EXTENDED-SPEED FINITE CONTROL SET MODEL PREDICTIVE TORQUE CONTROL FOR SWITCHED RELUCTANCE MOTOR DRIVES WITH ADAPTIVE COMMUTATION ANGLES

EXTENDED-SPEED FINITE CONTROL SET MODEL PREDICTIVE TORQUE CONTROL FOR SWITCHED RELUCTANCE MOTOR DRIVES WITH ADAPTIVE COMMUTATION ANGLES

BY

RASUL TARVIRDILU ASL

A THESIS

SUBMITTED TO THE DEPARTMENT OF ELECTRICAL & COMPUTER ENGINEERING

AND THE SCHOOL OF GRADUATE STUDIES

OF MCMASTER UNIVERSITY

IN PARTIAL FULFILMENT OF THE REQUIREMENTS

FOR THE DEGREE OF

DOCTOR OF PHILOSOPHY

Doctor of Philosophy (2020) McMaster University

Electrical & Computer Engineering Hamilton, Ontario, Canada

TITLE: Extended-Speed Finite Control Set Model Predictive Torque Control for Switched Reluctance Motor Drives with Adaptive Commutation Angles

AUTHOR: Rasul Tarvirdilu Asl

M.Sc. (Electrical Engineering)

Middle East Technical University, Ankara, Turkey

SUPERVISOR: Dr. Ali Emadi

Ph.D. (Texas A&M University)

IEEE Fellow

Canada Excellence Research Chair in Hybrid Powertrain

NUMBER OF PAGES: xxxiii,189

To my Family,

And beloved wife Sevda

Abstract

In this thesis, after a comprehensive literature review on different conventional and predictive torque control strategies for switched reluctance motor (SRM) drives, two online methods and one offline multi-objective optimization-based method are proposed to extend the operating speed range of finite control set model predictive torque control (FCS-MPTC) for SRM by adaptively controlling the commutation angles in the entire speed range. Furthermore, a method is proposed to minimize the steady state torque tracking error of FCS-MPTC for SRM drives.

The incapability of the conventional FCS-MPTC in controlling the commutation angles, which is considered as one of the main drawbacks of the conventional FCS-MPTC, limits its application for high-speed torque control of SRM drives. The phase turn-off angle is always selected to be close to the aligned position with the conventional FCS-MPTC regardless of the operating speed. However, commutation angle advancement is required for high-speed torque control of SRM drives to limit the negative phase torque resulting from the current tail after the turn-off angle in the generating region. Excessive negative torque with the conventional FCS-MPTC at higher speeds can result in a degraded performance with high rms current, low average torque, high torque ripple, and reduced efficiency.

The phase turn-off angle can be adaptively controlled as speed changes with the first online commutation angle control strategy proposed in this thesis. This method is based on predicting the free-wheeling phase current in an extended time interval which is much bigger than the prediction horizon of FCS-MPTC. The second online turn-off angle control method is also proposed by improving the optimality condition defined for determining the optimal turn-off angle. The optimality condition is determined by calculating the work done by the conducting phase after the phase is turned off.

The weighting factor of the objective function of FCS-MPTC is kept constant with both proposed online methods. An offline multi-objective optimization-based strategy is proposed to determine the globally optimal turn-off angle and the weighting factor in the entire operating torque and speed ranges. The effectiveness of both proposed online methods and the offline commutation angle control strategy is verified using simulations and experimental results. The results are also compared to the conventional FCS-MPTC and the indirect average torque control with optimized conduction angles which is considered as one of the main conventional torque control strategies for SRM drives.

In order to minimize the torque tracking error as a result of either parameter uncertainties or tracking multiple objectives with a single objective function with weighting factors, a method is proposed which is based on updating the reference torque at each sample time by calculating the average torque tracking error in the

previous sample times. The validity of the proposed method is verified using simulations.

Acknowledgements

I would like to express my sincere gratitude to my supervisor, Prof. Ali Emadi, for giving me the chance of being a part of a world-class multidisciplinary research team at McMaster Automotive Resource Center (MARC) to explore the cutting edge of technology in the field of transportation electrification. I would like to thank him for all his valuable advice and continuous support during my Ph.D. studies. His passion, dedication, enthusiasm, and creativity, altogether, makes him a unique personality and a role model.

I would like to thank my supervisory committee members Dr. Jennifer Buaman, and Dr. Dhafar Al-Ani for their valuable comments and suggestions to help me improve the quality of my PhD thesis. I had the honor of attending Dr. Bauman's course on electric vehicles which was very helpful in learning the fundamental concepts of EVs. I would like to thank Dr. Yue Zhao, who was the external examiner for my PhD thesis, for all his comments and suggestions to improve the quality of my thesis. I am also thankful to Dr. Babak Nahid-Mobarakeh for being the chair of PhD defense session.

I would like to express my deepest appreciation to Dr. Shamsuddeen Nalakath for all his time and sincere support. Shams was always present and eager to help in all the stages of the thesis starting from the theoretical analysis to experimental verifications, and even, publications.

I would like to thank Dr. Berker Bilgin for his constructive comments to improve the quality of my Ph.D. dissertation and publications. I am also grateful for all his support at the experimental stage of this thesis. Having the honor of attending his course on switched reluctance motors gave me the opportunity to build a solid theoretical understanding about SRMs.

I would like to thank my invaluable friend, Diego F. Valencia who was always available and eager to help with theory and experiments. I am very grateful for all his collaborations with the publications and experimental work. I am deeply grateful to Silvio Rotilli Filho for all his constructive comments and generous support.

I am thankful to the help and support of my colleagues Alan Callegaro, Christopher Mak, Zekun Xia, Gaoliang Fang, Dianxun Xaio and Aniket Anand for their help and assistance with my dissertation. I am also grateful to my lab colleagues Sumedh Dhale, Parisa M. Shamsabadi, Carin Yeghiazarian, Helia Jamali, Amirreza Poorfakhraei, Amir Akbari, Reihaneh Ostadian, Sobhan Kashfi, Shiva Ghasemi, Fatemeh Abolqasemi, Lucas Bruck, Mehdi Kazemi, Saeed Amirfarhangi, Ahoora Bahrami, Ali Ramezani, Peter Azer, Carlos Vidal, Maryam Alizadeh, Niloufar Keshmiri, Atriya Biswas, Negar Noroozi, and Jeremy Lempert. I would like to thank Teresa Janes, Theresa Mitchell, Dan Manolescu and Paul Nguyen for all their efforts in coordinating the research needs.

Words cannot express my gratitude to my parents Mohammadbagher and Fariba for their continuous support and endless love throughout my studies. I am grateful to my younger siblings Ali and Mahdieh for their never-ending encouragements. I would like to express my deepest love and gratitude to my wife, Sevda Ebrahimi, for her endless support, dedication, patience, and sacrifice in all these years. Everything that I have accomplished so far, I owe to my family.

Nothing can alleviate the pain, suffering and bitterness of losing two of my invaluable friends Iman Aghabali and Mehdi Eshaghian in the airplane crash in January 2020. They will be always missed, and all their good memories will be in my heart forever.

This research was undertaken, in part, thanks to funding from the Natural Sciences and Engineering Research Council (NSERC).

Contents

List of Figures

List of Tables

Notation

Abbreviations

AC	Alternating current
CCS-MPC	Continuous control set model predictive control
DAC	Digital to analog conversion
DBPC	Deadbeat predictive control
DC	Direct current
DITC	Direct instantaneous torque control
DTC	Direct torque control
EMF	Electro-motive force
FCS-MPC	Finite control set model predictive control
FCS-MPTC	Finite control set model predictive torque control
FEM	Finite element method
GA	Genetic algorithm
GPC	Generalized predictive control
HCC	Hysteresis current control
IM	Induction motor
ITC	Indirect torque control
IPMSM	Interior permanent magnet synchronous motor
LUT	Look up table
MPC	Model predictive control

PCC	Predictive current control
PM	Permanent magnet
PMSM	Permanent magnet synchronous motor
PTC	Predictive torque control
PWM	Pulse width Modulation
SRM	Switched reluctance motor
SVM	Space vector modulation
TSF	Torque sharing function
VF	Virtual flux
VV-FCS-MPC	Virtual vector finite control set model predictive control

Symbols

$\Delta\theta$	Difference between the electrical angles of the phase
ΔL	Difference between minimum and maximum inductances
$\Delta T_{percent}$	Percentage of torque ripple
ΔT_{rms}	rms torque ripple
ε	Back-emf
θ, θ_{elec}	Electrical angle of the phase
θ_{mech}	Rotor position (mechanical angle)

θ_{off}	Phase turn-off angle
θ_{on}	Phase turn-on angle
θ_{ov}	Overlap angle for torque sharing functions
λ	Phase flux linkage
λ_{err}	Flux error
λ_s	Saturation flux linkage
ω	Rotor angular speed in electrical rad/s
A	Torque area
E_T	Torque tracking error
f	Objective function
f_{GA}	Objective function of genetic algorithm
$f_{GA,hyst}$	Objective function of genetic algorithm for hysteresis controller
f_{MPC}	Objective function of MPC
F_r	Radial force
f_{sw}	Switching frequency
i, i_{phase}	Phase current
I_{max}	Maximum phase current limit
I_{ref}	Reference current
I_{rms}	rms phase current
k	Time step

k_{MPC}, δ	Weighting factor of MPC
L	Phase inductance
L_{av}	Average inductance
N_r	Number of rotor poles
n_r	Rotor speed in rpm
n_{ref}	Reference rotor speed in rpm
P_{cu}	Copper losses
R	Phase resistance
R_r	Rotor outer radius
t	Time
T_{avg}	Average torque
T_e	Electromagnetic torque
T_{err}	Torque error
T_{max}	Maximum instantaneous torque
T_{min}	Minimum instantaneous torque
T_{rated}	Rated torque
T_{ref}	Reference torque
T_{ref}^*	Updated reference torque
T_s	Sampling time
V_{DC}	DC link voltage
v_{phase}, u	Phase voltage

w	Weighting factor for the objective function of multi-objective genetic algorithm optimization
W_c	Co-energy
W_f	Energy

Chapter 1

Introduction

1.1 Background and motivation

Switched reluctance motors (SRMs) are the low-cost alternatives of permanent magnet and induction motors (IMs), as they possess a simple structure without rotor bars or permanent magnets. Three-phase line start induction motors are less costly compared to both permanent magnet and switched reluctance motors, as they can directly be connected to the grid, and the need for the drive system is eliminated. However, the need for a highly efficient drive for adjustable-speed applications brings the necessity of the need for an inverter and a drive system. Hence, the cost of the drive system diminishes the superiority of the IMs in terms of the cost. Besides, IMs have high ohmic losses in rotor bars which reduces their efficiency. Permanent magnet synchronous motors (PMSMs) have higher efficiency and better power factor compared to IMs. The problems associated with higher cost of permanent magnet materials, their limited supply chain and environmental

concerns are considered as the main drawbacks of using PMSMs [1]. High cost of permanent magnet materials reduces the attractiveness of PMSMs in cost-sensitive applications.

The simple and low-cost doubly salient structure with concentrated windings on the stator and no magnets or bars on the rotor, ability to operate at harsh environments, high speeds and high temperatures [2] (due to lack of windings or magnets on the rotor), and fault tolerant capability are several other advantages that lead SRM to be a promising candidate for versatile applications. However, highly nonlinear electromagnetic characteristic, torque ripple, and acoustic noise and vibration due to its double-salient structure are the main drawbacks of this machine limiting its widespread use in high performance applications, e.g. automotive [3], [4]. However, there are recent advancements in the design and control of SRM on improving many of its drawbacks [5]. In the design stage, torque ripple and acoustic noise is reduced by optimizing geometric parameters of SRM including pole combination [6], pole arcs, air gap length, etc. The modern finite element and optimization tools are effectively employed in the literature to minimize the torque ripples and electromagnetic nonlinearities [7]. The torque ripple and acoustic noise [8]–[13] can also be minimized in the control stage by employing novel and highly efficient control strategies [14]. In [15], guidelines to select the suitable control methods depending on the operating mode and speed to achieve better performance are provided. The indirect average torque control (ITC) and direct torque control

(DTC) [16], [17] are the common SRM control methods in the literature. The advanced techniques like model predictive control (MPC) [18]–[21], commutation angle optimization with average torque control [7], current profiling [22], and torque sharing functions (TSF) [23]–[26] are also developed to reduce the torque ripple and improve the efficiency. The main objectives which are considered in developing a control algorithm for SRM are maximizing the efficiency, reducing the torque ripple, acoustic noise and vibration along with minimizing the response time of the controller. The selection of the control method is largely dependent on the application.

Model predictive control was first implemented to control the systems with large time constant such as chemical processes due to its inherent high computational burden and lack of powerful processors. In recent years, significant advancements in microprocessor and semiconductor technologies has made it possible to implement MPC in power electronics and motor drive applications [27]. Complex switching rules and modulation schemes can be avoided using MPC, as the optimum voltage vector is directly applied at each sample time [18]. There are different MPC methods proposed in the literature including finite control set MPC (FCS-MPC), continuous control set MPC (CCS-MPC), generalized predictive control (GPC), deadbeat control, direct MPC, explicit MPC and adaptive MPC with self-tuning capability. FCS-MPC stands as the most popular predictive control method for power electronics and motor drive applications due to its faster response

time, capability of handling nonlinearities and constraints and simple and straightforward implementation [28]. Besides, finite number of possible switching states of the power converter at each switching instant has been another incentive to adopt FCS-MPC for this application. This approach has been well-developed for control of induction, permanent magnet and synchronous reluctance motor drives; however, the technology is not mature enough for SRM drives, mainly because of the heavy computational burden on the microcontroller due to the highly nonlinear electromagnetic characteristics of SRM. Complexities associated with control of SRM drives stemming from their highly nonlinear flux and torque characteristics and their doubly salient structure can be better handled using FCS-MPC.

An accurate model of the SRM is needed to predict the future state of the machine in MPC. The models are either analytical or based on lookup tables. The accuracy of the model is an important factor affecting the performance of the controller. MPC is mostly used for current control of SRM in the literature. A fixed switching frequency predictive current control is implemented in [29]. A predictive current control method with fixed switching frequency is proposed in [30] for low torque ripple and low acoustic noise applications. A model predictive current control of SRM that takes into account the inductance variations and measurement uncertainties is proposed in [19] and [20].

Finite control set model predictive torque control (FCS-MPTC) is implemented in [18], [21], [31] for torque control of SRM drives to achieve lower torque ripple,

rms current and average switching frequency using a single objective function with weighting factors. A similar approach is adopted in [32] and [33] to minimize torque ripple and rms current for torque control of SRM using FCS-MPC. The predictive approach can be integrated with torque sharing functions (TSF) [34]–[36] or direct torque control (DTC) [37], [38] to improve the performance of the conventional torque control techniques. Most of the studies in the literature focus on controlling SRM drives using FCS-MPC in the low-speed (constant torque) region. As the speed increases, the current control [39], [40] gets more challenging in SRM drives due to increased back-emf, which brings the necessity of advancing the commutation angles to minimize the phase negative torque. The existing finite set model predictive torque control for SRM is incapable of controlling the commutation angles and suffers from the large negative phase torque and large torque ripples especially in the high-speed region, which limits its operating speed range for SRM drives. This issue, which is the main focus of this thesis, has not been addressed in the literature.

1.2 Thesis contributions

As mentioned in the previous section, incapability of the existing FCS-MPTC in controlling the commutation angles in predictive torque control of SRM drives is one of the main drawbacks of this method. The turn-off angle is always adjusted to be very close the aligned position regardless of the speed. To achieve a highly

efficient control, the commutation angles need to be advanced as the speed increases to minimize the negative torque produced by the outgoing phase in the generating region. Three methods have been proposed in this thesis to adaptively control the commutation angles in the entire speed range. The problems associated with the incapability of the existing FCS-MPTC in adjusting the commutation angles are effectively managed with the proposed methods. The proposed methods can adjust the phase turn-off angle to extend the operating speed range of FCS-MPTC for SRM. The effectiveness of the proposed control methods in terms of improving the efficiency and reducing RMS current and torque ripple is demonstrated in this thesis through simulations and experimental results. The results are also compared with FCS-MPTC without the proposed commutation angle control (conventional FCS-MPTC) and indirect average torque controller with optimized commutation angles. Finally, a method is proposed to minimize the steady state torque tracking error of FCS-MPTC in SRM drives. The main contributions of this thesis are summarized as follows:

1. First online adaptive turn-off angle control for FCS-MPTC of SRM drives

2. Second online adaptive turn-off angle control for FCS-MPTC of SRM drives

3. Multi-objective optimization based offline turn-off angle control for FCS-MPTC of SRM drives

4. Steady state torque tracking error minimization of FCS-MPTC for SRM drives

5. Considerable reduction of online computation time of the conventional FCS-MPTC with the proposed objective function evaluation technique

1.3 Thesis outline

The main focus of this thesis is proposing online and offline adaptive commutation angle control methods with considerably reduced online computation time for FCS-MPTC of SRM drives to reduce the phase negative torque, phase rms current, and torque ripple. Besides, a method is proposed to minimize the steady state torque tracking error of FCS-MPTC.

In Chapter 2, the fundamentals of switched reluctance motors including their operating principles, static flux linkage and torque characteristics, phase voltage equations and torque production principles are briefly described. After presenting the schematic diagram of the asymmetric bridge converter and discussing the hard and soft switching techniques, the current and torque control methods for SRM drives are briefly introduced. The conventional torque control methods including DTC, ITC, TSF and current profiling are then described in more details.

In Chapter 3, the classification of the predictive control approaches applied for SRM drives in the literature are presented. Then, a comprehensive literature review

is presented on predictive torque control methods for SRM drives. Both conventional and predictive torque control methods are compared in terms of their characteristics and performance. After presenting the schematic diagram of different predictive torque control methods, these methods are compared in terms of their phase torque distribution, the utilized predictive model, calculation of the reference voltage, modulation scheme and the implemented switching type.

In chapter 4, after presenting the look up table based discrete predictive model of SRM, the formulation and implementation of the conventional FCS-MPTC is discussed. Then, the shortcomings of the conventional FCS-MPTC in adjusting the commutation angles at higher speeds is shown and verified by simulations. Finally, the experimental setup is described along with the characteristics of the test motors used in this thesis and the experimental test results of the conventional FCS-MPTC.

In chapter 5, after describing the proposed optimality condition for the first online adaptive commutation angle control scheme, the analytical equations to predict the phase current waveform are presented and discussed. A sector partition technique is then proposed to reduce the computational burden of FCS-MPTC. Finally, the proposed method is validated by simulations and experimental results, and the improvements are compared to the conventional FCS-MPTC.

In chapter 6, the proposed second online adaptive turn-off angle control is presented. The proposed optimality condition to determine the optimal turn-off

angle which is based on the energy balance concept is also discussed. Finally, the simulation and experimental results are shown to prove the effectiveness of the proposed scheme.

In chapter 7, the proposed offline multi-objective optimization-based commutation angle control is presented. After formulating the multi objective optimization problem, it is solved using the genetic algorithm (GA) optimization method. Furthermore, a parametric sweep of optimization variables is demonstrated to show the effect of the variation of optimization variables on the performance of SRM. An optimal solution is selected after presenting and discussing the pareto front of the optimization. Finally, the proposed method and the obtained results are validated by simulations and experimental results.

In chapter 8, after presenting the simulations and experimental results for the indirect average torque control with optimized conduction angles, a comprehensive performance comparison (using both simulations and experimental tests) is carried out by presenting and comparing the results of the conventional and proposed FCS-MPTC and the ITC with optimized conduction angle methods. The performance of the controllers is also compared under speed dynamics.

In chapter 9, a method is proposed to minimize the steady state torque tracking error of the FCS-MPTC for SRM drives. In the proposed method, the reference torque is updated at each sampling instant by calculating a compensation term considering

the accumulative torque tracking error in the previous sample times. The effectiveness of the proposed method in reducing the torque tracking error and its effect on the performance of SRM is investigated by providing comprehensive simulation results.

Finally, the conclusions and suggested future work along with the list of publications are presented in chapter 10.

Chapter 2

Fundamentals of Switched Reluctance Motor (SRM) Drives

In this chapter, the fundamentals of operation, modeling and control of SRM drives are briefly presented. First, the concept of pole configuration and the relationship between mechanical and electrical angles are described. Then, the 2-D characteristics of the SRM are introduced and the governing circuit equations are presented. Finally, a brief description is given on SRM drives and the conventional current and torque control methods for SRM are briefly introduced.

2.1 Operating principles of switched reluctance motors

Switched reluctance motors have a simple structure [41] and low manufacturing cost compared to IPM and IM machines, as they have concentrated stator windings with no permanent magnets or bars on the rotor [42]. Stator and rotor cores are both fabricated from laminated silicon steel sheets. The number of stator and rotor poles

in an SRM is selected based on the application requirements in the design stage. The number of phases in an SRM is dictated by the pole configuration and the connection type of the stator windings. The cross sections of sample 4-phase 8/6 and 3-phase 12/8 (used as the reference SRM1 in this thesis) switched reluctance motors are shown in Figure 2.1-a and b respectively. The geometric parameters including pole heights, pole arcs, air gap length, etc. need to be carefully designed in the design stage to achieve a desired torque-speed performance under a specific DC link voltage and dimensional constraints while minimizing the torque ripple and acoustic noise.

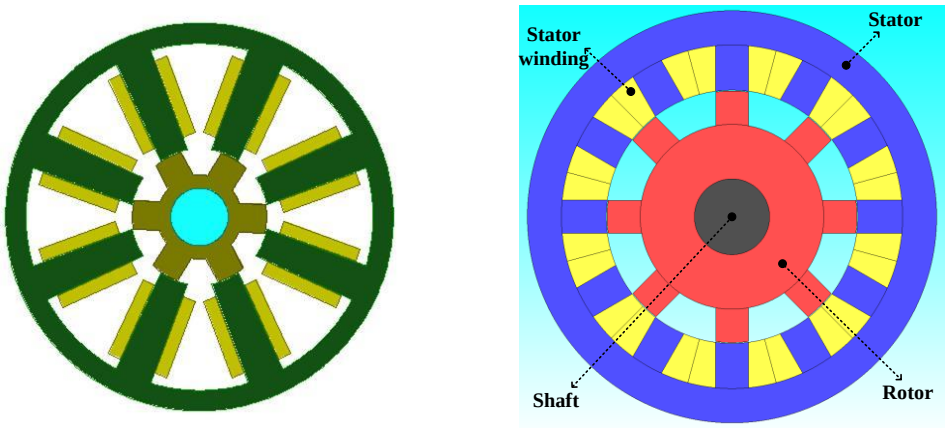

(a) (b)

Figure 2.1: Cross section of SRM; (a) four phase 8/6 SRM, and (b) three phase 12/8 SRM

In both IPM and IM machines the torque is generated by the interaction between the stator and rotor magnetic fields. However, in SRM, there are no permanent magnets or bars on the rotor. In SRM, the rotation happens as a result of reluctance torque which tries to minimize the reluctance of the flux path by aligning the rotor poles with the excited stator poles. In the conventional SRM, the phases are

magnetically and electrically isolated and the mutual coupling between phases is usually neglected. By sequential excitation of the consecutive phases, the continuous rotation is maintained.

The position in which the rotor pole is aligned with the excited stator pole (maximum phase inductance) is called the aligned position with the electrical angle of 180°. On the other hand, the position in which the excited stator pole is located in the middle of two consecutive rotor poles (minimum phase inductance) is called the unaligned position ($\theta_{elec} = 0^{\circ} = 360^{\circ}$). It can be understood that in a 3-phase 12/8 SRM, one complete electrical cycle (360° electrical) is equivalent to 45° mechanical. In other words, 8 complete electrical cycles happen in one complete rotor revolution. The relationship between electrical and mechanical angles in an SRM is described as

$$\theta_{elec} = N_r \theta_{mech} \tag{2.1}$$

where θ_{elec} and θ_{mech} stand for electrical angle and mechanical angle of the phase, and N_r is the number of rotor poles.

Unlike IM and IPM machines, flux and torque in SRM are largely dependent on both current and rotor position. A 2.3 kW, 6000 rpm, three-phase 12/8 SRM with a DC link voltage of 300 V is chosen as the reference machine (SRM1), in this thesis. Flux linkage-position-current and torque-position-current characteristics of the reference SRM1 have been derived from electromagnetic FEM software, JMAG.

The characteristics are given in Figure 2.2-a and b respectively in one complete electrical cycle (45^o mechanical angle).

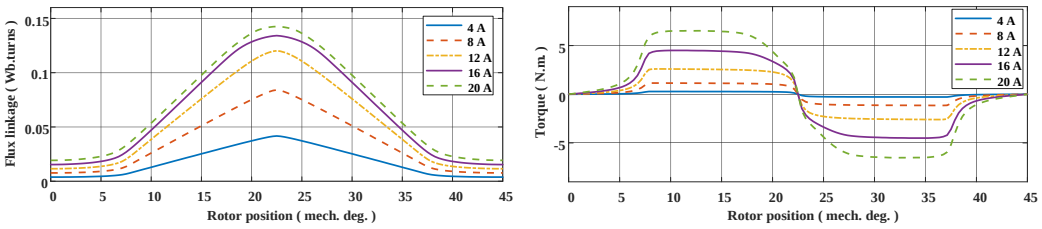

(a) (b)

Figure 2.2: Static characteristics of the test SRM1; (a) flux linkage-position-current, and (b) torque-position-current

It can be observed that both flux linkage and torque are functions of rotor position and the phase current. Hence, SRM has a highly nonlinear flux and torque characteristics which makes its performance analysis and control more complicated compared to IM and IPM motors. As the phases of SRM are electrically isolated, torque ripple happens in the commutation regions in which the conducting phase is turned off and the upcoming phase is responsible to deliver the reference torque on the shaft. These 2-D static characteristics are approximated using analytical equations or stored in look up tables to incorporate in implementation of the control schemes for SRM.

It can be observed from Figure 2.2-b that torque production capability of SRM is zero at both aligned and unaligned positions. Furthermore, SRM generates positive torque in inductance rising region (0°-180° electrical) known as motoring region. The torque is negative in the inductance falling region (180°-360° electrical), known as generating region. The variation of the phase inductance of the test SRM1

versus position and phase current in one complete electrical cycle is shown in Figure 2.3.

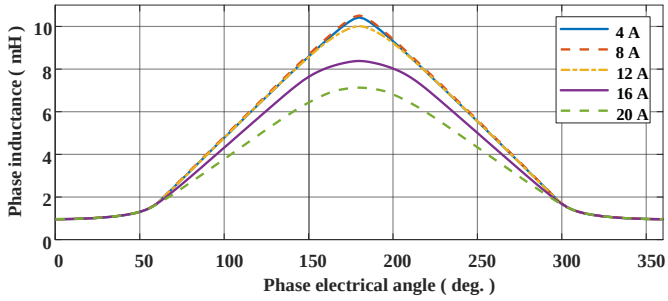

Figure 2.3: Variation of phase inductance of the test SRM1 versus electrical angle and current.

The phase voltage (v_{phase}) equation of SRM by neglecting the mutual coupling between the phases is represented as [43]

$$v_{phase} = Ri + \frac{d\lambda(\theta, i)}{dt} \tag{2.2}$$

where R, λ, i and θ stand for phase resistance, phase flux linkage, phase current and the phase electrical angle, respectively. By expanding (2.2),

$$v_{phase} = Ri + L(\theta, i)\frac{di}{dt} + i\frac{dL(\theta, i)}{d\theta}\omega \tag{2.3}$$

where L and ω stand for phase inductance and rotor angular speed in electrical rad/s. The term $\varepsilon = i\frac{dL(\theta,i)}{d\theta}\omega$ represents the back-emf in an SRM, which is dependent on phase current, slope of inductance and speed. Unlike PM motors, the back-emf cannot be directly measured in SRM [44]. The phase equivalent circuit of an SRM is shown in Figure 2.4.

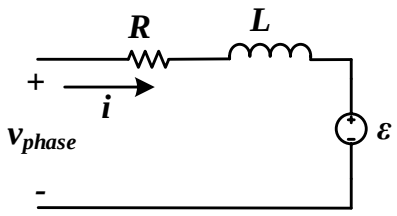

Figure 2.4: Phase equivalent circuit of an SRM

Torque equation in an SRM is represented as

$$T_e = -\frac{\partial W_f}{\partial \theta}|_{\lambda=constant} \tag{2.4}$$

where W_f is the energy stored in the magnetic circuit. For theoretical analysis, torque in SRM is usually expressed as a function of magnetic co-energy (W_c). The co-energy is a non-physical quantity, and it is used for theoretical analysis purposes. The relationship between magnetic energy and co-energy is

$$W_c = i\lambda(\theta, i) - W_f. \tag{2.5}$$

The torque equation as a function of magnetic co-energy is represented as [45], [46]

$$T_e = \frac{\partial W_c}{\partial \theta}|_{i=constant}. \tag{2.6}$$

The graphical representation of energy and co-energy in an SRM is given in Figure 2.5.

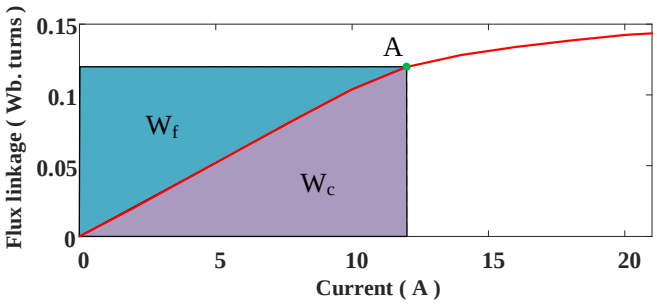

Figure 2.5: Graphical representation of energy and co-energy

2.2 Switched reluctance motor drives

Per-phase diagram of asymmetric bridge converter which is commonly used to drive SRM is presented in Figure 2.6. Three different voltage levels ($-V_{DC}$, 0 and $+V_{DC}$) can be achieved using this converter. If both S_1 and S_2 are active (S=1), the phase voltage is $+V_{DC}$. The freewheeling mode ($v_{phase}=0$) is achieved if either S_1 or S_2 are active (S=0). Finally, if both S_1 and S_2 are off (S= -1), $-V_{DC}$ appears on the phase terminals. The representation of the phase current path corresponding to each voltage level is depicted in Figure 2.6 (a)-(c). If all three possible switching states per phase are used to control SRM, the switching mode is called "soft switching". If only $+V_{DC}$ and $-V_{DC}$ are used, the switching mode is known as "hard switching".

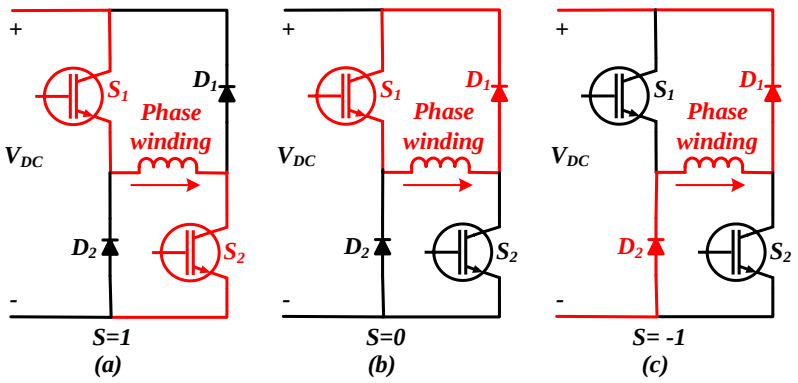

Figure 2.6: Per-phase diagram of asymmetric bridge converter; (a) $v_{phase}=+V_{DC}$ (S= +1), (b) $v_{phase}=0$ (S=0), and (c) $v_{phase}=-V_{DC}$ (S= -1).

Similar to AC machines, torque control in SRM can be implemented using cascaded control loops. The outer loop usually controls the speed and generates the desired reference torque required for tracking the reference speed. The inner loop (current

control loop) is usually implemented to track the reference currents to achieve the desired reference torque on the shaft. Hysteresis current control (HCC) [47], [48] is usually preferred to other control methods in SRM drives due to its simple structure, straightforward implementation, and elimination of the need to know machine parameters. The purpose of HCC is keeping the current within a band known as hysteresis band. However, HCC suffers from the variable switching frequency. To achieve a current control with constant switching frequency, PWM current control [49] can be implemented. This, on the other hand, brings the need for a PWM modulator, and reduces the speed of the dynamic response of the controller. Recently, the predictive current control (PCC) approach has gained considerable attention among researchers. Generalized predictive control (GPC) [50], deadbeat predictive control [29], [30], [51]–[54], hysteresis-based predictive control [55], [56], and model predictive control (MPC) are considered as the main predictive control approaches in the literature developed for current control of SRM drives. MPC is categorized as continuous control set-MPC (CCS-MPC) [19], [20], [57] and finite control set-MPC (FCS-MPC) [58]–[60]. A predictive model is required in both MPC methods to predict the future state of the machine. A modulation stage is required to be integrated with CCS-MPC, hence, resulting in a constant switching frequency control. On the other hand, FCS-MPC, which is the most popular predictive current control strategy applied in power electronics and motor drive applications, eliminates the need for the modulator, leading to a

variable switching frequency control. Elimination of the modulation stage results in a faster dynamic response compared to CCS-MPC.

The conventional torque control techniques are generally divided into two broad categories, direct torque control (DTC) and indirect torque control (ITC). In the former, the switching signals are usually generated directly using torque hysteresis controller and switching tables [16], while the internal current control loop is implemented in the latter to regulate the current and produce the reference torque. The indirect torque control can be divided into two broad categories; indirect average torque control and indirect instantaneous torque control. The most common indirect torque control scheme is the indirect average torque control method. Characteristics of both conventional and predictive torque control methods for SRM drives are summarize in Table 3.1.

DTC has a simple structure, proper robustness, and faster dynamic response as there is no internal current loop, and the torque is directly treated as the control variable. The block diagram of DTC control strategy is given in Figure 2.7.

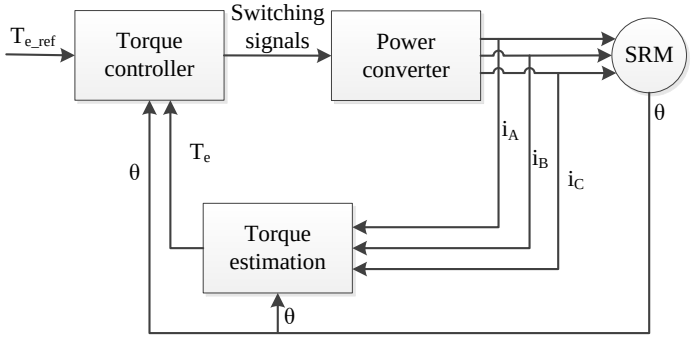

Figure 2.7: Block diagram of direct torque control (DTC) for the SRM

DTC requires complex switching rules to be calculated offline. As a response, DITC has gained popularity in SRM due to the simplicity in implementation and proper ripple results, but both DTC [16], [61] and DITC [62], [63] suffer from large current ripples and limited performance at the high-speed region [15] and low-load condition. The lack of regulation of phase currents also represents a potential hazard for the drive itself. Torque control capability in DITC technique, depends on complex switching rules and sampling time of the controller [64].

On the other hand, indirect average torque control with optimized conduction angles, torque sharing functions and current profiling are considered as three main ITC methods for SRM drives. The block diagram of the indirect average torque control with optimized conduction angles which is considered as the most commonly used technique for torque control of SRM drives is presented in Figure 2.8.

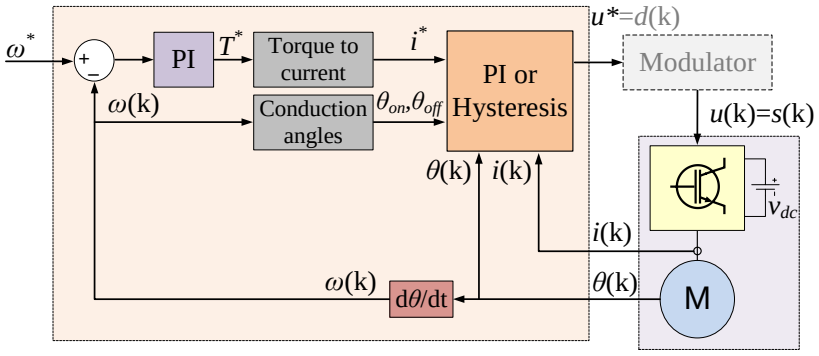

Figure 2.8: Block diagram of indirect average torque control

Optimization methods calculate, offline, optimal reference currents and commutation angles for different operating conditions to achieve some predefined performance targets (lower torque ripple, higher efficiency, lower vibration and acoustic noise) [7], [65], [66]. The data is then stored as look-up tables (LUTs) for the experimental implementation. In ITC, the phase currents have rectangular waveform at lower speeds. As speed increases, due to the induced back-emf, the current cannot rise up to the desired predetermined reference level, and the current waveform is not rectangular anymore. Either hysteresis or PWM current controller can be used to control the phase currents in ITC. The indirect torque control with optimized turn-on and turn-off angles is usually integrated with hysteresis current controller. This method will be referred to as "optimized hysteresis controller" in this thesis. This method is not capable of shaping the current and the current is controlled to be inside the hysteresis band inside the conduction period. The simulated performance of the reference SRM1 with optimized hysteresis controller at 2000 rpm (under load torque of 3 Nm) and 6000 rpm (under load torque of 1.5 Nm) are presented in Figure 8.1 and Figure 8.2, respectively.

The phase currents are shaped in both TSF and current profiling schemes to achieve the desired performance. Torque sharing functions distribute the reference torque among individual phases to achieve a constant reference torque on the shaft [23]. The transition between the phases can be linear, quadratic, cubic or even sinusoidal to compensate for the difference in phase inductance between the two interacting

phases [67]. The reference currents are determined using $i(T,\theta)$ static maps and fed to the current controller to complete the control loop, and the switching behavior depends on the current controller. Sample reference torque waveforms (linear TSF) of the test three phase SRM1 for T_{ref}=1 Nm are shown in Figure 2.9-a. The corresponding reference current waveforms calculated using inverse $i(T,\theta)$ LUT are depicted in Figure 2.9-b. These current waveforms are then fed to the current controller to be tracked.

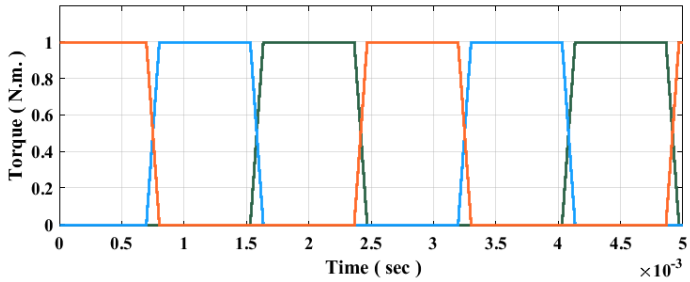

(a)

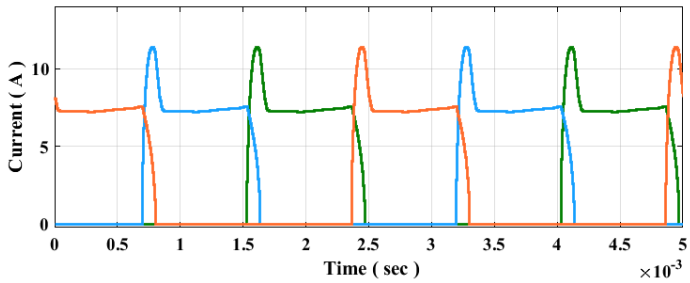

(b)

Figure 2.9: Reference phase torques and phase currents of the three-phase SRM1 using linear torque sharing function (TSF); (a) phase torques, and (b) phase currents.

The simulated performance of the test SRM1 with linear TSF at 1800 rpm under load torque of 1 Nm is presented in Figure 2.10. Note that the turn on angle (θ_{on}) and the overlapping angle (θ_{ov}) are set to 40° and 15° mechanical, respectively.

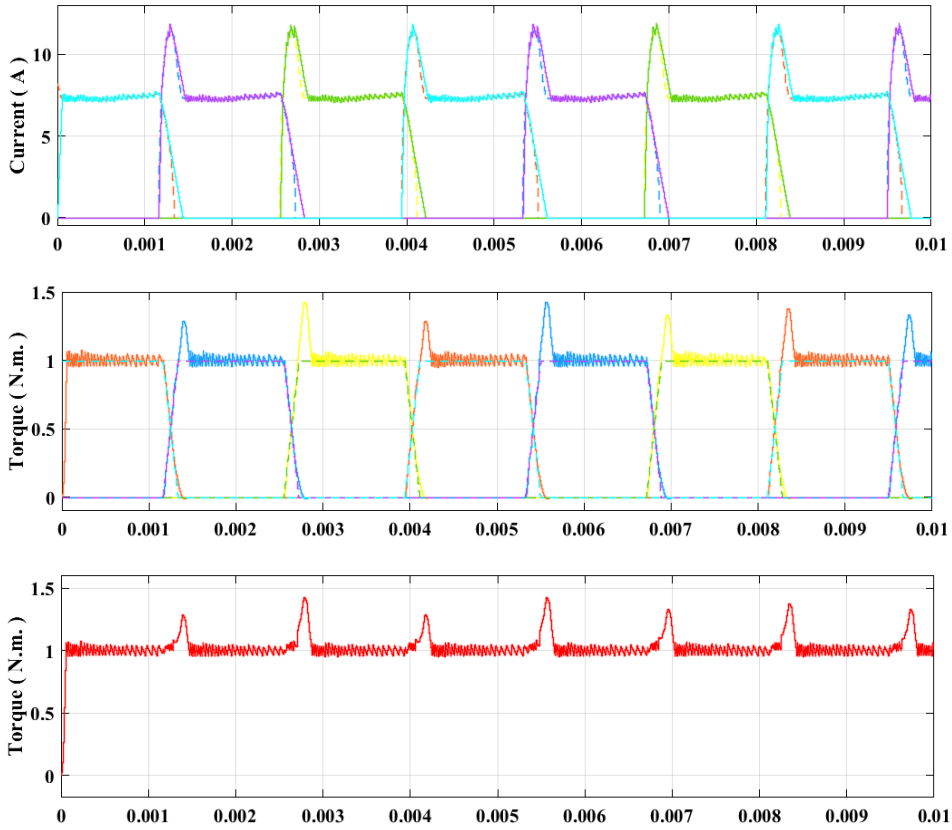

Figure 2.10: Current and torque waveforms of the test SRM1 at 1800 rpm (Linear TSF, T_{ref} =1 N.m., θ_{on} =40°, θ_{ov} =15°)

The same simulation is repeated at a higher speed of 3000 rpm (Linear TSF, T_{ref} =1 Nm, θ_{on} =40°, θ_{ov} =15°). The waveforms are shown in Figure 2.11.

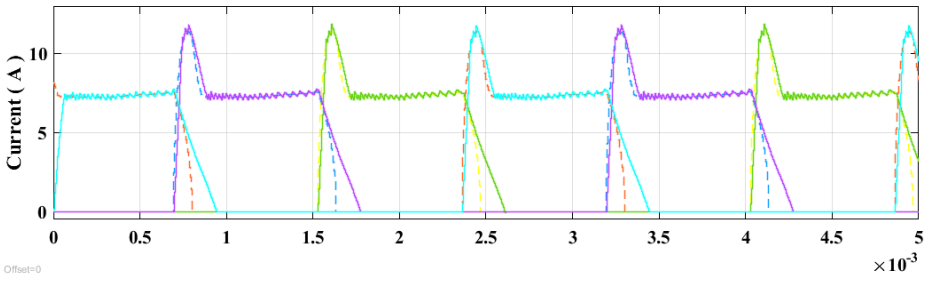

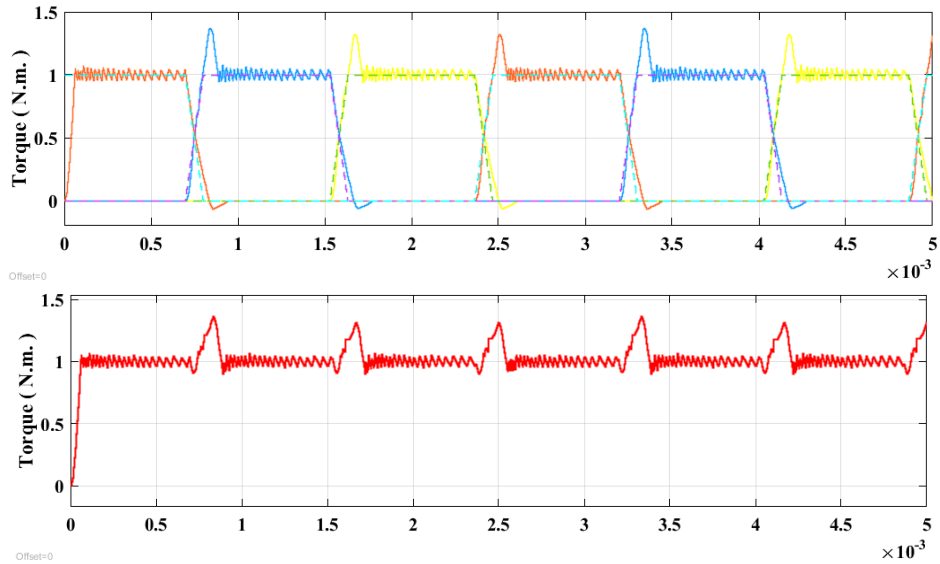

Figure 2.11: Current and torque waveforms of the test SRM1 at 3000 rpm (Linear TSF, T_{ref} =1 N.m., θ_{on} =40°, θ_{ov} =15°)

It is observed from Figure 2.10 and Figure 2.11 that the reference current tracking is deteriorated at higher speeds after the phase is turned off, which causes the current tail in the generating region, and consequently the negative torque production. Because torque production capability of the SRM is very low near the unaligned position, having a lower turn-on angle leads to a large reference current. Therefore, it is not possible to have advance firing using the TSF. So, TSF control scheme cannot compete with conventional control methods at higher rotational speeds. Simple control structure and straightforward implementation are the advantages of TSF schemes. In the current profiling method, the reference current profiles are calculated offline to achieve the desired performance targets [68].

The predictive torque control with its capability of handling nonlinearities and constraints, simple and straightforward implementation and faster dynamic

response compared to the conventional control techniques has gained considerable attention among researchers to be used for motor control applications. As mentioned earlier, SRM has a highly nonlinear flux and torque characteristics which makes its control more challenging compared to the conventional AC drives. Predictive torque control is considered a suitable approach to control SRM drives. Next chapter will present a literature review on different predictive control approaches developed to control SRM drives.

2.3 Summary

The fundamental concepts about modeling and control of SRM drives are briefly presented in this chapter. After brief descriptions on operating and torque production principles of SRM, the static 2-D characteristics of the test SRM1 are presented. Then, the conventional current and torque control strategies are briefly described. The predictive control approaches for SRM drives and their comparison with conventional control methods will be presented in the next chapter.

Chapter 3

Model Predictive Control of SRM Drives

In this chapter, the classification of predictive control approaches applied to SRM drives in the literature is presented. Then, a comprehensive literature review is presented on different predictive torque control methods applied to SRM drives in the literature. The predictive torque control methods will be comprehensively compared in terms of phase torque distribution, predictive model, calculation of the reference voltage, modulation scheme and switching behavior.

3.1 Classification of predictive control methods for SRMs

Predictive control is known for its better dynamic response, simple control structure and straightforward implementation [69]. Besides, it is capable of effectively handling the constraints and nonlinearities of the system. It all comes at the expense of higher computational burden, which can be managed by the recent advancements in microprocessor technology.

Predictive control determines the optimal inputs to the system (switching signals in case of a motor drive) to achieve the desired performance target by predicting the future state of the plant using a predictive model. Different approaches have been considered to control SRM drives. Generalized predictive control (GPC), based on linearizing the model of the plant, is not very popular in motor drive applications, especially SRM drives, given the highly nonlinear characteristics of the motor and inverter, but it offers the possibility to include disturbances within the formulation [70].

In deadbeat predictive control (DBPC), the optimal input is directly calculated using the predictive model, thus reducing the steady-state error to zero, but it suffers from measurement noise and parameter sensitivity [69]. Both GPC and DBPC use a modulator and hence have a fixed switching frequency.

In the case of using the predictive model along with a cost function, the predictive approach is called model predictive control (MPC). It is divided into two general categories; continuous control set (CCS-MPC) and finite control set (FCS-MPC). The former defines a continuous cost function and finds the exact optimal voltage to be applied in the next sampling period. As the converter applies the voltage in form of PWM, a duty cycle output fixes the switching frequency through a modulator. The modulator is eliminated in FCS-MPC, which allows including the discrete states of the converter keeping a proper dynamic response [71]. Its drawback is the variable switching frequency. A fixed switching frequency control

has been achieved in FCS-MPC by using the virtual voltages (VV), and it has been successfully implemented in multi-phase machines [72].

An alternative to simplify modelling and computational burden has been the use of controllers in the virtual-flux (VF) domain. The VF-control maps the machine variables into the flux domain, which allows controlling the equivalent rotor flux, hence, resulting in improving the stability and robustness of the controller [73].

3.2 Predictive torque control of SRM

Predictive torque control (PTC) for induction and PMSM drives has been well studied in the last decades; however, the nonlinear characteristics of the SRM and the lack of straightforward and closed-form analytical equations for predicting its performance have been a barrier for development of PTC for SRM drives. Recently, researchers have been more interested towards implementing these techniques for SRM drives. A comprehensive analysis, review and comparison on different predictive torque control approaches applied for SRM drives in terms of their requirements for modulator, modelling, control variable and switching behavior is given in this section. The classification and characteristics of both conventional and predictive torque control approaches for SRM drives are summarized in Table 3.1.

Table 3.1: Characteristics of both conventional and predictive torque control methods for SRM drives

Control type	Control technique		Need for offline calculations	Calculation of reference voltage or switching state	Modulator	Current regulation	High-speed	Four-quadrant	References
Classic torque control	DTC		☑	Switching table	☐	☐	☐	☑	[16]
	DITC		☑	Switching table	☐	☐	☐	☐	[62]
	ITC with optimum conduction angles		☑	Inner current loop	n/a	☑	☑	☑	[7], [66]
	TSF		☑	Inner current loop	n/a	☑	☑	☑	[23], [26], [67]
	Current profiling		☑	Inner current loop	n/a	☑	☑	☑	[68], [74]
Predictive torque control	DBPC		☐	Direct calculation	☑	☐	☐	☐	[17], [75]–[79]
	GPC		☑	Continuous cost function	☑	☐	☐	☐	[80]
	FCS-MPC	Conventional	☐	Discrete cost function	☐	☑	☑	☐	[18], [21], [31], [32], [34]–[36], [81]
		VF-FCS-MPC	☐	Discrete cost function	☐	☑	☑	☐	[37], [38]
		VV-FCS-MPC	☐	Discrete cost function	☑	☑	☐	☐	[33]

Figure 3.1 shows the block diagram of the FCS-MPC-based PTC strategy, which is the most popular predictive control technique for torque ripple reduction thanks to its simplicity, capability of handling nonlinearities and constraints, and straightforward implementation.

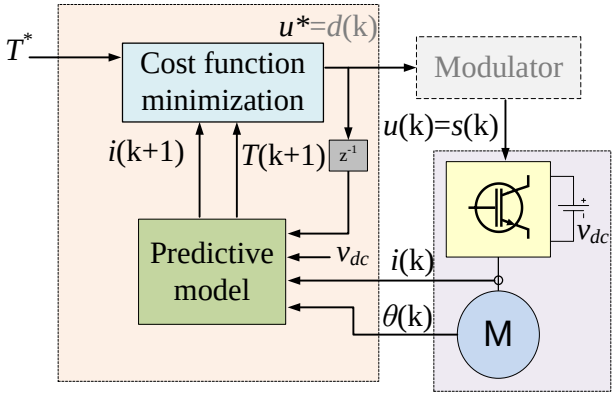

Figure 3.1: Block diagram of FCS-MPTC

The algorithm uses the measured phase current $i(k)$ and rotor position $\theta(k)$ to feed the predictive model and estimate the torque output $T(k+1)$. In this case, the torque output is a n-size vector where n is the number of possible switching states, which is $3^3 = 27$ for a three-phase SRM. The predicted torque values are then used in a cost function to decide which of the switching states provides the minimum error with respect to the torque reference. Alternatively, as shown in Figure 3.1, the phase currents $i(k+1)$ can also be predicted and included in the cost function to be minimized, as an effort to reduce the copper losses. This is included in the cost function as a secondary objective with a weight factor δ_i [21]. The optimal switching state can be selected based on the predicted performance of the machine in either one (single-step MPC) or more (multi-step MPC [21]) future sample times. Using multi-step FCS-MPC leads to exponentially increased computational burden, but it still cannot provide considerable improvements in the high-speed performance. The effect of number of prediction horizons on the performance of FCS-MPC for low-speed torque control of SRM is shown in [21].

Figure 3.2 shows the DBPC strategy for torque control, in which the cost function is omitted, and the reference voltage $v(k+1)$ is directly calculated by the predictive model in form of a duty cycle. This guarantees a constant switching frequency by using a modulator.

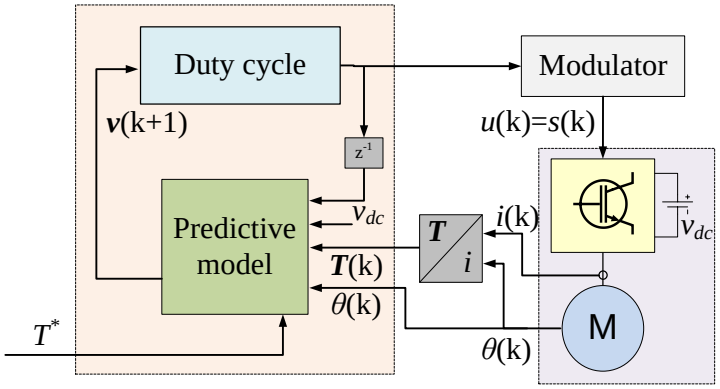

Figure 3.2: Block diagram of deadbeat predictive control (DBPC)

As the response of this model lies on the predictive model, the accuracy can be enhanced by mapping the control variable in the VF frame (VF-DBPC). This representation modifies the control as shown in Figure 3.3, where static maps are included to estimate flux linkages, thus simplifying the prediction and calculations, as it is possible to use equation (2.2) to compute a discrete-time flux linkage representation.

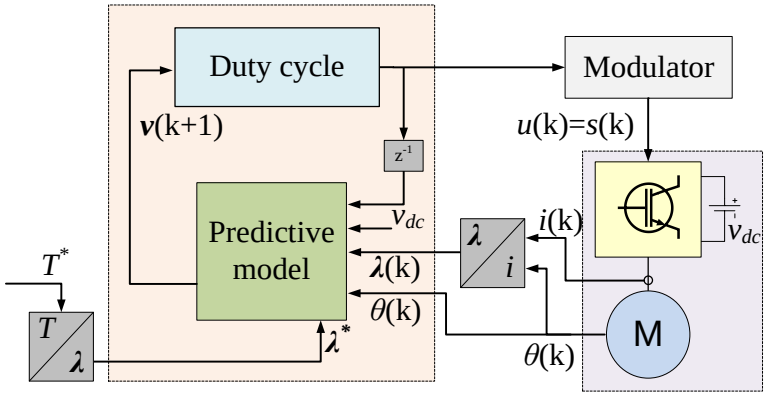

Figure 3.3: Block diagram of virtual flux deadbeat predictive control (VF-DBPC)

Whether cost function, hysteresis or modulator is used, the control performance depends on the accuracy of their predictive model, cost function and the ability to distribute the total torque within the individual torque contributions for each phase. These features are discussed next.

3.2.1 **Phase torque distribution**

The torque ripple problem in SRMs is originated during the phase transition. Figure 3.4 shows adopted strategies in the literature for PTC in SRMs. The simplest approach is to use pre-calculated torque distributions, it means, adopting the TSF LUTs and focus on the tracking of phase torque [34], [36]. The main advantage is the flexibility, as it works in multi-phase machines and needs a simple hysteresis loop. It can also include features like compensating for the loss of current tracking due to the back-EMF at higher speeds [26]. However, the optimal sharing of this technique is not static for every operating point, it operates mostly in the constant-torque (low-speed) region and multiple tables would be required.

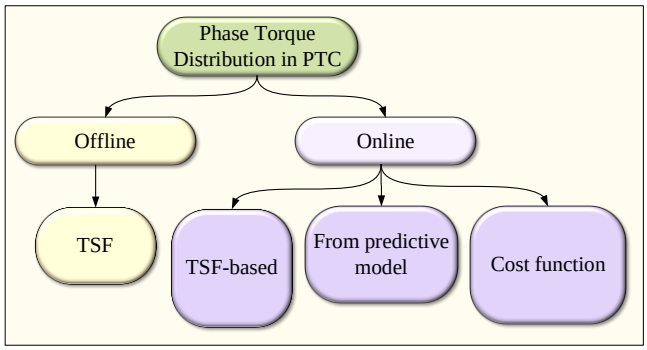

Figure 3.4: Phase torque distribution used for predictive torque control (PTC) for SRM drives

One advantage of using PTC is the possibility of letting the controller decide the optimal trajectory, thus reducing the offline computation and the uncertainty of designing regulators for unknown operating points. In that way, the principle of TSF can be implemented online, simply by considering a reference distributed among the active phases, which depend on the rotor position. One of the phases provides its maximum torque, based on static maps, and the remaining reference torque is distributed to the next phase [17], [78], [81]. It also applies to multi-phase topologies considering the maximum torque contribution of each active phase and penalizing those with less efficiency [76], [77]. The problem is again reduced to a single-phase torque tracking, but the interaction of all phases for further improvement is not considered.

An alternative appears on including the torque distribution implicit within the controller [75]. The predictive control can be integrated, for instance, with DTC in the d-q rotating frame to improve its performance [37]. Besides, the representation of torque in the VF domain helps to simplify this process.

Finally, it is common to use the flexibility of the cost function in FCS-MPC to obtain an optimal distribution. Comparing a torque reference with a prediction of all possible torque contributions from all possible switching states allows determining the optimal trajectory online [18], [21], [31], [33], [35]. The comparison can also be implemented in the VF-domain [37], [38]. However, its performance in the four-quadrant operation is not reported, and it is difficult for the

cost function to consider advanced turn-on angles for high-speed operation as this would penalize the cost with a temporally negative torque. Incapability of FCS-MPC in advancing commutation angles in the high-speed region is considered as one of the main shortcomings of this method. An adaptive commutation angle control method is proposed in [32] to extend the operating speed range of FCS-MPC for SRM drives.

3.2.2 **Predictive model**

Beyond the torque distribution or not, the effectivity of predictive control relies on its ability to track these references. The performance depends on the accuracy of the predicted variables and the model. Modelling in torque control of SRM is more complex than current control because it requires two models to operate: the flux linkage and torque characteristics, which are highly nonlinear, as in Figure 2.2. In general, the objective is to predict the torque in order to decide the input sequence that produces the minimum tracking error. Then, it is common to assume an inductance or flux model and compute the torque from the definition using equations (2.4) or (2.6). Therefore, if a proper representation of the flux linkage λ is obtained, an accurate torque can be predicted. Figure 3.5 summarizes the models used in PTC for SRM.

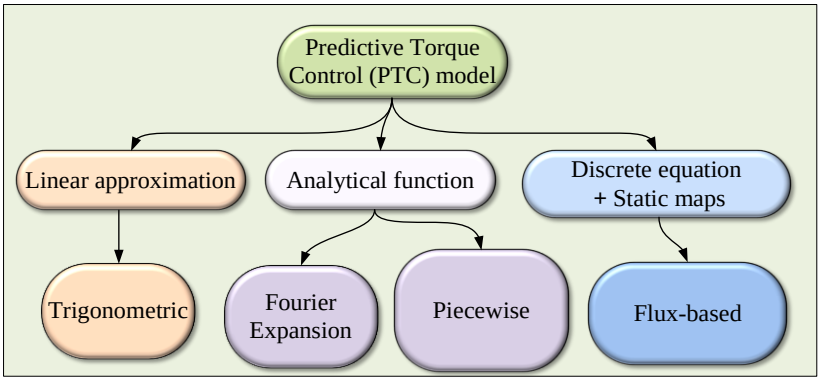

Figure 3.5: Modeling techniques used for predictive torque control in SRM drives

The simplest approach is to define the inductance as a linear function of rotor position, while the torque is computed from the equivalent flux characteristic [31], [79]. This inductance can be determined, for instance, as a function of the average inductance L_{av} and the difference between maximum and minimum inductance ΔL:

$$L = L_{av} - \Delta L \cos(\theta). \tag{3.1}$$

The use of Fourier expansion to represent the nonlinear characteristic is also considered. By tuning the Fourier coefficients, it is possible to represent the flux linkage characteristic as an analytical expression as shown in the following equation [18], [31]:

$$\begin{gathered} \lambda = \lambda_s\left(1 - e^{-p(\theta)i}\right) \\ p(\theta) = \alpha + \beta \cos(q) + \gamma \sin(q) \\ q = N_r\theta - (j-1)2\pi/3 \end{gathered} \tag{3.2}$$

In this equation, j represents the active phase. α and β are constants to be tuned experimentally. λ_s is the flux linkage under saturation. The use of this analytical expression allows obtaining derivative terms to compute torque.

A variation of equation (3.2) simplifies the model using the piece-wise relation $p(\theta)$. It allows expressing the flux as a function of the current separated from rotor position. The model was originally proposed in [82] and adapted to PTC [21], [33], [34], [37], [38], [75]:

$$p(\theta) = \begin{cases} 128\frac{\theta^3}{\pi^3} - 48\frac{\theta^2}{\pi^2} + 1 & \theta \in [0, \pi/4] \\ f\left(\frac{\pi}{2}\right) - \theta & \theta \in [\pi/4, \pi/2] \end{cases}. \tag{3.3}$$

The use of analytical equations allows a fast execution time on the microprocessor, but it comes at the expense of reduced prediction accuracy. Accurate modeling of the nonlinear characteristics of the SRM using closed-form analytical equations is a challenging task. An alternative is to use the flux-based equation in equation (2.2) and obtain a more accurate behavior of the machine using static maps [17], [32], [36], [76]–[78]. There is a compromise between the memory usage and accuracy of prediction model by defining the size of the flux and torque static maps. In practice, it is possible to optimize the trade-off between the allocated memory space and achieving a satisfactory performance [83].

3.2.3 Calculation of reference voltage

From Table 3.1, it is notorious that only cost functions and direct calculations are implemented in PTC for SRM to obtain the actuating variable of the control loop. DBPC uses the predictive model to define the switching pattern in form of a reference voltage, which is applied to the converter through a modulator. This calculation can be performed through various methods. For instance, the phase currents can be represented in a rotating reference frame like in AC drives, and the d-q-axis flux linkage can be use in a DTC-based strategy [53]. In this case, the reference voltage is also defined in the rotating frame and implemented through a space vector modulation stage. Another way is to use the natural variables and map them in the VF-domain. This procedure allows using simple discretization techniques to compute the reference voltage using the desired and the previously estimated virtual flux [17], [75]–[78].

The use of a cost function is the other adopted approach for PTC. Figure 3.6 shows the typical objectives included in the cost function using FCS-MPC.

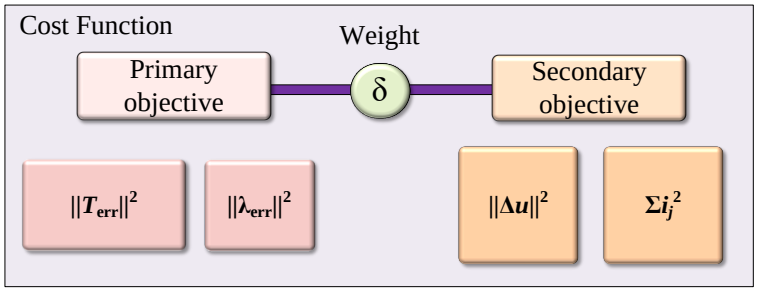

Figure 3.6: Cost function objectives in FCS-MPTC for torque control in SRM drives

A simple quadratic cost function helps achieving a single target like minimizing the torque error T_{err} and choosing between the finite switching states [36]. The advantage of a cost function is its simplicity of including control objectives, then it is recommended to use more than one. The primary objective is either torque error [18], [21], [31], [32], [34], [35] or virtual-flux error λ_{err} minimization [37], [38]. If more than one target is pursued along with the constraints, one or more weight factors δ are usually used to create a multi-objective cost function. Tuning the weight factors to achieve the optimal performance in the entire operating range is a challenging task. A cost function with adaptive time-varying weights is proposed as a solution in [84]; however, it increases the complexity of the control scheme. Secondary objectives include minimization of the phase currents to optimize efficiency [18], [21], [31]–[33], [35], or minimization of switching transitions Δu to optimize switching losses [18], [21], [31], [35]. However, from the design of predictive control, it is not recommended to cost the input since it compromises dynamic response, which is one of the most attractive features in these family of control techniques. Finally, limitations are also considered, as the maximum current I_{max} penalizes the cost if the $i(k) > I_{max}$, thus avoiding that solution option [31].

An alternative to fix the switching frequency and improve the dynamics of the phase current is the use of virtual states. Instead of using the converter states, a group of virtual states are evaluated, which can be synthetized by a modulator stage

and the volts-second approach [33]. Although the f_{sw} is constant, the drawback is the increase in its average value.

3.2.4 Modulation scheme and switching behavior

Both PWM from a duty cycle [17], [75]–[78] and SVM [33], [79] modulation can be integrated with predictive control schemes. The modulator is required for CCS-MPC, GPC or DBPC methods, and it leads to achieve a constant switching frequency, which results in a better loss distribution among the switches. However, it increases the complexity of the control scheme and reduces the speed of the dynamic response.

Similar to DTC and hysteresis controller, one of the advantages of FCS-MPC is eliminating the modulator [18], [21], [31], [32], [34]–[38], [81], but the variable switching frequency of this method can also raise some problems related to loss distribution and thermal management of the semiconductor devices. The attempt of getting the dynamics of FCS and a fixed switching frequency appeared with the use of virtual voltages, in which an optimum voltage $v_{vv} < v_{dc}$ is applied to the converter during the same sampling period, just like the volts-second strategy in SVM [33].

Either hard or soft switching can be implemented with the predictive control, but soft switching is generally preferred given the higher number of possible switching states and thus more degrees of freedom. It results in a smoother current and torque

control and reduces the voltage stress (dv/dt) on the switches. With FCS-MPC, these advantages come at the expense of increased computational burden. In a three-phase SRM, the number of evaluated states increases from 8 in hard switching to 27 in soft switching.

3.3 Summary

In this chapter, a comprehensive literature review is presented on predictive torque control approaches for SRM drives. After, classifying the predictive control methods, the characteristics and specifications of both conventional and predictive torque control methods along with the corresponding references are presented and discussed. Finally, the predictive methods are compared and analyzed in terms of phase torque distribution techniques, the implemented predictive mode, calculation of reference voltage, modulation scheme and switching behavior. The implementation of the conventional FCS-MPTC which is the most common predictive torque control approach for SRM drives and its shortcomings in adaptively adjusting the commutation angles for high-speed torque control applications will be presented in the next chapter.

Chapter 4

Implementation of Conventional Finite Control Set Model Predictive Torque Control (FCS-MPTC) for SRM and its Shortcomings

The implementation of the conventional finite control set model predictive torque control for switched reluctance motor drives along with the simulations results on the test SRM1 are presented in this chapter. Then, the shortcomings of the conventional FCS-MPTC in controlling the SRM at high-speed range are described and discussed through simulation results. The experimental setup will then be explained and the experimental test results of the test SRM2 with the conventional FCS-MPTC are presented and discussed.

4.1 Implementation of conventional FCS-MPTC

In Finite Control Set Model Predictive Control (FCS-MPC), an optimal control voltage vector corresponding to the minimum cost is selected among the finite set

of all possible voltage vectors. The cost for the motor control is usually formulated to achieve a reference torque, reference current, or speed along with certain constraints. The control voltage vectors are essentially the possible switching states of an inverter. An SRM is driven by asymmetric bridge converter and the per-phase circuit is shown in Figure 2.6. Depending on the switching state of the switches (S_1 and S_2), the phase voltage can be $-V_{DC}$, 0 or $+V_{DC}$. Therefore, there are three different possible switching states for each phase at each sampling time. Considering a three phase SRM, 3^3=27 different switching states are possible. The optimal switching state is selected from these twenty-seven switching states in a sampling interval if the prediction horizon is one. The computational burden of FCS-MPC increases exponentially with the length of the prediction horizon. For example, 27^2=729 possible switching states need to be evaluated for two prediction length.

The model of SRM to predict the future states in FCS-MPC is

$$v = Ri + \frac{d\lambda}{dt} \tag{4.1}$$

where v, R, i and λ stand for phase voltage, phase resistance, phase current, and phase flux linkage. λ is a 2D look-up table and it varies with both rotor position and phase current as shown in Figure 2.2-a. The discrete version of equation (4.1) using forward Euler method is

$$v(k) = Ri(k) + \frac{\lambda(k+1) - \lambda(k)}{T_s} \tag{4.2}$$

where T_s is the sampling interval. Then, the flux linkage of the SRM at one future time step (time instant k+1) can be obtained using

$$\lambda(k+1) = \lambda(k) + T_s\big(v(k) - Ri(k)\big). \tag{4.3}$$

The flux linkage at time instant k+1 is a function of the current machine states and the switching state, which is going to be applied at sampling instant k.

From the flux linkage-position-current characteristic of the test SRM1, given in Figure 2.2-a, it can be observed that flux linkage is a function of the rotor position and the phase current. Hence, using both current and position feedbacks, the flux linkage of the machine at time instant k, $\lambda(k)$ can be found from the flux linkage LUT in Figure 2.2-a:

$$\lambda(k) = \lambda\big(i(k), \theta_{mech}(k)\big). \tag{4.4}$$

Once the flux linkage at time k is known, the flux linkage at time (k+1) is estimated from equation (4.3). As the time constant of the electrical dynamics is much lower than the mechanical dynamics, the speed can be assumed as a constant in one sampling time. Hence, the mechanical position at time k+1, $\theta_{mech}(k+1)$ can be found as

$$\theta_{mech}(k+1) = \theta_{mech}(k) + \frac{360}{60} n_r T_s \tag{4.5}$$

where n_r is the rotor speed in rpm. Once both the flux linkage and rotor position at time instant k+1 are known, the phase current can be found at time k+1 from the flux linkage LUT in Figure 2.2-a:

$$i(k+1) = i\big(\lambda(k+1), \theta_{mech}(k+1)\big). \tag{4.6}$$

Phase torque can then be calculated using the torque LUT Figure 2.2-b:

$$T_{phase}(k+1) = T_{phase}\big(i(k+1), \theta_{mech}(k+1)\big). \tag{4.7}$$

Finally, the total torque can be determined by summing up the torque produced by the individual phases:

$$T_e(k+1) = \sum_{j=1}^{m} T_j(k+1) \tag{4.8}$$

where *m* is the number of phases, which is three for both the reference machines in this thesis. Using equations (4.3)-(4.8), all the required future states of the SRM can be found. Phase voltage at time instant *k*, *v*(*k*) is the only unknow in equation (4.3), which is the decision variable for the FCS-MPC to determine. As stated earlier, there are 27 different possible switching states for the reference 3-phase SRM. The future states of the machine are predicted using equations (4.3)-(4.8) for all the possible switching states. The state (voltage vector) which minimizes the objective function of FCS-MPC is selected and applied to the machine by commanding the corresponding gating signals to the asymmetric bridge converter. The objective function in this thesis includes both the terms to track the instantaneous reference torque and to minimize the instantaneous current:

$$f_{MPC} = \big(T_e(k+1) - T_{ref}\big)^2 + k_{MPC}\frac{\sum_{j=1}^{m} i_j^2(k+1)}{mI_{max}^2} \tag{4.9}$$

where T_{ref}, i_j, and I_{max} are the reference torque, instantaneous phase current of phase j, and the peak current limit of the machine (I_{max}=21A for SRM1), respectively. Sum of three instantaneous phase currents is normalized by mI_{max}^2. The coefficient k_{MPC} determines the weight of the current minimization term with respect to the torque tracking term. If k_{MPC} is set to be too small, then MPC does not care about the current and, instead, focuses on tracking the reference torque, which could lead to high RMS currents and lower efficiency. On the other hand, a large weighting factor reduces the RMS current (current waveform gets smoother as well), but the reference torque tracking deteriorates and leads to steady state torque error. After conducting simulations at different operating points in the torque-speed envelope of the reference SRM, the weighting factor is set to be k_{MPC}=5 for SRM1 and k_{MPC}=2 for SRM2 in all the analysis in this thesis.

The block diagram of the FCS-MPTC is shown in Figure 4.1. As discussed earlier, current, position and speed feedbacks are required to calculate the future state of the machine. After estimating the flux linkage $\lambda(k)$ using equation (4.4), immediate future states of the SRM are predicted for all possible switching vectors. The optimum switching state which minimizes the cost function is then calculated and applied in each sampling time.

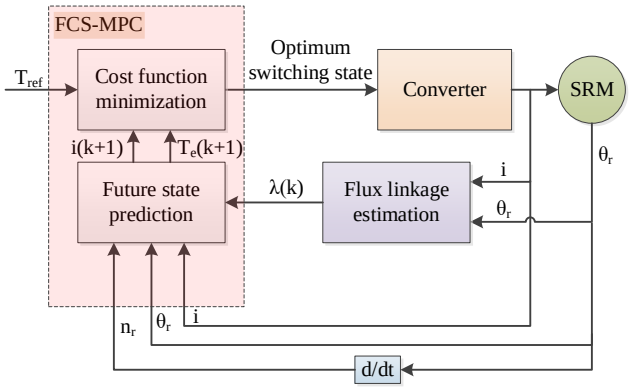

Figure 4.1: Block diagram of the FCS-MPTC

4.2 Shortcomings of conventional FCS-MPTC

The FCS-MPTC with a single prediction horizon decides the optimum switching states based on only the immediate future state of the machine. Therefore, MPC keeps a phase excited if it can develop positive torque. Once MPC finds that the excited phase generates negative torque in the immediate future, then it shuts down the phase and does not take the upcoming negative torque production by the demagnetizing currents into account. In this manner, MPC always turns-off the phase close to the aligned position regardless of the speed.

The results from a MATLAB Simulink simulation of the FCS-MPTC for SRM1 are shown in Figure 4.2 for the case without turn-off angle control for n_{ref} = 2000 rpm (low speed) and T_{ref} = 3 Nm. The simulation models are implemented according to the block diagram in Figure 4.1. SRM is in torque control mode and

runs at a constant speed, which is controlled by the load motor (not shown in Figure 4.1).

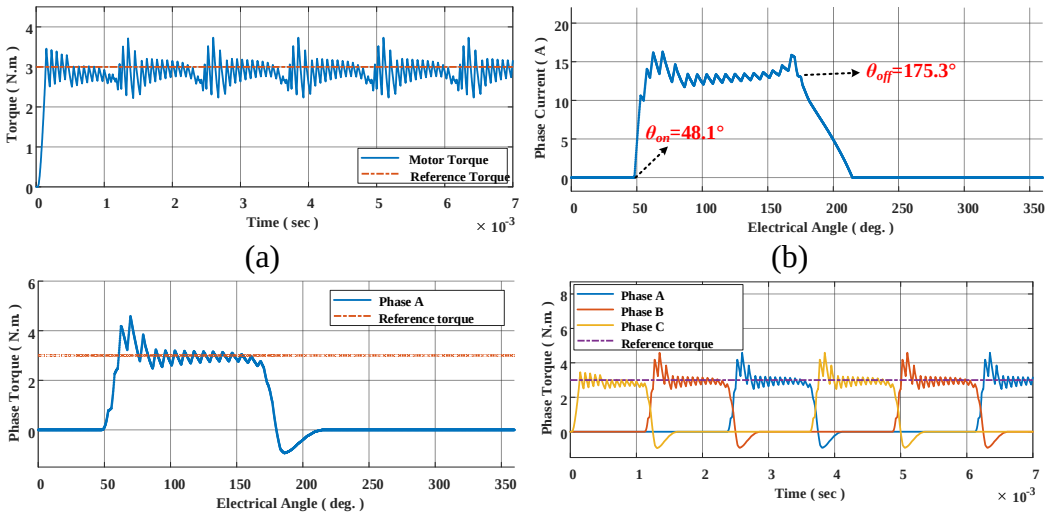

Figure 4.2: Simulation results of the test SRM1 with the conventional FCS-MPTC at n_{ref}=2000 rpm (low-speed) and T_{ref}=3 Nm without the turn-off angle control; (a) total torque, (b) phase current in one electrical cycle, (c) phase torque in one electrical cycle, and (d) phase torques.

Figure 4.3 shows the simulation results of SRM1 for n_{ref} = 6000 rpm (base speed) and T_{ref} = 1.5 Nm. The sampling time of the simulations is 50 µs. Hence, the maximum switching frequency of FCS-MPTC is 20 kHz. At lower speeds, the induced back emf is low and, hence, the current can rapidly decay to zero after the phase is turned off as shown in Figure 4.2-b. However, at high speed, higher induced emf slows down the rate of change of current, as shown in Figure 4.3-b. As a result, the phase still conducts even after the aligned position (generating region) for a considerable duration. Consequently, the conducting phase produces significant negative torque and the upcoming phase needs to compensate that by producing high positive torque, which is undesirable. The upcoming phase needs

higher current to produce the same torque magnitude as compared to the conducting phase, due to the difference in the rate of change of inductances. This results in high RMS current, low torque per ampere ratio, and lower efficiency. Therefore, the FCS-MPTC without the turn-off angle control is not the right choice to control the SRM, especially in the high-speed region.

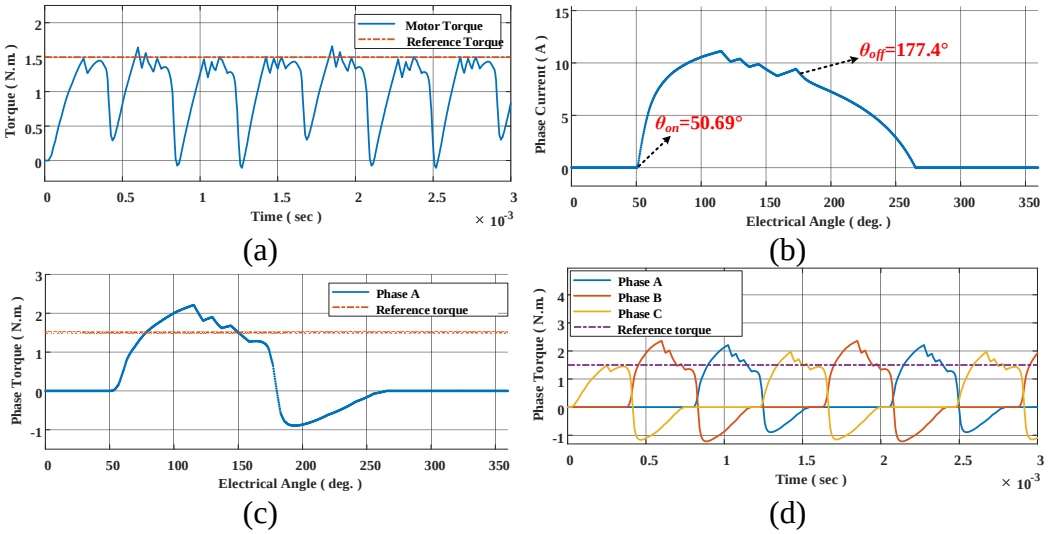

Figure 4.3: Simulation results of the test SRM1 with the conventional FCS-MPTC at n_{ref}=6000 rpm (base speed) and T_{ref}=1.5 Nm without the turn-off angle control; (a) total torque, (b) phase current in one electrical cycle, (c) phase torque in one electrical cycle, and (d) phase torques.

The negative torque production can be avoided by advancing the phase turn-off angle so that the phase current reaches zero before entering to the inductance falling region which starts from 180° electrical. The correct turn-off angle can be identified by predicting the demagnetizing current at each sampling interval. Once it is found that turning off a phase at a sampling instant results in zero current at 180° electrical, the corresponding angle at that sampling instant can be chosen as the turn-off angle. The concept is shown in Figure 4.4. By integrating this concept into the FCS-

MPTC, it automatically advances the phase turn-on angle to avoid negative torque production.

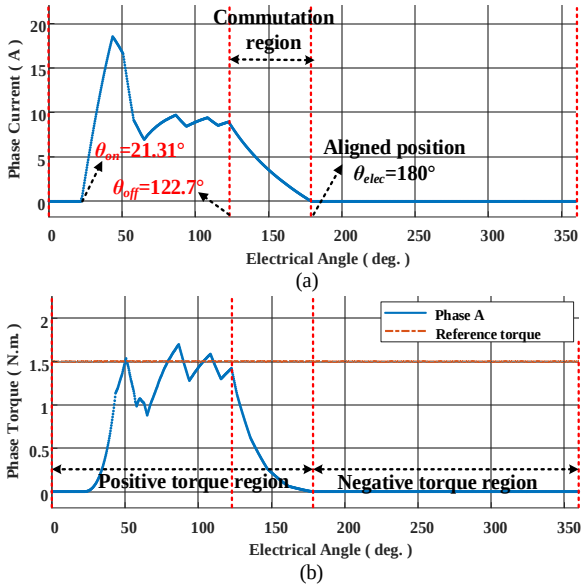

Figure 4.4: Graphical representation of the turn-off angle control to achieve zero negative torque (The waveforms are for SRM1 at n_{ref}=6000 rpm and T_{ref}=1.5 Nm); (a) phase current in one electrical cycle, and (b) phase torque in one electrical cycle.

Simulation results of SRM1 for this case are presented in Figure 4.5 for n_{ref}=6000 rpm and T_{ref}=1.5 Nm. It can be observed from Figure 4.5-a that the torque ripple is slightly reduced compared to Figure 4.3-a (without turn-off angle control). The turn-off angle is 122.7° (see Figure 4.4-a) to let the phase current decay to zero before the aligned position (180° electrical). FCS-MPTC also advances the turn-on angle to 21.31°, as can be seen in Figure 4.4-a, to maintain the reference torque tracking while eliminating negative torque production. However, the test SRM has lower torque production capability at positions close to θ_{elec}=0° (unaligned

position) as seen in Figure 2.2-b. Hence, a considerable part of torque production capacity of the machine is not well utilized by including turn-off angle control into FCS-MPTC. Moreover, due to the low torque production capability of the SRM close to the unaligned position, phase current increases as the turn-on angle is advanced (see Figure 4.4-a).

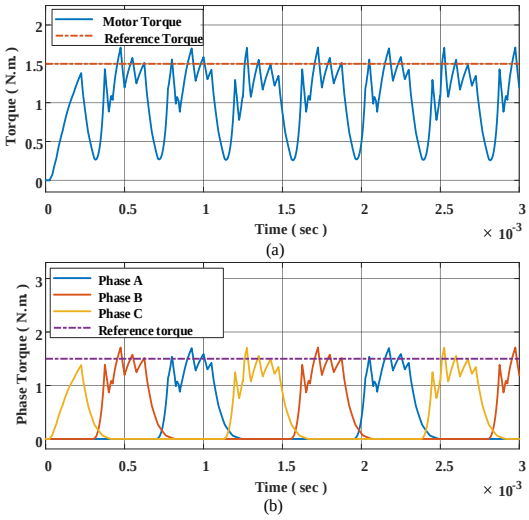

Figure 4.5: Simulation results of the test SRM1 with FCS-MPTC at n_{ref}=6000 rpm (base speed) and T_{ref}=1.5 Nm with zero negative torque; (a) total torque, and (b) phase torques.

In order to overcome these shortcomings of the turn-off angle control, a small negative torque could be allowed by slightly shifting the commutation angles towards the aligned position. For this purpose, an optimum turn-off angle that results in better utilization of the torque production capability with lower current and negative torque, is proposed. Two online and one optimization-based offline methods are proposed in this thesis to adaptively control the commutation angles in FCS-MPTC for SRM drives in the wide operating speed range.

4.3 Experimental setup

In this thesis, the proposed methods are experimentally validated on a 5.5 kW, 12/8, 3-phase SRM (will be referred to as SRM2 in this thesis) drive with the base speed of 5000 rpm and the DC link voltage of 72 V. An asymmetric bridge converter equipped with liquid cooling is used to control the SRM. The shaft speed is controlled by a 3-phase, 15 kW fully enclosed, air-cooled IPMSM driven by a Sevcon Gen 4 S4 72V, 350 A AC motor controller in a back to back configuration. The experimental setup is shown in Figure 4.6.

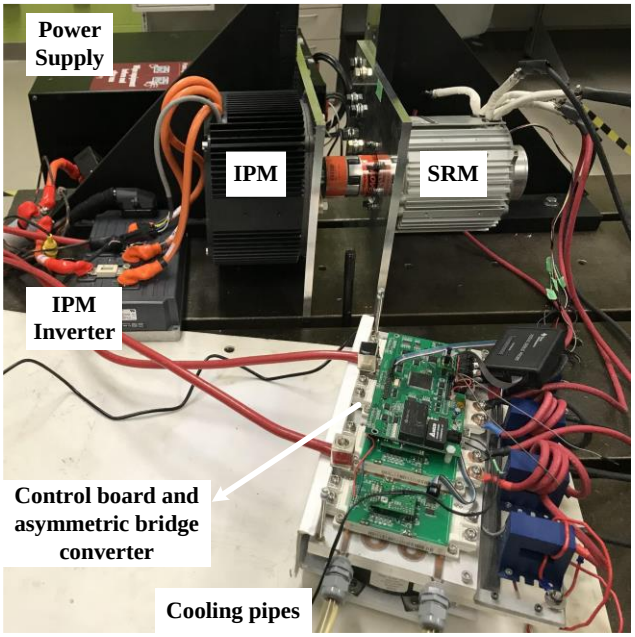

Figure 4.6: Experimental Setup

The specifications of both SRM2 and the dyno IPMSM motors are given in Table 4.1.

Table 4.1: Specifications of SRM2 and the dyno motor

SRM2		**IPMSM**	
Parameter	Value	Parameter	Value
Configuration	12/8, 3-phase	Number of phases	3
Power	5.5 kW	Power	15 kW
Base speed	5000 rpm	Speed	4500 rpm
Torque	10.5 Nm	Torque	37 Nm
Rated current	81.7 A	Phase current	220 A
Peak power	11 kW	Peak power	42 kW
Maximum speed	10000 rpm	Maximum speed	8000 rpm
Phase resistance	7.6 mΩ	Maximum torque	107 Nm
DC link voltage	72 V	DC link voltage	48-120 V

The flux linkage-position-current characteristic of SRM2 is obtained by locking the rotor at different positions (between unaligned and aligned positions in both motoring and generating regions) and applying the phase voltage pulses. The measured flux linkage characteristic of the test SRM2 is presented in Figure 4.7-a. The torque-position-current characteristic of the test SRM2 is then obtained based on the co-energy concept and using equation (2.6). The torque characteristic is depicted in Figure 4.7-b.

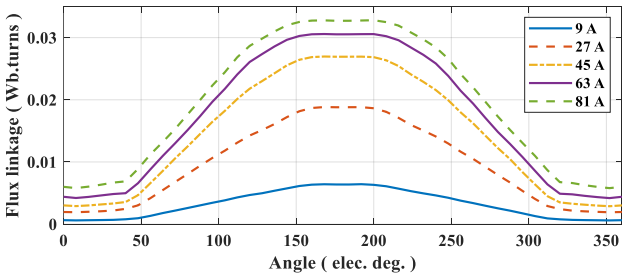

(a)

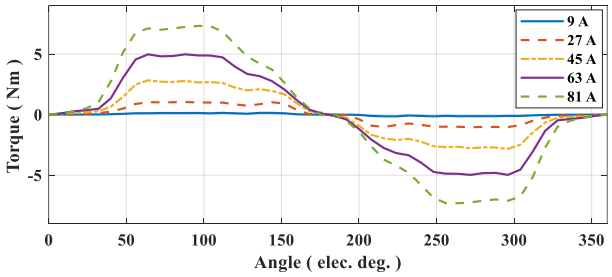

(b)

Figure 4.7: Static characteristics of the test SRM2; (a) flux linkage-position-current, and (b) torque-position-current

The nonlinear phase inductance of the test SRM 2, calculated from the flux linkage data is presented in Figure 4.8.

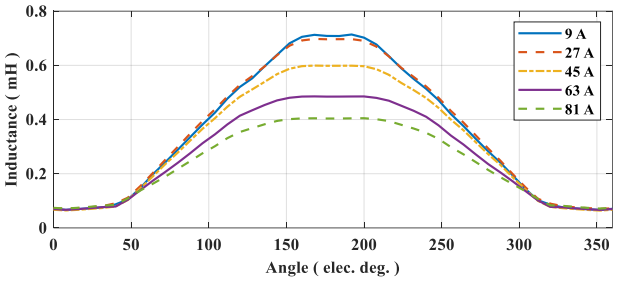

Figure 4.8: Measured inductance-position-current characteristic of the test SRM2

4.3.1 **Experimental results for conventional FCS-MPTC**

The conventional FCS-MPTC is implemented in real-time on the DSP platform (Texas Instruments C2000 F28335 microcontroller) to validate the performance of the predictive methods experimentally. In the experimental tests, the SRM operates in torque control mode (operating with FCS-MPTC), and the dyno IPMSM operates in speed control mode to keep the shaft speed constant at the desired reference. The sampling frequency of the predictive controller is set to 20 kHz, hence the sampling

time is 50 µs. However, the average switching frequency will be lower than 20 kHz, as FCS-MPTC is a variable frequency control strategy. To have a fair comparison, the control frequency is set to 20 kHz in all the experimental results in this thesis. A single step delay compensation has also been applied to the predictive controller to compensate for the measurement delays and the computation time. The experimental results of the conventional FCS-MPTC at 2000 rpm with the reference torque of 3 Nm are presented in Figure 4.9. The measured phase current and phase torque in one electrical cycle are shown in Figure 4.9-b and c, respectively. Because of the low bandwidth of the torque sensor, it is not feasible to compare the measured torque ripples at higher speeds, hence, the phase torques, and the shaft torque is estimated by recording the phase currents and the electrical angle of Phase A (through digital to analog conversion (DAC)), and using the corresponding torque-position-current characteristic of the test SRM2. The measured phase currents and the estimated phase torques are depicted in Figure 4.9-d and e, respectively. The total torque which is calculating by summing up the torque generated by individual phases is shown in Figure 4.9-a. Based on Figure 4.9-b, it can be observed that the current can quickly decay to zero after the turn-off angle and the generated phase negative torque is negligible (see Figure 4.9-c). Because of incapability of the conventional FCS-MPTC in controlling the commutation angles, huge phase current peaks (around 150 A) are observed as can be seen in both Figure 4.9-b and Figure 4.9-d.

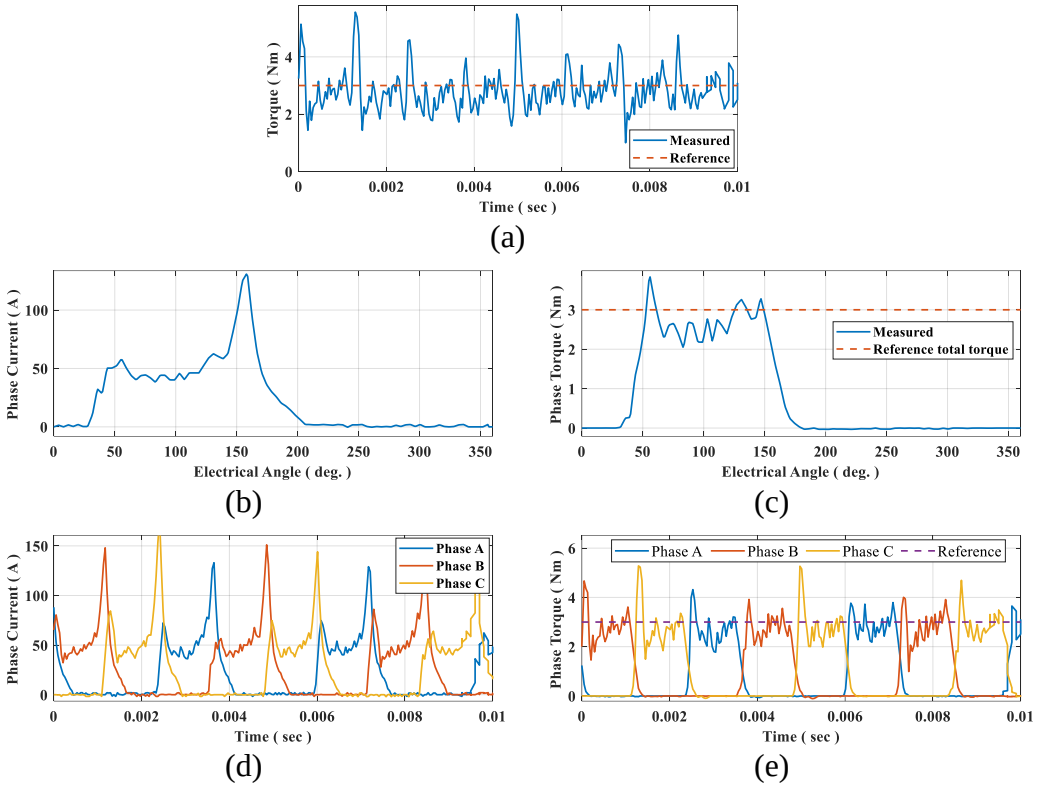

Figure 4.9: Experimental test results of SRM2 with the conventional FCS-MPTC (20 kHz) at n_{ref}=2000 rpm (low-speed) and T_{ref}=3 Nm; (a) torque, (b) phase current in one electrical cycle, (c) phase torque in one electrical cycle, (d) phase currents, and (e) phase torques.

The experimental test results at 4000 rpm under load torque of 3 Nm are presented in Figure 4.10. According to the phase current waveform given in Figure 4.10-b, due to the increased back-emf at higher speed, there is a big current tail in the generating region after the phase is turned off resulting in the negative phase torque as can be seen in Figure 4.10-c and e. The upcoming phase tries to compensate for this negative torque by increasing the phase current to deliver the reference torque on the shaft. However, it can be observed from Figure 4.10-a that the torque ripple is significantly bigger compared to low-speed operation. Besides, the average shaft

torque is considerably lower than the reference torque. Similar to the low-speed operation, big phase current peaks are observed as can be seen in both Figure 4.10-b and d.

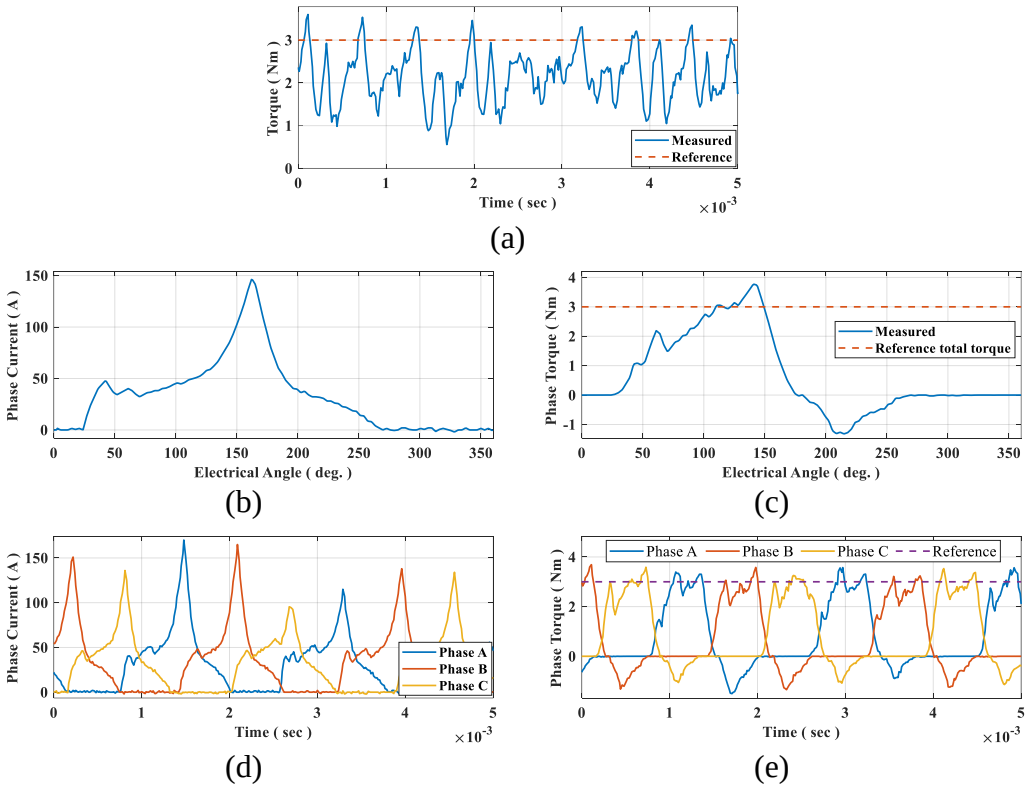

Figure 4.10: Experimental test results of SRM2 with the conventional FCS-MPTC (20 kHz) at n_{ref}=4000 rpm and T_{ref}=3 Nm; (a) torque, (b) phase current in one electrical cycle, (c) phase torque in one electrical cycle, (d) phase currents, and (e) phase torques.

Two online and one offline adaptive commutation angle control strategies are proposed in three following chapters to improve the performance of the conventional FCS-MPTC for SRM drives.

4.4 Summary

The implementation of the conventional single prediction horizon FCS-MPTC for SRM is presented in this chapter. The discretized voltage equation to predict the future state of SRM and the block diagram of FCS-MPTC are given and discussed. After presenting the simulation results of the conventional FCS-MPTC in both low-speed and high-speed regions, its shortcomings in controlling the commutation angles at different speeds are discussed based on the simulation results. It is concluded that a specific amount of phase negative torque needs to be allowed by controlling the turn-off angle to achieve the optimal performance in terms of torque ripple and copper losses. The experimental setup is briefly described and the specifications of the test SRM2 and the dyno IPMSM are given. Finally, the experimental results of the test machine in both low-speed and high-speed regions are presented and discussed. In the following three chapters, three methods (two online and one offline) will be proposed to adaptively control the commutation angles in both low-speed and high-speed ranges.

Chapter 5

First Online Adaptive Turn-Off Angle Control for FCS-MPTC of SRM Drives

This chapter presents an online adaptive method to adjust the phase turn-off angle in finite control set model predictive torque control (FCS-MPTC) of SRM drives to reduce the negative torque production. The current in the inductance falling region generates negative torque which increases the torque ripple, RMS current, and reduces the efficiency, especially at high-speed operation. The existing FCS-MPTC needs long prediction horizon to predict and reduce the negative torque production by adjusting the turn-off angle. However, long prediction horizon substantially increases the computational burden. A simple online method to automatically adjust the phase turn-off angle for single prediction horizon FCS-MPTC is proposed in this chapter. To reduce the computational burden of FCS-MPTC, a sector partition technique is also proposed in this chapter. The proposed method can allow for the negative phase turn-on angle while reducing the computational burden significantly. The proposed commutation angle control

method is validated in simulations for a three phase, 12/8, 2.3 kW SRM (SRM1) in the entire operating region. The comparison with the existing FCS-MPTC shows the effectiveness of the proposed method in terms of efficiency and torque ripple reduction. The experimental test results of the test SRM2 with the proposed commutation angle control method are also presented at both low-speed and high-speed operating points.

5.1 Proposed first online method

An online adaptive method to find the optimal turn-off angle for FCS-MPTC in the whole speed range is proposed in this section. The proposed method is based on predicting the phase demagnetizing current for an extended time interval, and the prediction horizon for FCS-MPTC is kept as one. As depicted in Figure 5.1, the optimality condition for the turn-off angle is chosen in such a way that the maximum allowable conduction time in the generating region (negative torque region) ($\Delta\theta_2$) should be equal to the time interval ($\Delta\theta_1$) between the phase turn-off instant and the aligned position (θ_{elec}=180°). This optimality criteria allows considerable positive torque while limiting the negative torque production. In other words, in each sampling interval, after predicting the demagnetizing current in the extended time interval, if the optimality condition for the turn-off angle is not satisfied, the single prediction horizon FCS-MPTC applies the optimum switching state that minimizes the cost function in equation (4.9). Once the optimality

condition is met, the conducting phase is turned off, and FCS-MPTC starts energizing the upcoming phase to achieve the torque reference.

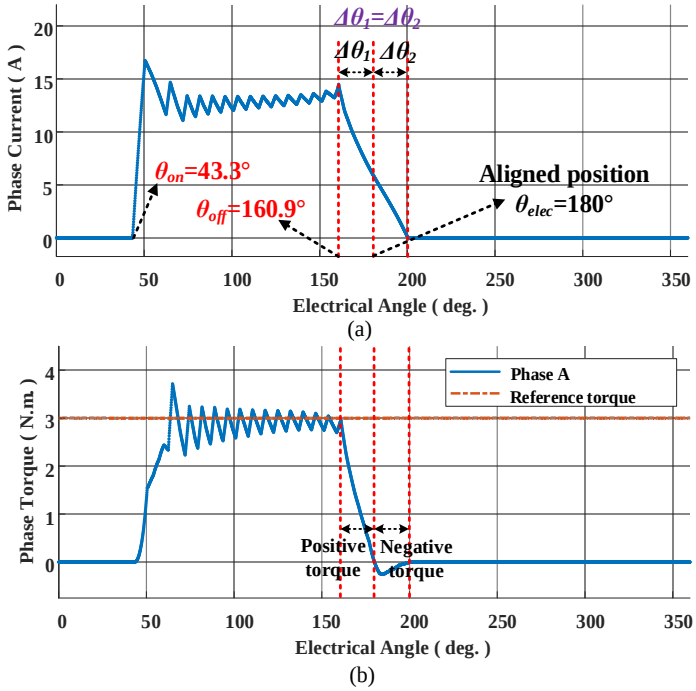

Figure 5.1: Graphical representation of the proposed online turn-off angle control method (The waveforms are for SRM1 at n_{ref}=2000 rpm and T_{ref}=3 Nm); (a) phase current in one electrical cycle, and (b) phase torque in one electrical cycle.

The turn-off angle usually lies in the interval of [90°, 180°]. So, in the proposed scheme, $\Delta\theta_1$ and $\Delta\theta_2$ are calculated from the predicted phase demagnetizing current at each sampling interval. The voltage across the phase in the demagnetization period is $-V_{DC}$. Therefore, the per-phase voltage equation in this time interval is

$$-V_{DC} = Ri + \frac{d\lambda}{dt} = Ri + L(\theta, i)\frac{di}{dt} + i\frac{dL(\theta, i)}{dt} \tag{5.1}$$

where $L(\theta, i)$ is the nonlinear phase inductance. Assuming a linear inductance variation for a small change in the rotor position, equation (5.1) can be treated as a

linear differential equation. So, the current at a future step j, i_j is predicted from the solution of equation (5.1) as

$$i_j = i_{j-1} e^{\frac{-(R+dL(\theta,i)/dt)\Delta t}{L_j(\theta,i)}} + \frac{-V_{DC}}{(R + dL(\theta,i)/dt)}\left(1 - e^{\frac{-(R+dL(\theta,i)/dt)\Delta t}{L_j(\theta,i)}}\right) \quad (5.2)$$

where $L_j(\theta, i)$ and Δt are the phase inductance at future step j and the time difference between steps j-1 and j. i_{j-1} is the current from the previous time step and it is used as the initial value in the current time step. The nonlinear inductance look-up table is used to calculate $L_j(\theta, i)$. At each sampling instant, the current i_j is predicted until it becomes zero. Then, the corresponding $\Delta\theta_1$ and $\Delta\theta_2$ are found. This process is repeated for each sampling interval until it meets the desired condition $\Delta\theta_1=\Delta\theta_2$. The rotor position corresponding to the sampling interval that meets the condition ($\Delta\theta_1=\Delta\theta_2$) is the optimal turn-off angle. Hence, the outgoing phase is turned-off at this sampling interval.

The flowchart of the proposed turn off angle control scheme is presented in Figure 5.2. Note that a delay compensation is needed in experimental implementation of both conventional and proposed predictive approaches to compensate the delay for the measurements and online computation time. Note that the calculation proposed in this flowchart is carried out for all three phases of SRM.

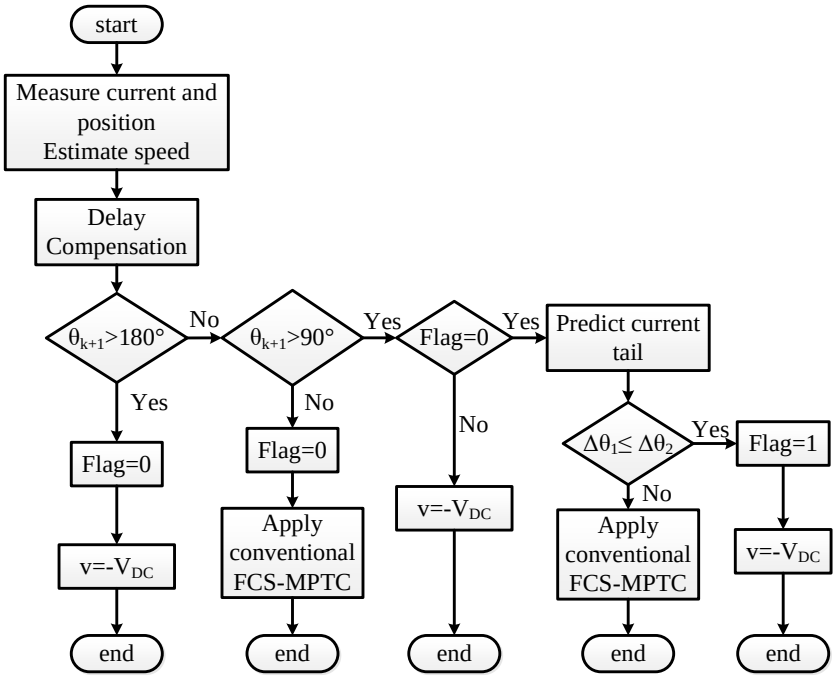

Figure 5.2: Flowchart of the first proposed online method

5.2 Proposed Sector Partition Technique

A sector partition technique is proposed in this section to reduce the computational burden of the conventional FCS-MPTC. The proposed method can allow for the negative turn-on angle, if needed. In the proposed method, each phase can be in conduction in the [-20°,180°] interval. The phase voltage is forced to be $-V_{DC}$ outside this region. The diagram of the proposed sector partition technique indicating the shut-down periods for a three-phase SRM is presented in Figure 5.3.

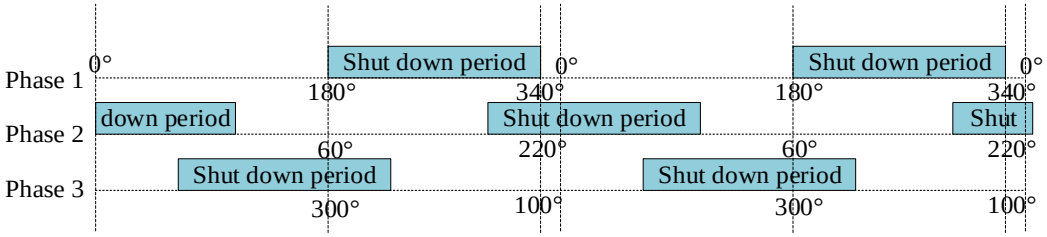

Figure 5.3: The proposed sector partition scheme

As stated earlier, 27 different switching states have to be calculated at each sample time for a 3-phase SRM. Number of future states to be predicted is reduced to 9 or 3 depending on the rotor position using the proposed sector partition scheme. In the overlap region of shut-down periods of two consecutive phases, only 3 future states need to be predicted. Otherwise, 9 different switching states are evaluated. Hence, the computational burden of FCS-MPTC is significantly reduced. The proposed sector partition scheme will be applied to both conventional and the proposed FCS-MPTC methods in this thesis.

5.3 Simulation results

The proposed method is implemented in MATLAB/Simulink. The simulation results for n_{ref}=2000 rpm and T_{ref}=3 Nm are given in Figure 5.4. Similar to the previous cases, the sampling time and maximum switching frequency are set to 50 μs and 20 kHz. It can be observed that the proposed method sets the turn-off angle to 160.9° (see Figure 5.1-a) – it was 175.3° with FCS-MPTC without the turn-off angle control. In order to track the desired reference torque, the turn-on angle is automatically set to 43.3° (Figure 5.1-a) – it was 48.1° with FCS-MPTC without

the turn-off angle control. If Figure 4.2, Figure 5.1 and Figure 5.4 are compared, it can be observed that the negative torque and, hence, the rms current is reduced under similar operating conditions.

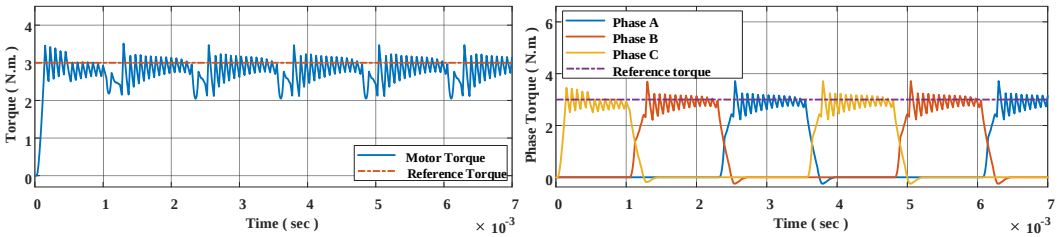

(a) (b)

Figure 5.4: Simulation results of the test SRM1 with the proposed method at n_{ref}=2000 rpm (low-speed) and T_{ref}=3 Nm; (a) total torque, and (b) phase torques.

In order to investigate the effectiveness of the proposed method at a higher speed, the same simulations are repeated for n_{ref}=6000 rpm (base-speed) and T_{ref}=1.5 Nm. The results are presented in Figure 5.5. The turn-off angle is effectively advanced to 151.5° (it was 177.4° with FCS-MPTC without the turn-off angle control) to prevent the negative torque production. The turn-on angle is also reduced to 36.29° (it was 50.69° with FCS-MPC without the turn-off angle control) to deliver the reference torque. Significant improvement in both average torque and torque ripple can be observed by comparing Figure 5.5-a and Figure 4.3-a. Comparing Figure 5.5-c and Figure 4.3-c reveals the significant reduction in the negative torque production with the proposed method. It can be observed from both Figure 5.4 and Figure 5.5 that the negative torque is significantly reduced in the proposed method.

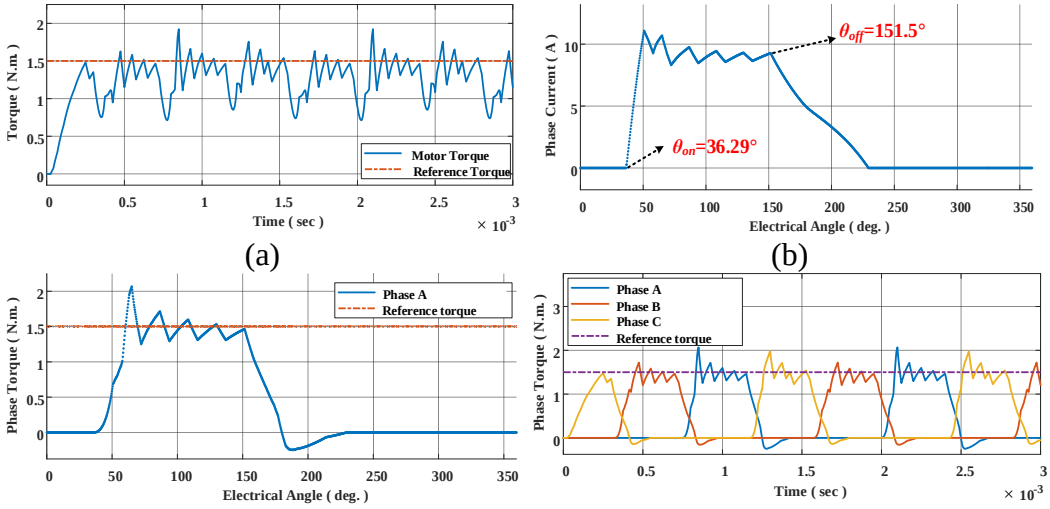

Figure 5.5: Simulation results of the test SRM1 with the proposed method at n_{ref}=6000 rpm (base speed) and T_{ref}=1.5 Nm; (a) total torque, (b) phase current in one electrical cycle, (c) phase torque in one electrical cycle, and (d) phase torques.

The simulated performance of the reference machine is summarized in Table 5.1 for FCS-MPTC with and without the proposed turn-off angle control. It can be observed that the proposed method can effectively adjust the commutation angles at both low and high-speed regions. At 6000 rpm, there is a significant improvement in the average torque. The average torque is increased by 39% for the same reference torque (T_{ref}=1.5 N.m.). The RMS current has also been reduced around 24%. Moreover, the torque ripple has been reduced from 192.6% to 73.5%. On the other hand, in the low-speed region, for 0.7% lower output torque, the RMS current is reduced around 5%. However, the torque ripple is increased from 19.6% to 36.9%. This implies that, the proposed commutation angle control method needs

to be further improved to achieve better performance at the low-speed region, but it provides significant improvement at higher speeds.

Table 5.1: Performance comparison of the test SRM1 with the existing FCS-MPTC and the proposed method

Performance parameters		θ_{on} (elec. deg)	θ_{off} (elec. deg)	T_{avg} (Nm)	I_{RMS} (A)	T_{ripple} (%)
n_r=2000 rpm T_{ref}=3 Nm	Existing MPC	48.1	175.3	2.84	8.21	19.6
	Proposed method	43.3	160.9	2.82	7.8	36.9
n_r=6000 rpm T_{ref}=1.5 Nm	Existing MPC	50.69	177.4	0.9	6.69	192.6
	Proposed method	36.29	151.5	1.25	5.1	73.5

5.4 Experimental results

To investigate the low-speed performance of the proposed commutation angle control method, the experimental test results of SRM2 at $n_{ref} = 2000\ rpm$ under the load torque of $T_{ref} = 3\ Nm$ are presented in Figure 5.6. Note that the optimal turn-off angle with the proposed method is calculated using simulations in the entire torque and speed ranges. Then, the data are stored in look up tables to incorporate in experimental implementation of the proposed method. As mentioned earlier, the weighting factor of the objective function of FCS-MPTC is kept constant at $k_{MPC} = 2$ in the conventional and proposed online methods. Similar to the experimental results with the conventional FCS-MPTC, the control frequency is set to 20 kHz. Because of the low-speed operation and lower phase back-emf, the phase current can quickly decay to zero after the turn-off angle, and the generated negative phase

torque is negligible as seen in both Figure 5.6-c and e. Hence, the turn-off angle is selected to be close to the aligned position with the proposed method (similar to the conventional FCS-MPTC). Note that the phase current peak is greatly reduced compared to the conventional FCS-MPTC with the proposed commutation angle control scheme as seen in Figure 5.6-b and d.

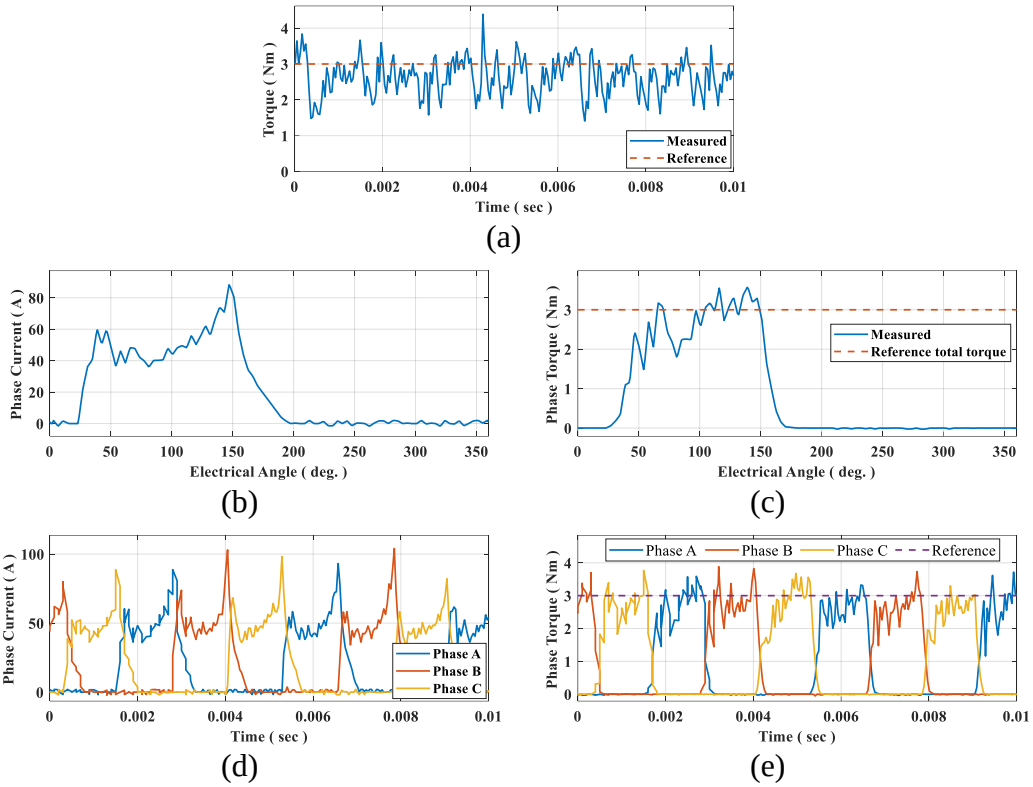

Figure 5.6: Experimental test results of SRM2 with the first online method (20 kHz) at n_{ref}=2000 rpm (low-speed) and T_{ref}=3 Nm; (a) torque, (b) phase current in one electrical cycle, (c) phase torque in one electrical cycle, (d) phase currents, and (e) phase torques.

The experimental test results of SRM2 with the proposed method at $n_{ref} = 4000\ rpm$ under the load torque of $T_{ref} = 3\ Nm$ are presented in Figure 5.7. Comparing the measured phase currents in Figure 5.7-b and Figure 4.10-b reveals

that both phase turn-on and turn-off angles are advanced with the proposed method to reduce the negative torque production in the generating region after the phase is turned off. Besides the phase current peak is considerably reduced compared to the conventional FCS-MPTC. By comparing Figure 5.7-c, and Figure 5.7-e with Figure 4.10-c and Figure 4.10-e respectively, significant reduction of the phase negative torque with the proposed method can be observed, as the current tail in the generating region is considerably shorter with the proposed method. This results in a lower rms phase current with the proposed method as can be understood by comparing Figure 5.7-d and Figure 4.10-d. By comparing Figure 5.7-a and Figure 4.10-a, it can be seen that a higher average torque is achieved with the proposed turn-off angle control method. A comprehensive performance comparison is carried out in Chapter 8.

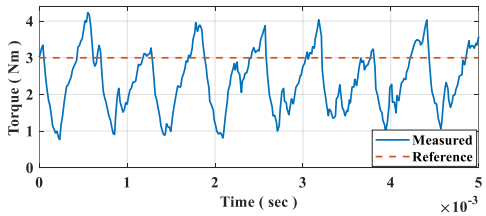

(a)

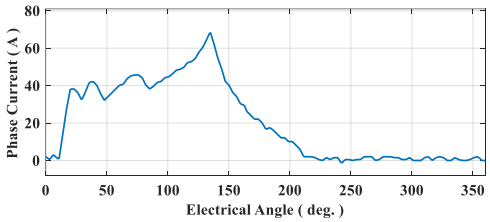

(b)

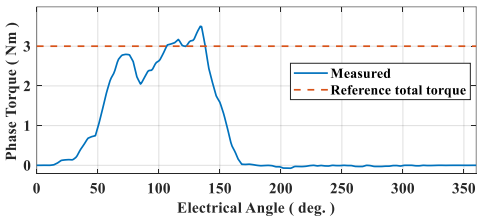

(c)

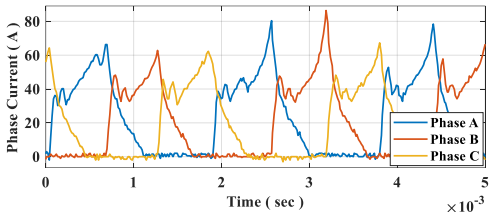

(d)

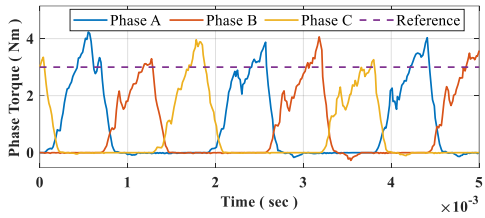

(e)

Figure 5.7: Experimental test results of SRM2 with the first online method (20 kHz) at n_{ref}=4000 rpm and T_{ref}=3 Nm; (a) torque, (b) phase current in one electrical cycle, (c) phase torque in one electrical cycle, (d) phase currents, and (e) phase torques.

5.5 Summary

An extended-speed online adaptive commutation angle control for finite control set model predictive torque control of switched reluctance motors is proposed in this chapter. As, mentioned earlier, the existing FCS-MPTC is not capable of adjusting commutation angles which limits its application especially at higher speeds where advanced commutation is needed to prevent negative torque production. The effectiveness of the proposed method in adjusting the commutation angles is verified by comparing the simulation results of SRM1 for the FCS-MPTC with and without the proposed turn-off angle control. It Is observed that the average torque is increased by 39% at the base speed. Moreover, RMS current and torque ripple are reduced by 24% and 119.1% respectively. The experimental results of test SRM2 at both low-speed and high-speed operating points are also provided to validate the performance of the proposed control method.

Chapter 6

Second Online Adaptive Turn-Off Angle Control for FCS-MPTC of SRM Drives

In this chapter, the second online adaptive commutation angle control method for FCS-MPTC of SRM drives is proposed. The optimality condition, defined in the first online method, is modified in this chapter to achieve an improved performance. After presenting the method and the proposed optimality condition, the effectiveness of the proposed method in adaptively controlling the commutation angles at different speeds are shown using simulation results on the test SRM1. Finally, the experimental results of the test SRM2 with the proposed turn-off angle control scheme are presented.

6.1 Proposed second online method

To improve the performance of the first proposed online method, the second online commutation angle control method is proposed in this section for FCS-MPTC of

SRM drives. Similar to the first proposed online method, this method is based on predicting the freewheeling phase current and phase torque for an extended time interval much bigger than the prediction horizon of FCS-MPTC. Note that the prediction horizon of FCS-MPTC is kept as 1. As discussed earlier, the turn-off angle is around 180° in the conventional FCS-MPTC regardless of the speed, which is the main drawback of this method. Negative torque production leads to a lower average torque and higher rms current and consequently a lower efficiency. To prevent the negative torque production (zero negative torque), the phase has to be shut down early. In this case, a large amount of toque production capability of the phase is not used and the average shaft torque is again reduced. Hence, there is an optimal phase turn-off angle which helps to use the maximum torque production capability of the SRM while preventing excessive negative torque production. A method is proposed in this section based on the calculation of the work done by the excited phase after the phase is turned off.

Torque (T) is proportional to the radial force (F_r) exerted on the rotor surface ($T=R_rF_r$), where R_r is the rotor outer diameter. Under a constant speed, the rotor position (θ_r) has a linear variation with time ($\theta_r=kt$). Hence, the area under the torque-time curve is a representation of the work done by the excited phase ($\int F_r d\theta$) as

$$\int T dt = \int R_r F_r d(k'\theta) = R_r k' \int F_r d\theta. \quad (6.1)$$

The area under the torque-time (torque-position) curve can also be interpreted as the co-energy (W_c) by rearranging equation (2.6) as

$$W_c = \int T d\theta = R_r \int F_r d\theta. \tag{6.2}$$

In the proposed method, this work is calculated for the conducting phase after the turn-off angle. The area under the T-t curve is divided into two sections after the turn-off angle; between turn-off angle and the alignment position, and the other one between the alignment position and the point in which phase current reaches zero. It is obvious that the former area will be positive, however, the latter will be negative. The negative work (and the negative produced torque) which is done by the excited phase after the alignment position has to be compensated by another phase. If this negative area gets bigger, then a large extra torque will be needed to be developed by the upcoming phase. This requires higher phase current and again lower efficiency. In the proposed method, at the specific electrical angle in which the negative work (after the alignment position) becomes equal to the positive work (before the alignment position), the phase will be shut down. This is shown in Figure 6.1. Areas A_1 and A_2 are equal and the phase is shut down at θ_{off} which is shown on the figure. In the ideal case, area A_3 has to be equal to A_2 to compensate for the negative torque, and hence to deliver the reference torque on the shaft. However, the upcoming phase cannot compensate for all the negative torque especially at higher speeds, so, $|A_3| \leq |A_2| = |A_1|$.

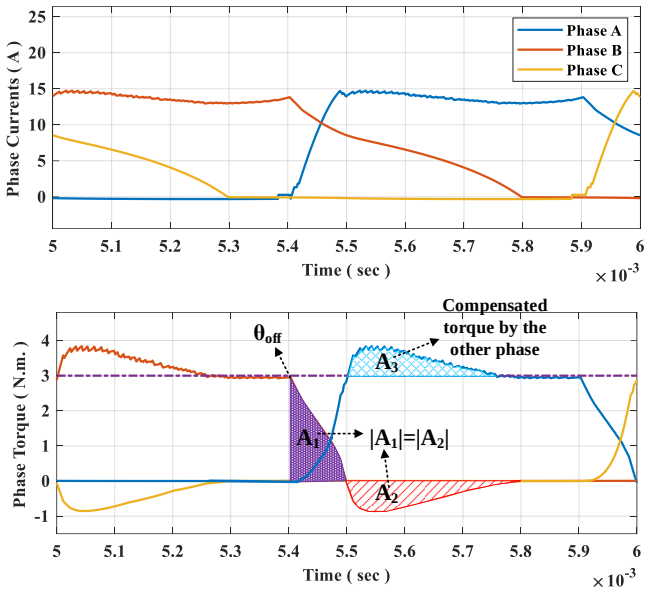

Figure 6.1: Representation of the optimality condition for the second proposed online turn-off angle control method

The turn-off angle usually lies in the interval of [90°, 180°]. In the proposed scheme, A_1 and A_2 are calculated from the predicted freewheeling phase current and predicted phase torque at each sampling interval. The phase voltage equation after the turn-off angle is given in equation (5.1). Similar to the previous chapter, the current at a future step j (i_j) can be predicted by solving this differential equation. The closed form solution for this differential equation is given in equation (5.2). At every sampling instant, the current i_j is predicted until its value becomes zero. The torque is also estimated using the torque-position-current LUT. The area under the torque curve is calculated using the midpoint integration rule. before the alignment position (θ_e=180°), torque is positive. The torque area becomes negative once the rotor passes the alignment position. This process is repeated at each sampling instant until the desired optimality condition (A_1=A_2) is met. The rotor

angle corresponding to the sampling instant meeting the condition (A_1=A_2) is the optimal turn-off angle. Therefore, the outgoing phase is turned-off at this sampling instant. Note that the flowchart of the second online method is very similar (except for the optimality condition) to the first proposed online method presented in Figure 5.2.

6.2 Simulation results

The proposed method is implemented in MATLAB/Simulink. The simulation results of the test SRM1 for n_{ref}=2000 rpm and T_{ref}=3 Nm are given in Figure 6.2. Similar to the previous simulations, the sample time and maximum switching frequency are set to 50 µs and 20 kHz respectively. It can be observed that the turn-ff angle is adjusted to be 169.8° (175.3° with FCS-MPC without turn-off angle control) using the proposed method. To track the desired reference torque, the turn-on angle is automatically adjusted to be 47.71° (48.1° with FCS-MPC without turn-off angle control). Comparing the results with the conventional FCS-MPTC reveals the effective reduction in phase negative torque and hence the rms current under similar operating conditions.

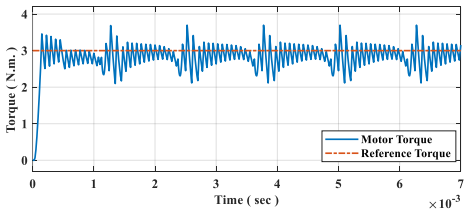

(a)

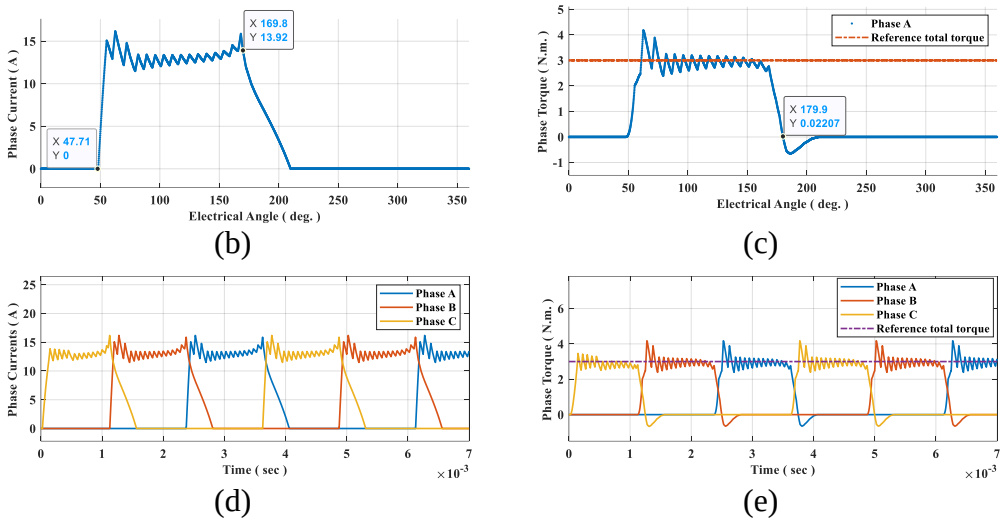

Figure 6.2: Simulation results of the test SRM1 with the second online method at n_{ref}=2000 rpm (low-speed) and T_{ref}=3 Nm; (a) torque, (b) phase current in one electrical cycle, (c) phase torque in one electrical cycle, (d) phase currents, and (e) phase torques.

To investigate the effectiveness of the proposed method at high-speed region, the same simulations are repeated for n_{ref}=6000 rpm (base-speed) and T_{ref}=1.5 Nm. The results are presented in Figure 6.3. The turn-off angle is effectively advanced to 165.3° (it is 177.4° with FCS-MPC without turn-off angle control) to prevent the negative torque production. The turn-on angle is also automatically reduced by FCS-MPTC (43.49°, it is 50.69° with FCS-MPTC without turn-off angle control) to deliver the desired average torque on the shaft. Significant improvement in terms of average torque and torque ripple can be observed by comparing the results with the conventional FCS-MPTC. A significant reduction in phase negative torque is achieved compared to the conventional FCS-MPTC by adjusting the commutation angles in the proposed method.

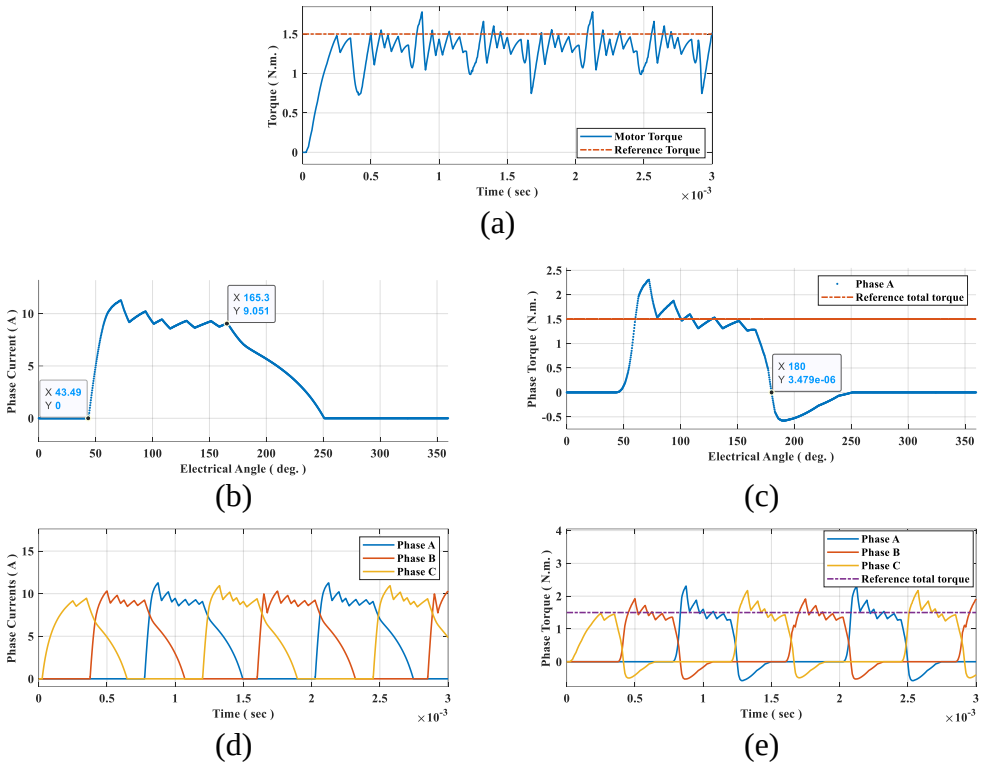

Figure 6.3: Simulation results of the test SRM1 with the second online method at n_{ref}=6000 rpm (high-speed) and T_{ref}=1.5 Nm; (a) torque, (b) phase current in one electrical cycle, (c) phase torque in one electrical cycle, (d) phase currents, and (e) phase torques.

6.3 Experimental results

The experimental test results of the test SRM2 with the proposed second online method at $n_{ref} = 2000\ rpm$ under the load torque of $T_{ref} = 3\ Nm$ are presented in Figure 6.4. The look up table of the optimal turn-off angles in the entire torque and speed ranges are calculated using the proposed method in simulations to be used for experimental implementation of the proposed control scheme. Similar to the previous experimental tests, the control frequency is set to 20 kHz. Due to the lower phase back-emf at 2000 rpm, the phase current can quickly reach to zero after

the turn-off angle (see Figure 6.4-b), and the phase negative torque is negligible as can be seen in both Figure 6.4-c and e. Hence, similar to the conventional FCS-MPTC, the optimal turn-off angle is adjusted to be close to the aligned position at lower speeds with the proposed method. By comparing Figure 6.4-b and d with Figure 4.9-b and d, it can be observed that the phase current peak is considerably reduced with the proposed turn-off angle control strategy compared to the conventional FCS-MPTC.

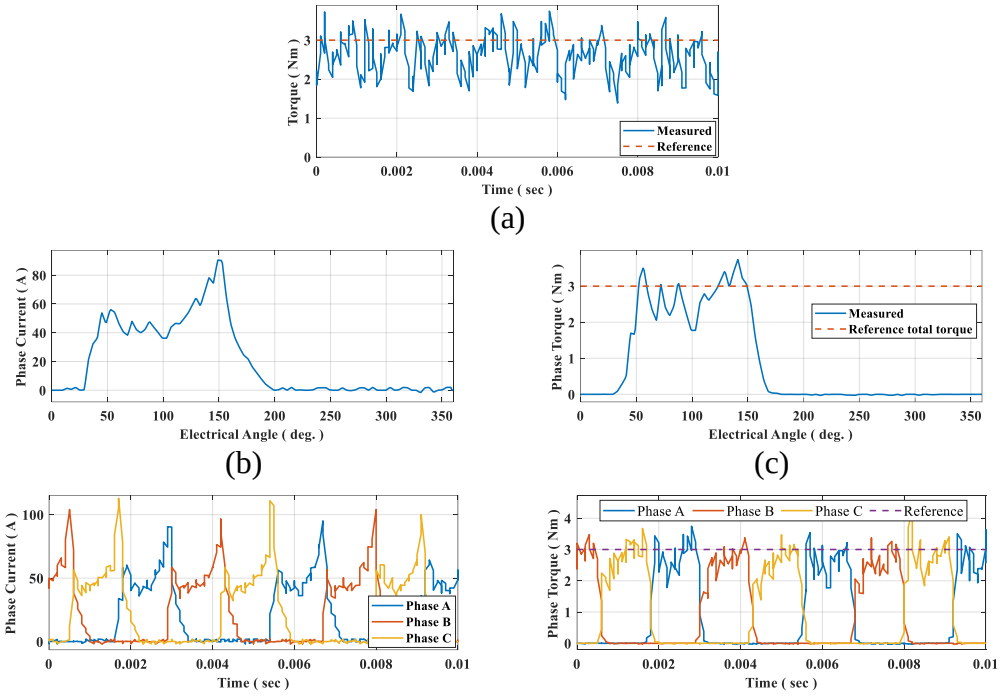

Figure 6.4: Experimental test results of SRM2 with the second online method (20 kHz) at n_{ref}=2000 rpm (low-speed) and T_{ref}=3 Nm; (a) torque, (b) phase current in one electrical cycle, (c) phase torque in one electrical cycle, (d) phase currents, and (e) phase torques.

To investigate the performance of the proposed control method at higher speeds, the experimental results of SRM2 are presented at $n_{ref} = 4000\ rpm$ under the load

torque of $T_{ref} = 3\ Nm$ in Figure 6.5. According to Figure 6.5-a and Figure 4.10-a, it can be observed that higher average torque can be achieved with the proposed method compared to the conventional FCS-MPTC. By comparing the measured phase currents in Figure 6.5-b and Figure 4.10-b, it can be understood that the commutation angles are advanced with the proposed method to reduce the negative phase torque. The current tail in the generating region is shorter compared to the conventional FCS-MPTC resulting in a lower phase negative torque as can be seen in both Figure 6.5-c and Figure 6.5-e. This reduction in the phase negative torque leads to the reduction in the rms phase current as can be understood by comparing Figure 6.5-b and d with Figure 4.10-b and d, respectively. Moreover, it can be also observed that the phase current peak is significantly lower with the proposed method compared to the conventional FCS-MPTC. Comparing the experimental results of the second online method (Figure 6.5) with the first online method (Figure 5.7) reveals that the commutation angles are less advanced with the second online method, resulting in a slightly larger phase negative torque with this method. On the other hand, the torque production capability of SRM close to the aligned position is better utilized with the second online method.

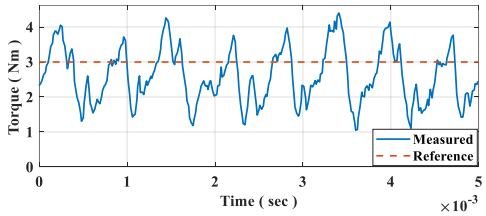

(a)

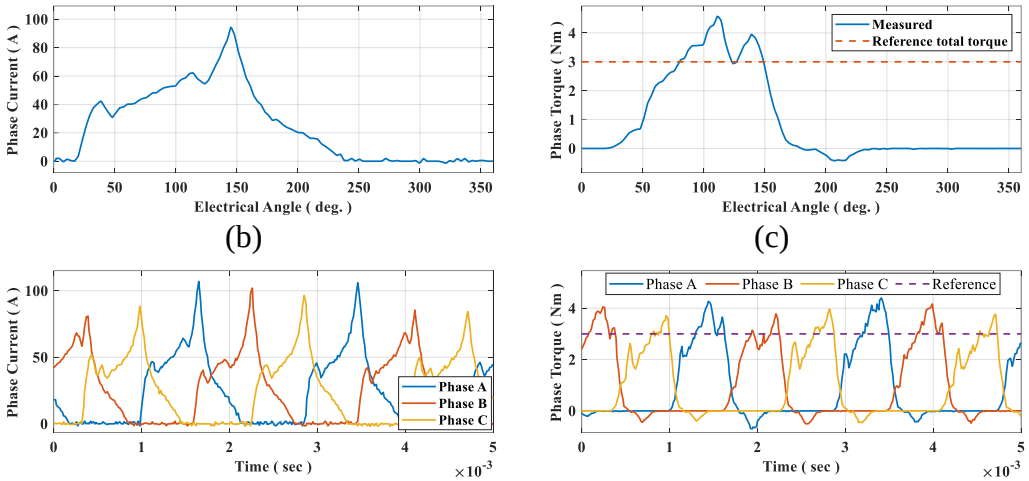

Figure 6.5: Experimental test results of SRM2 with the second online method (20 kHz) at n_{ref}=4000 rpm and T_{ref}=3 Nm; (a) torque, (b) phase current in one electrical cycle, (c) phase torque in one electrical cycle, (d) phase currents, and (e) phase torques.

6.4 Summary

In order to improve the performance of the first online method, presented in Chapter 5, the second online adaptive commutation angle control method with modified optimality condition is proposed in this chapter. The optimality condition is based on the balance between the positive work and the negative work done by the conducting phase after the turn-off angle. The simulation results of the test SRM1 reveal the superior performance of the proposed method compared to the conventional FCS-MPTC at base-speed in terms of torque ripple, average torque, and phase negative torque. Comparing the experimental results of the test SRM2 with the conventional FCS-MPTC shows that a smaller negative torque can be achieved by the proposed method by advancing the commutation angles at higher

speeds. The proposed second online method has a less advanced turn-off angle, and hence, a larger phase negative torque compared to the first proposed online method especially at higher speeds. However, it has a better utilization of the torque production capability of SRM close to the aligned position compared to the first proposed online method. An offline multi-objective optimization-based method is proposed in the next chapter to find the globally optimal turn-off angle and k_{MPC} for FCS-MPTC of SRM drives in the entire torque and speed ranges.

Chapter 7

Multi-Objective Optimization-Based Offline Commutation Angle Control

In this chapter, an offline multi-objective optimization problem, with both average torque tracking error and rms current minimization as optimization objectives, is defined and solved to determine the globally optimal phase turn-off angle in FCS-MPTC for SRM drives. The weighting factor in the objective function of FCS-MPTC (k_{MPC}) is considered as the second optimization variable. A parametric sweep is carried out to analyze the effect of changing the optimization variables on the performance of the test SRM1. After presenting the optimization results and the pareto-front analysis for both SRM1 and SRM2, the optimal solution to the multi-objective optimization problem is selected. The performance of the proposed optimization-based offline method is then validated by presenting the simulation results of the test SRM1 for the selected optimal points. Finally, the experimental test results of the test SRM2 for the selected optimal points, found based on multi-

objective optimization, are presented to experimentally validate the performance of the proposed commutation angle control scheme.

7.1 Multi-objective optimization problem

The optimal turn-off angle is determined in both proposed online methods based on a defined optimality condition, however, it is not proven whether the obtained turn-off angle is the globally optimal commutation angle or not. Besides, the weighting factor (k_{MPC}) of the objective function of FCS-MPTC is kept constant in all the simulations and experimental results for online methods. Note that changing the weighting factor will affect the performance of the controller.

7.1.1 Objective function of optimization problem

A multi-objective optimization problem is formulated and solved in this chapter to find the globally optimal turn-off angle and k_{MPC} in the entire torque and speed ranges to achieve the desired performance. Delivering the average torque on the shaft while minimizing the rms phase current are considered as two objectives of the optimization as

$$\begin{cases} f_1 = \dfrac{(T_{avg} - T_{ref})^2}{T_{rated}^2} \\ f_2 = \dfrac{I_{rms}^2}{I_{max}^2} \end{cases} \tag{7.1}$$

where T_{rated} and I_{max}, which are used for normalization of the objective functions, are rated torque and maximum current amplitude limit of the test SRM respectively.

7.1.2 **Selection of optimization variables**

The variables of the optimization are the phase turn-off angle (θ_{off}) and the weighting factor (k_{MPC}) used in the objective function of FCS-MPTC. The optimum k_{MPC} is selected to make a trade off between minimized rms current (also more smooth current) and torque tracking with minimum steady state error. The simulation results of SRM1 for k_{MPC}=0.2 and k_{MPC}=20 (n_{ref}=2000 rpm, T_{ref}=3 Nm) under maximum switching frequency of 20 kHz using the proposed first online adaptive angle control are given in Figure 7.1 and Figure 7.2 respectively.

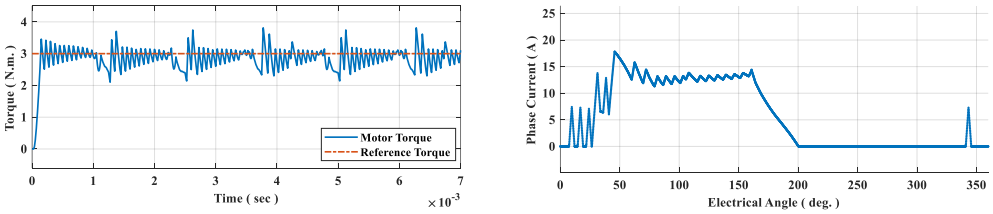

(a) (b)

Figure 7.1: Simulation results of the test SRM1 with the proposed first online method with k_{MPC}=0.2 at n_{ref}=2000 rpm and T_{ref}=3 Nm; (a) torque, and (b) phase current in one electrical cycle.

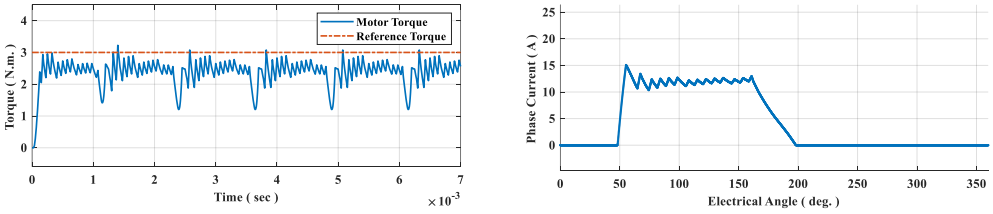

(a) (b)

Figure 7.2: Simulation results of the test SRM1 with the proposed first online method with k_{MPC}=20 at n_{ref}=2000 rpm and T_{ref}=3 Nm; (a) torque, and (b) phase current in one electrical cycle.

It can be observed from Figure 7.1 that a lower k_{MPC} results in extra undesirable switching which increases both switching and copper losses. On the other hand, a

higher k_{MPC} leads to a smoother current as can be seen in Figure 7.2-b, however, there is a steady state torque error (see Figure 7.2-a) as the importance of the average torque tracking term has been reduced compared to the rms current minimization term by increasing k_{MPC}.

7.1.3 **Parametric sweep by varying optimization variables**

To observe the effect of variations in θ_{off} and k_{MPC} on performance of SRM1, a parametric sweep is carried out by varying $90° \leq \theta_{off} \leq 180°$ and $0 \leq k_{MPC} \leq 50$. The simulation results at n_{ref}=2000 rpm and T_{ref}=3 Nm are presented in Figure 7.3. It can be observed from Figure 7.3-a that maximum torque is achieved when k_{MPC} is close to zero and θ_{off} is near 180°. However, rms current is higher when θ_{off} is very close to 180° (see Figure 7.3-b) as the current extends to inductance falling region leading to negative torque production. Moreover, it is observed from Figure 7.3-c that thermal limit of the SRM due to peak current constraint (I_{max}=21 A) has an important effect in determining the optimal feasible operating point. Torque ripple is also reduced by selecting k_{MPC} close to zero and θ_{off} close to 180°. However, it is high when θ_{off} is in [175°,180°] interval due to negative torque as can be seen in both Figure 7.3-d and Figure 7.3-e. As the desired reference torque is achieved when θ_{off} is very close to the aligned position (180°), it can be concluded that, at lower speed region, the turn-off angle with the conventional FCS-MPTC without turn-off angle control is close to the globally optimal turn-off angle point.

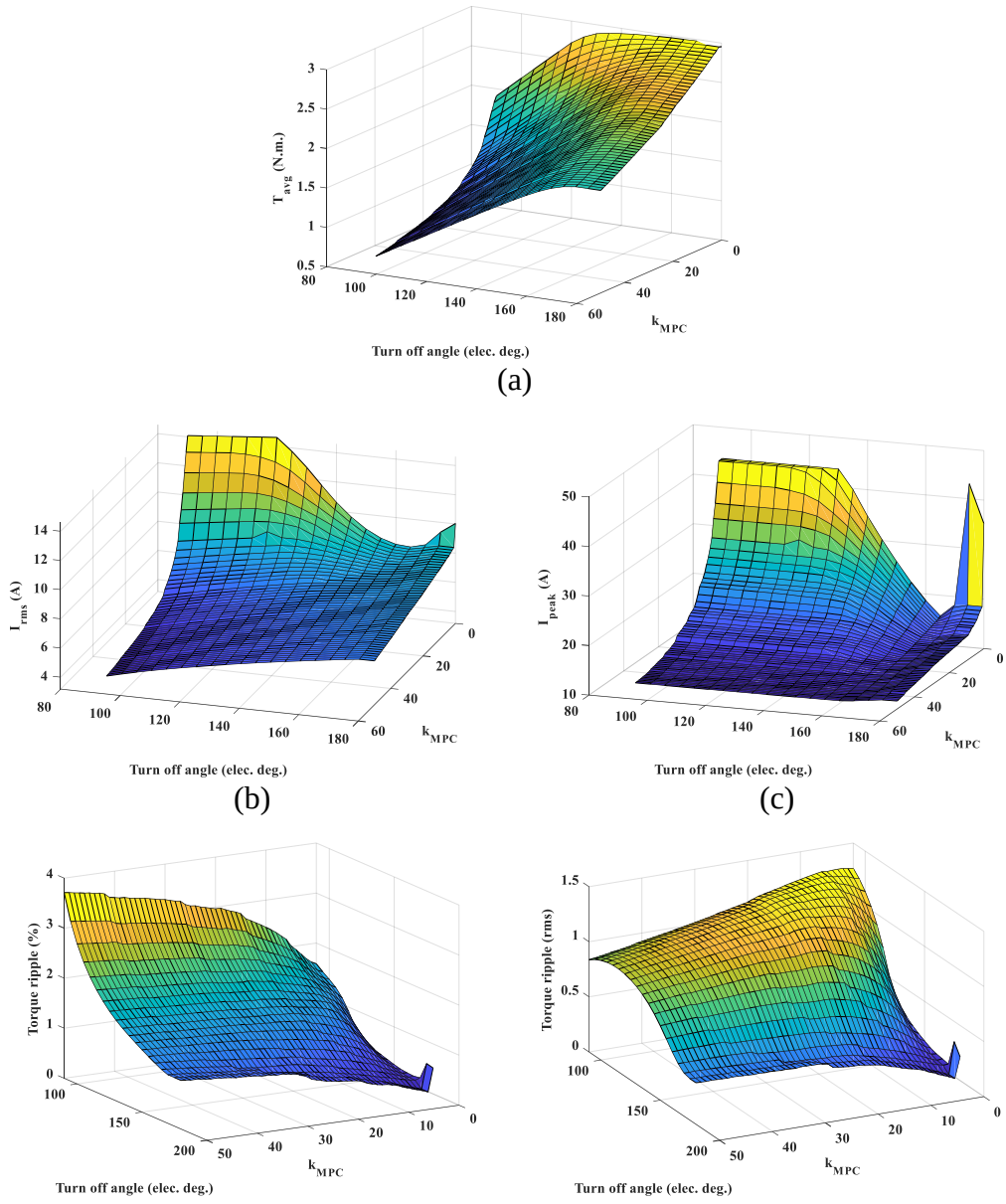

Figure 7.3: Performance calculation results of the test SRM1 with a parametric sweep over θ_{off} and k_{MPC} at n_{ref}=2000 rpm (low-speed) and T_{ref}=3 Nm; (a) average torque, (b) rms current, (c) peak current, (d) torque ripple (%), and (e) torque ripple (rms).

The same parametric sweep is carried out for SRM1 by varying $90° \leq \theta_{off} \leq 180°$ and $0 \leq k_{MPC} \leq 30$ at n_{ref}=6000 rpm and T_{ref}=1.5 Nm. The results are given in Figure 7.4.

Due to higher back-emf at 6000 rpm, the phase current needs more time to decay, so the maximum average torque is achieved around θ_{off}=165° and k_{MPC}=0 as seen in Figure 7.4-a. The average torque decreases by increasing k_{MPC}. On the other hand, the rms current increases by reducing the weighting factor for current minimization term (k_{MPC}) based on Figure 7.4-b. When k_{MPC}=0 the rms current has a minimum around θ_{off}=155°. As the SRM1 has lower torque production capability close to unaligned position, the peak phase current is high when turn-off angle is excessively advanced as can be observed from Figure 7.4-c. Torque ripple also increases by selecting θ_{off} very close to the aligned position (180°) based on both Figure 7.4-d and Figure 7.4-e because of the high-speed operation, the higher back-emf, the longer required time for current decay and consequently the larger negative torque.

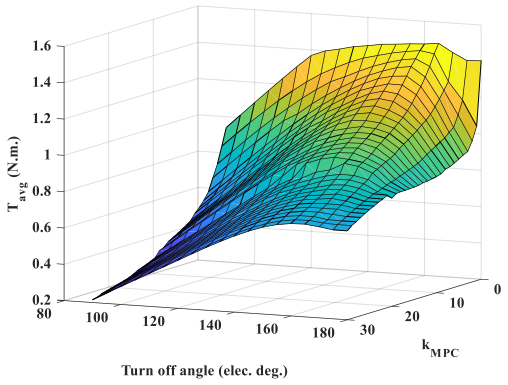

(a)

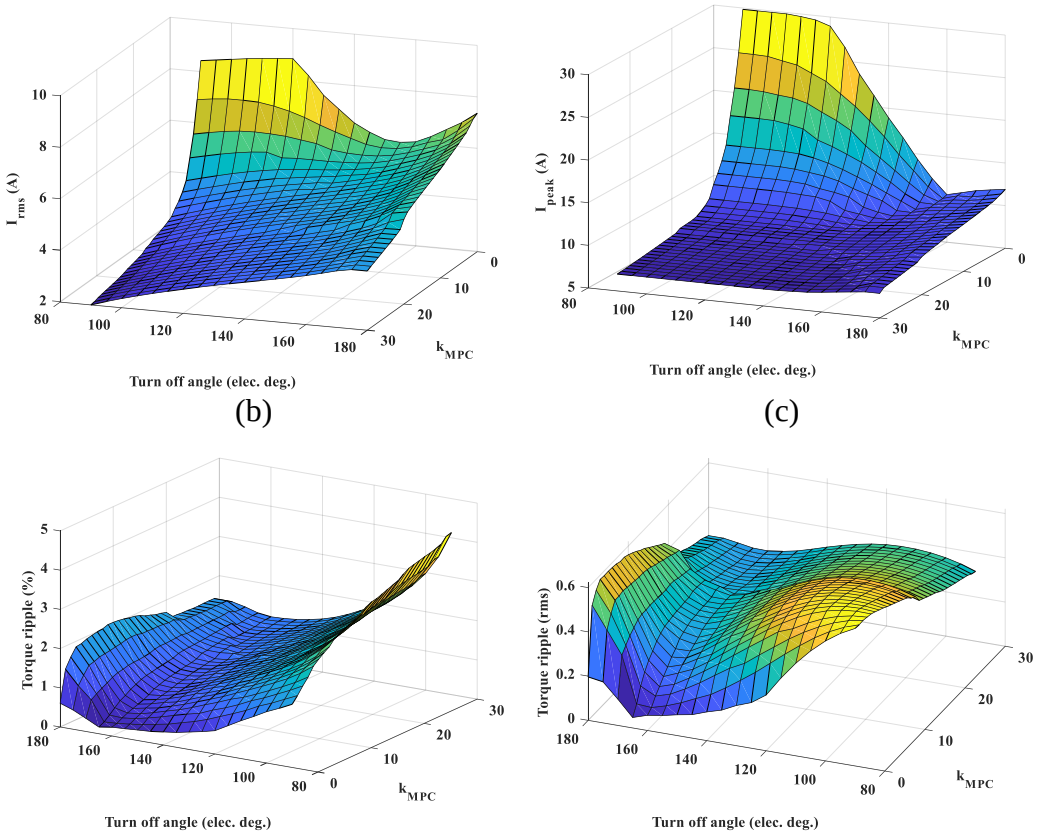

Figure 7.4: Performance calculation results of the test SRM1 with a parametric sweep over θ_{off} and k_{MPC} at n_{ref}=6000 rpm (high-speed) and T_{ref}=1.5 Nm; (a) average torque, (b) rms current, (c) peak current, (d) torque ripple (%), and (e) torque ripple (rms).

Note that rms torque ripple (ΔT_{rms}) is a measure of the output torque quality. It represents how far the instantaneous torque is from the average torque [7]. ΔT_{rms} is calculated using

$$\Delta T_{rms} = \sqrt{\frac{1}{\theta_2 - \theta_1}\int_{\theta_1}^{\theta_2}\left(T(\theta) - T_{avg}\right)^2 d\theta} \tag{7.2}$$

where $T(\theta)$ is the torque waveform as a function of rotor position. $(\theta_2-\theta_1)$ is equal to one full electrical cycle. T_{avg} is the average torque over one electrical cycle as

$$T_{avg} = \frac{1}{\theta_2-\theta_1}\int_{\theta_1}^{\theta_2} T(\theta)d\theta. \tag{7.3}$$

Torque ripple is usually defined as the function of $(T_{max}-T_{min})$ over T_{avg} in the literature as

$$\Delta T_{percent} = 100 \times \frac{T_{max} - T_{min}}{T_{avg}} \tag{7.4}$$

where T_{min} and T_{max} stand for the minimum and maximum of the instantaneous total torque, respectively. In this thesis, both ΔT_{rms} and $\Delta T_{percent}$ are calculated and compared for different control methods. Finally, rms current is calculated using

$$I_{rms} = \sqrt{\frac{1}{\theta_2-\theta_1}\int_{\theta_1}^{\theta_2} \left(i_{phase}(\theta)\right)^2 d\theta}. \tag{7.5}$$

7.2 Optimization results for SRM1

A constrained multi-objective genetic algorithm optimization is carried out for SRM1 considering both peak current ($I_{max}\leq 21$ A) and rms current ($I_{rms}\leq 14.15$ A) limits. A comprehensive guide on genetic algorithm optimization can be found in [85]. Required simulations in the optimization process are done under maximum switching frequency of 500 kHz to eliminate the effect of sampling. Optimum $90°\leq\theta_{off}\leq 180°$ and $0\leq k_{MPC}\leq 200$ are determined for different reference torque and reference speed levels covering all operating regions of SRM1. The objective function for multi-objective optimization is formulated as

$$f_{GA} = wf_1 + (1-w)f_2 = w\left(\frac{(T_{avg} - T_{ref})^2}{T_{rated}^2}\right) + (1-w)\left(\frac{I_{rms}^2}{I_{max}^2}\right) \qquad (7.6)$$

where w is the weighting factor varying in the interval of [0,1] to change the importance of average torque tracking term compared to rms current minimization term. Number of populations, number of stall generations, objective function tolerance and number of elite count are set to 300, 12, 0.05 and 5 respectively.

In the optimization process for each reference torque and reference speed point, GA runs Simulink to calculate performance of SRM for all the individual populations (θ_{off}, k_{MPC}) of the corresponding generation. 5 populations with lower fitness function (f_{GA}) values are survived to the next generation. Other populations in the next generation are constructed using mutation and cross over functions of GA. This process is repeated until the desired stopping criteria is met.

The optimization results for SRM1 at 2000 rpm for different reference torque levels are given in Figure 7.5.

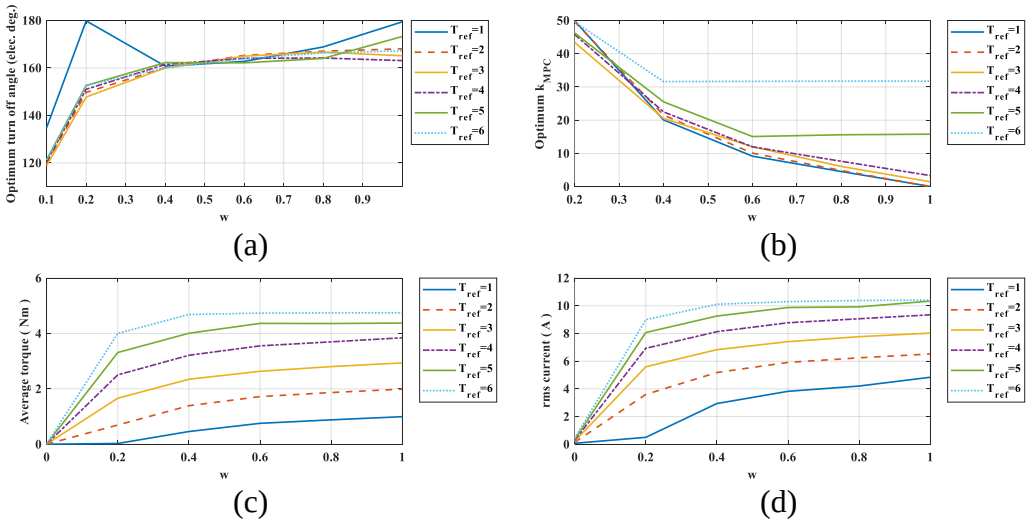

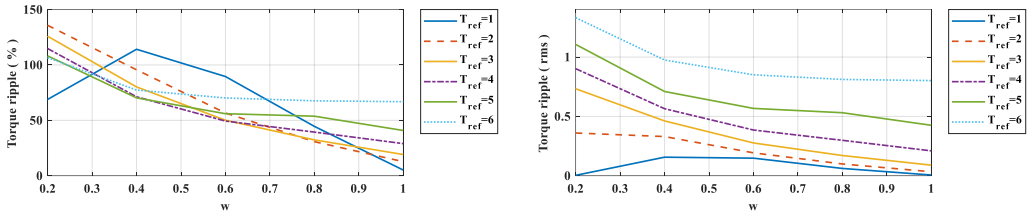

(e) (f)

Figure 7.5: Multi-objective genetic algorithm (GA) optimization results for SRM1 at n_{ref}=2000 rpm (low-speed); (a) optimum turn-off angle, (b) optimum $k_{MPC,}$ (c) average torque, (d) rms current, (e) torque ripple (%), and (f) torque ripple (rms).

The optimization results for SRM1 at 6000 rpm are presented in Figure 7.6.

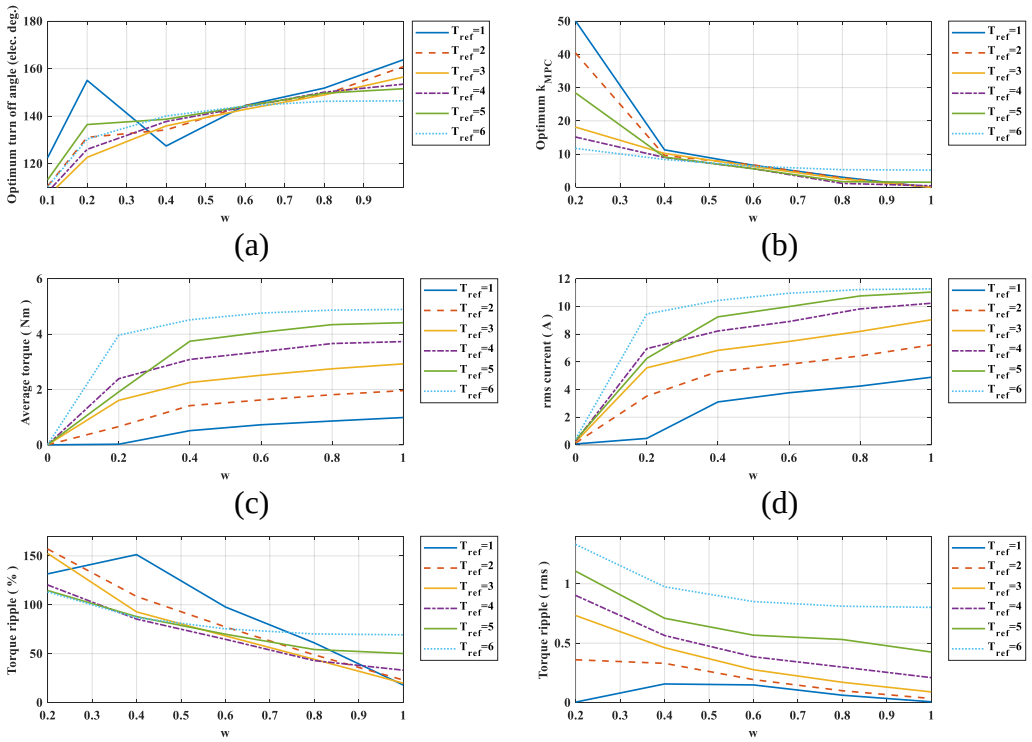

(a) (b)

(c) (d)

(e) (f)

Figure 7.6: Multi-objective GA optimization results for SRM1 at n_{ref}=6000 rpm (high-speed); (a) optimum turn-off angle, (b) optimum $k_{MPC,}$ (c) average torque, (d) rms current, (e) torque ripple (%), and (f) torque ripple (rms).

Turn-off angle increases by increasing *w* based on Figure 7.5-a and Figure 7.6-a to utilize maximum torque production capability of SRM. On the other hand, k_{MPC} is

reduced to decrease the effect of the instantaneous current minimization term in the objective function of FCS-MPTC (Figure 7.5-b and Figure 7.6-b). It can be observed from both Figure 7.5-c and Figure 7.6-c that good average torque tracking is achieved when $w = 1$. However, rms current is also maximized with this weighting factor as seen in Figure 7.5-d and Figure 7.6-d. By increasing w the importance of average torque tracking term increases and hence a better torque quality is achieved. So, torque ripple is reduced as w changes from 0 to 1 based on Figure 7.5-e,f and Figure 7.6-e,f. Because delivering the desired torque on the shaft is considered as the first priority, w is preferred to be as close as possible to 1. Based on Figure 7.1, it can be seen that a very low k_{MPC} leads to excessive undesirable switching which has to be avoided. The optimum w is selected to be 0.8 by making a compromise between maximizing average torque tracking and the smoothness of the current.

7.2.1 Pareto-front analysis of multi-objective optimization for SRM1

In order to choose an optimal weighting factor for GA optimization in the entire operating range of SRM, the pareto front of the multi-objective optimization is presented in this section for different operating regions of SRM1. Note that the rated torque of the test SRM1 is 3.8 Nm.

1) High torque at base speed (3Nm at 6000 rpm)

The pareto front of the multi-objective optimization at 6000 rpm under 3 Nm is presented in Figure 7.7.

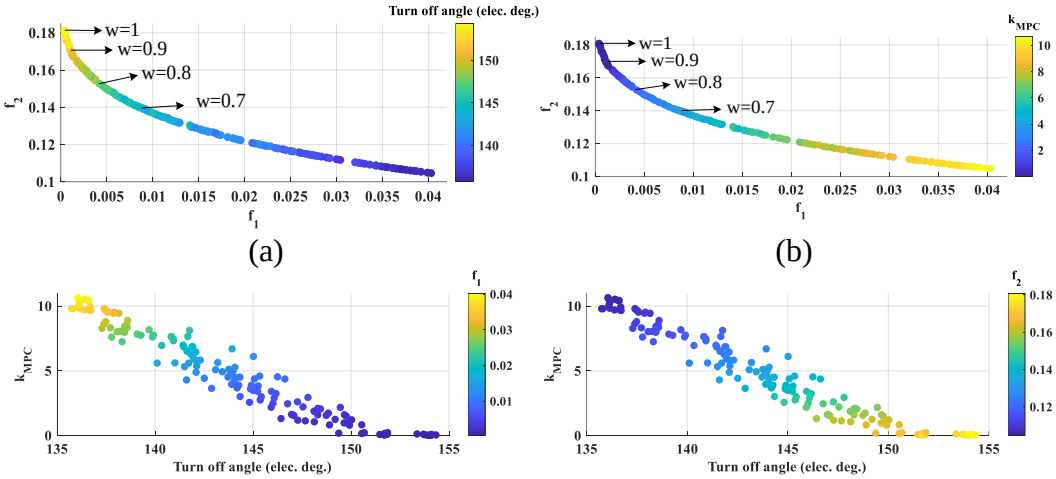

Figure 7.7: Pareto front of multi-objective optimization for SRM1 at 6000 rpm under 3 Nm; (a) variation of optimal turn off angle on pareto front, (b) variation of optimal k_{MPC} on pareto front, (c) variation of f_1 with optimization variables, and (d) variation of f_2 with optimization variables.

2) High torque at low speed (3 Nm at 2000 rpm)

The results at 2000 rpm under load torque of 3 Nm are presented in Figure 7.8.

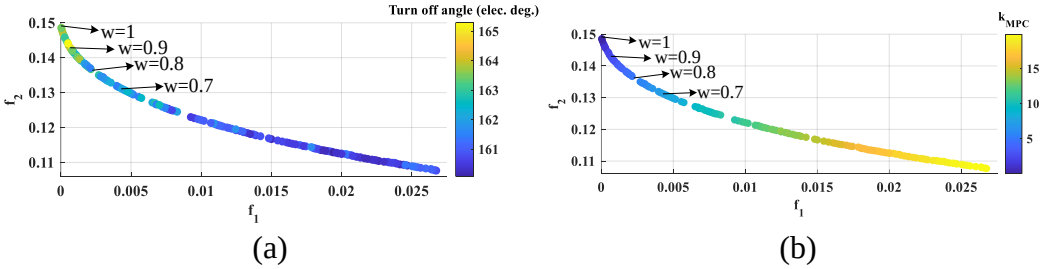

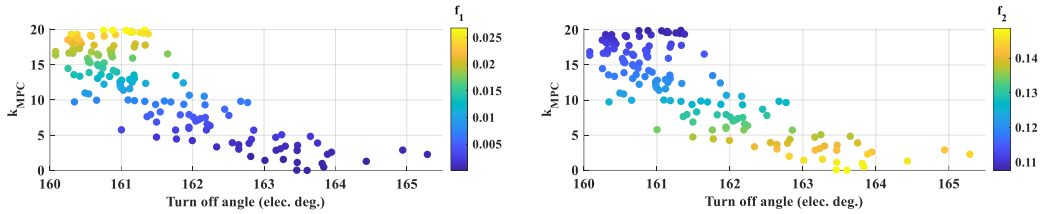

(c) (c)

Figure 7.8: Pareto front of multi-objective optimization for SRM1 at 2000 rpm under 3 Nm; (a) variation of optimal turn off angle on pareto front, (b) variation of optimal k_{MPC} on pareto front, (c) variation of f_1 with optimization variables, and (d) variation of f_2 with optimization variables.

3) Low torque at base speed (1Nm at 6000 rpm)

The pareto front of the multi-objective optimization at 6000 rpm under 1 Nm is presented in Figure 7.9.

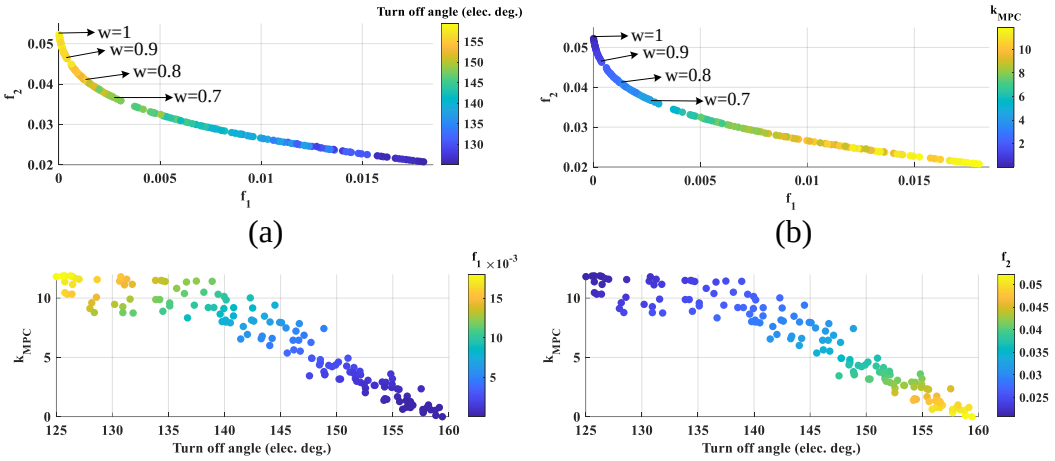

(a) (b)

(c) (d)

Figure 7.9: Pareto front of multi-objective optimization for SRM1 at 6000 rpm under 1 Nm; (a) variation of optimal turn off angle on pareto front, (b) variation of optimal k_{MPC} on pareto front, (c) variation of f_1 with optimization variables, and (d) variation of f_2 with optimization variables.

4) Low torque at low speed (1 Nm at 2000 rpm)

Finally, the pareto front of optimization at 2000 rpm under load torque of 1 Nm is given in Figure 7.10.

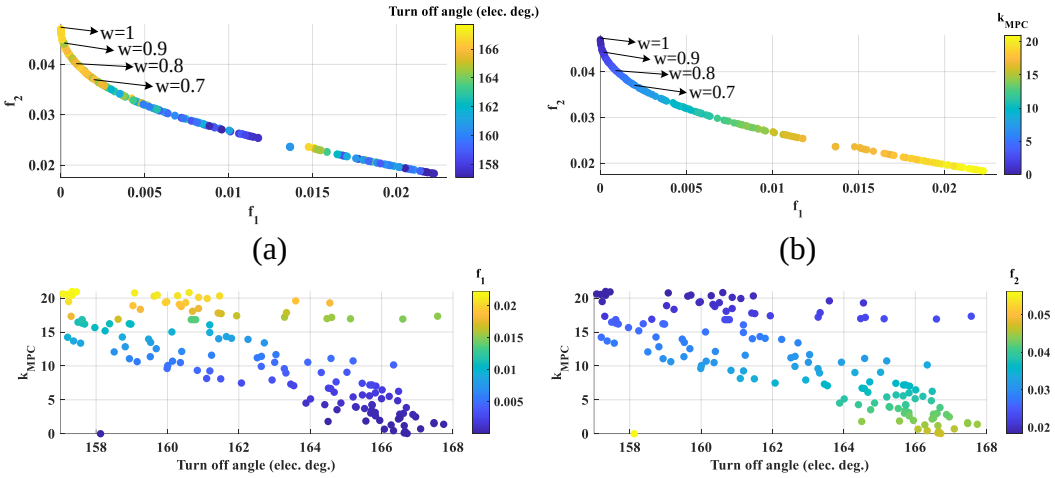

Figure 7.10: Pareto front of multi-objective optimization for SRM1 at 2000 rpm under 1 Nm; (a) variation of optimal turn off angle on pareto front, (b) variation of optimal k_{MPC} on pareto front, (c) variation of f_1 with optimization variables, and (d) variation of f_2 with optimization variables.

According to Figure 7.7-Figure 7.10, some gaps are observed on the pareto fronts of the optimizations. In this thesis, the gaps on the pareto fronts have been reduced by increasing the number of populations of the multi-objective optimization. However, searching for gaps algorithms [86] can also be implemented to further minimize the gaps on the pareto fronts of the optimizations. Note that in the optimization problem the torque tracking is considered as the primary objective with rms current minimization as a side objective. Therefore, the purpose is to achieve a minimized f_1 to have a torque tracking with minimized steady state error. Based on the pareto front results provided for different operating points in the entire operating region of SRM1 up to the base speed, it can be observed that as w increases the torque tracking error is minimized, but the rms current increases. It can be also observed that as w increases the optimal turn-off angle is pushed

towards 180° electrical to use the maximum torque production capability of SRM. On the other hand, optimal k_{MPC} reduces which results in a higher rms current and hence lower efficiency. According to the pareto fronts in the entire operating region, as stated in the previous section, the weighting factor corresponding to the optimal solution of the multi-objective optimization problem for SRM1 is selected to be $w = 0.8$ in this thesis. The optimal solution corresponding to $w = 0.8$ is shown on the pareto fronts provided in the entire torque-speed range (Figure 7.7-Figure 7.10).

7.2.2 Contour plots of optimal solution for SRM1

The contour plots of the optimal solution of the genetic algorithm optimization with $w = 0.8$ are presented in Figure 7.11 for the entire operating torque and speed ranges of SRM1. Note that x and y axes of the graphs stand for reference speed and average delivered torque respectively except for Figure 7.11-a in which y-axis stands for the reference torque.

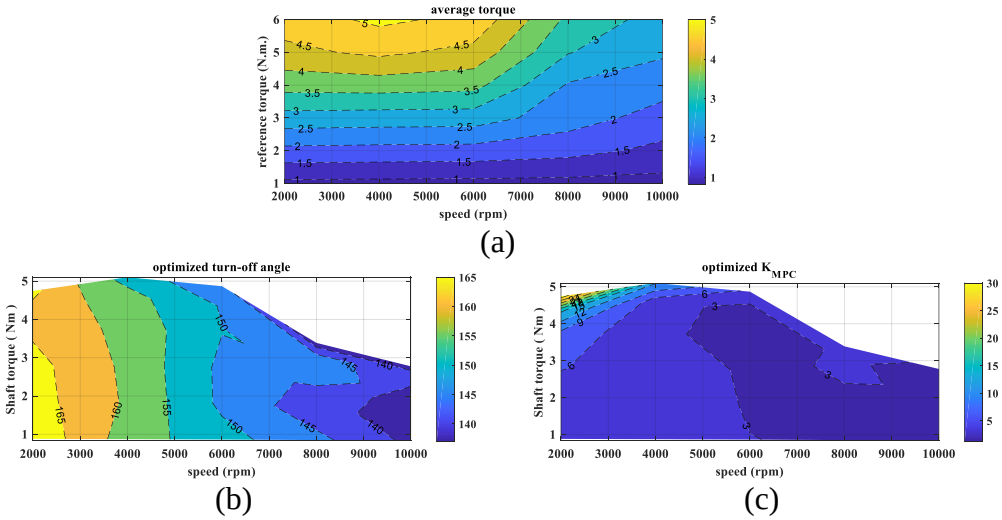

(a)

(b)

(c)

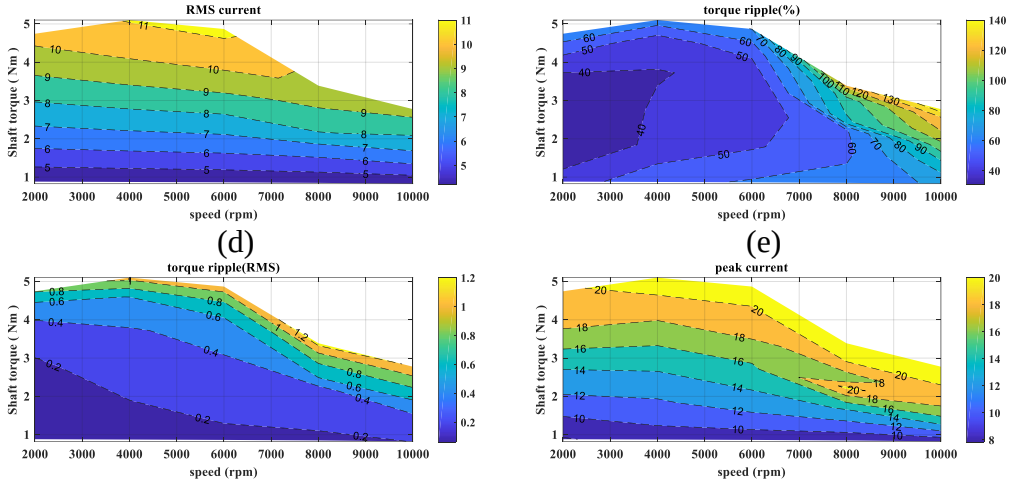

Figure 7.11: GA Optimization results for SRM1 with $w = 0.8$; (a) average torque, (b) optimum turn-off angle, (c) optimum k_{MPC}, (d) rms current, (e) torque ripple (%), (f) torque ripple (rms), and (g) peak current.

It can be observed from Figure 7.11-a that the reference average torque cannot be perfectly tracked especially at higher speeds. It means that there is a steady state torque tracking error which increases by the speed. This is because FCS-MPTC selects and applies the optimum switching state taking only one immediate future step into consideration. As a result, FCS-MPTC does not have any information on torque history and only instantaneous torque is considered. Moreover, based on the construction of its objective function, FCS-MPTC aims to maximize torque extraction while minimizing the rms current for a given reference torque. Hence, the instantaneous torque is always equal (in the best-case scenario) or less than the reference torque resulting in steady state torque error. Based on Figure 7.11-b, it can be understood that optimal turn-off angle is mostly dependent on speed. In other words, for constant speed, the optimal turn-off angle is almost constant as the

reference torque increases. However, optimal k_{MPC} is dependent on both speed and torque based on Figure 7.11-c. Both turn off angle and k_{MPC} are reduced as the speed increases. Higher rms current is required as the torque increases as seen in Figure 7.11-d. It can be understood from both Figure 7.11-e and Figure 7.11-f that torque ripple increases as the motor moves into higher speed and higher torque regions. Finally, it can be observed from Figure 7.11-g that the maximum current amplitude (I_{max}=21 A) is the main limiting factor determining the maximum torque production capability of the SRM over the operating speed range.

7.3 Simulation results for 12/8 2.3 kW SRM (SRM1)

The simulation results of the test SRM1 with the proposed offline multi-objective optimization-based commutation angle control method at n_{ref}=2000 rpm and T_{ref}=3 Nm are given in Figure 7.12. The optimal turn-off angle and k_{MPC} at this operating point are 166.68° and 6.09 based on optimization results given in Figure 7.11. Similar to all previous simulations, maximum switching frequency is set to 20 kHz.

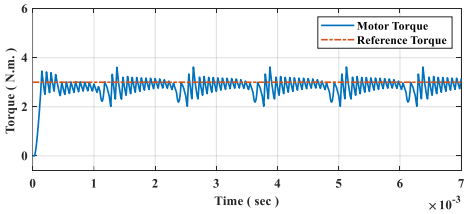

(a)

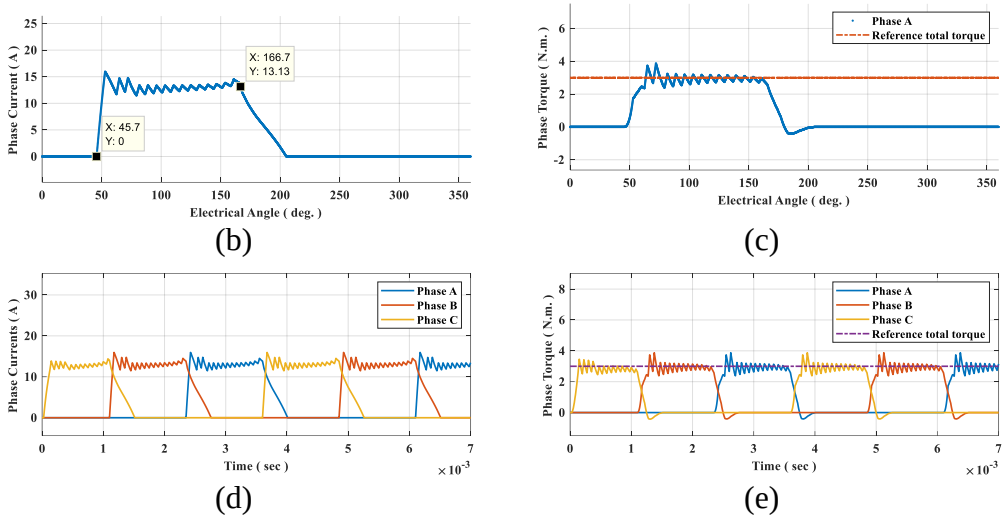

Figure 7.12: Simulation results of the test SRM1 with the proposed offline optimization-based method at n_{ref}=2000 rpm (low-speed) and T_{ref}=3 Nm; (a) torque, (b) phase current in one electrical cycle, (c) phase torque in one electrical cycle, (d) phase currents, and (e) phase torques.

It can be seen from Figure 7.12-b that by adjusting the turn-off angle to 166.68° the turn-on angle is advanced by FCS-MPTC to 45.7° compared to FCS-MPTC without commutation angle control (48.1°) to deliver the desired torque on the shaft. The negative torque is considerably reduced as seen in Figure 7.12-c compared to the existing FCS-MPTC resulting in lower rms current and better utilization of torque production capability of the machine. The simulation results of the test SRM1 at n_{ref}=6000 rpm and T_{ref}=1.5 Nm are presented in Figure 7.13. Optimal turn-off angle and weighting factor for FCS-MPTC are found to be θ_{off}=150.39° and k_{MPC}=2.93 based on the optimization results.

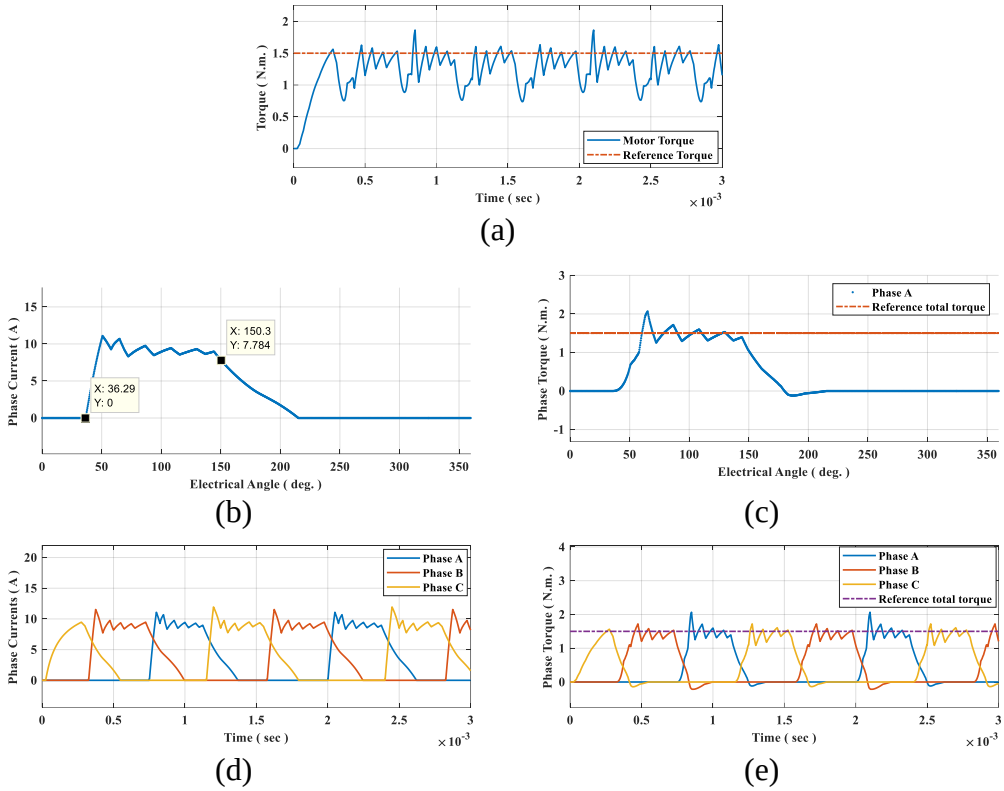

Figure 7.13: Simulation results of the test SRM1 with the proposed offline optimization-based method at n_{ref}=6000 rpm (base-speed) and T_{ref}=1.5 Nm; (a) torque, (b) phase current in one electrical cycle, (c) phase torque in one electrical cycle, (d) phase currents, and (e) phase torques.

It can be seen from Figure 7.13-a that torque ripple and torque quality are significantly improved compared to the existing FCS-MPTC without commutation angle control. The phase turn-on angle is advanced by FCS-MPTC to 36.29° as seen in Figure 7.13-b (it is 50.69° with the existing FCS-MPTC) to deliver the desired average torque on the shaft. It can be observed from Figure 7.13-c that negative torque is effectively reduced in high-speed region compared to FCS-MPTC without turn-off angle control. Hence, there is a considerable improvement

in SRM performance at 6000 rpm (base-speed) compared to the conventional FCS-MPTC without tun-off angle control.

7.4 Optimization results for SRM2

A similar constrained multi-objective optimization problem is formulated and solved for SRM2 to determine the optimal turn-off angle and k_{MPC} (optimization variables) on the pareto front of the optimization at both low speed (1000 rpm) and base speed (5000 rpm) operating points. Similar to the previous case, functions f_1 and f_2, given in equation (7.1), are used to construct the objective function for the multi-objective optimization problem (f_{GA}), presented in equation (7.6). The weighting factor (w) dictates the importance of the average torque tracking term with respect to rms current minimization term. The configurations of the multi-objective optimization are set similar to the previous case.

7.4.1 Pareto front analysis of multi-objective optimization for SRM2

The pareto front of the multi-objective optimization at low speed (1000 rpm) under reference torque of 3 Nm is presented in Figure 7.14. The variation of the optimal turn-off angle and k_{MPC} are shown on the pareto front in Figure 7.14-a and b, respectively. It can be observed that as w increases, the optimal turn-off angle is increased to maximize the average output torque. On the other hand, the optimal

k_{MPC} is reduced resulting in a higher rms current. The optimal solutions corresponding to $w = 0.4, 0.7, 0.8, 0.9$ and 1 are also marked on the pareto fronts. The trajectory of the optimal solutions along with the variation of f_1 and f_2 are presented in Figure 7.14-c and d, respectively.

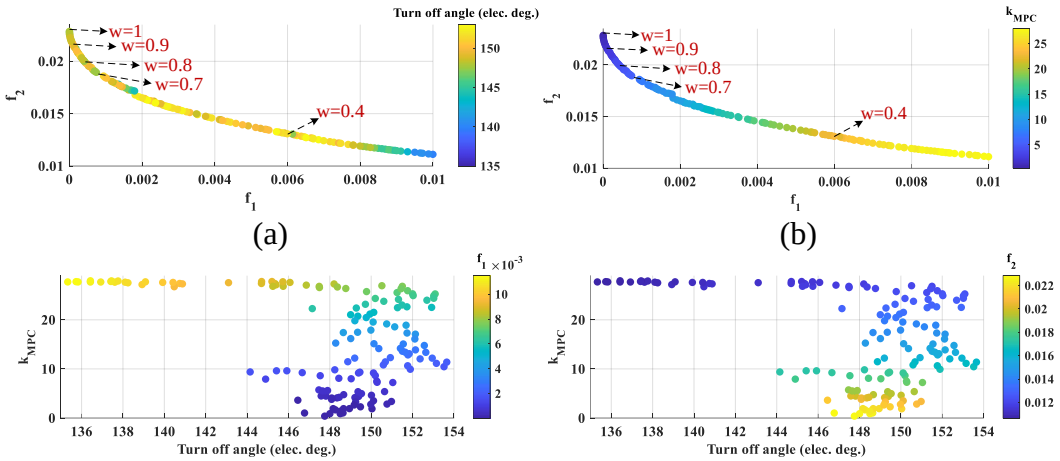

Figure 7.14: Pareto front of multi-objective optimization for SRM2 at 1000 rpm under 3 Nm; (a) variation of optimal turn off angle on pareto front, (b) variation of optimal k_{MPC} on pareto front, (c) variation of f_1 with optimization variables, and (d) variation of f_2 with optimization variables.

The optimization results at the base speed (5000 rpm) under reference torque of 3 Nm are presented in Figure 7.15. The variation of the optimal turn-off angle and optimal k_{MPC} are shown on the pareto fronts in Figure 7.15-a and b, respectively. Similar to the low-speed operation, as w increases, the optimal turn-off angle is increased and the optimal k_{MPC} is reduced. The variation of f_1 and f_2 are shown on the trajectory of the optimal solutions given in Figure 7.15-c and d, respectively.

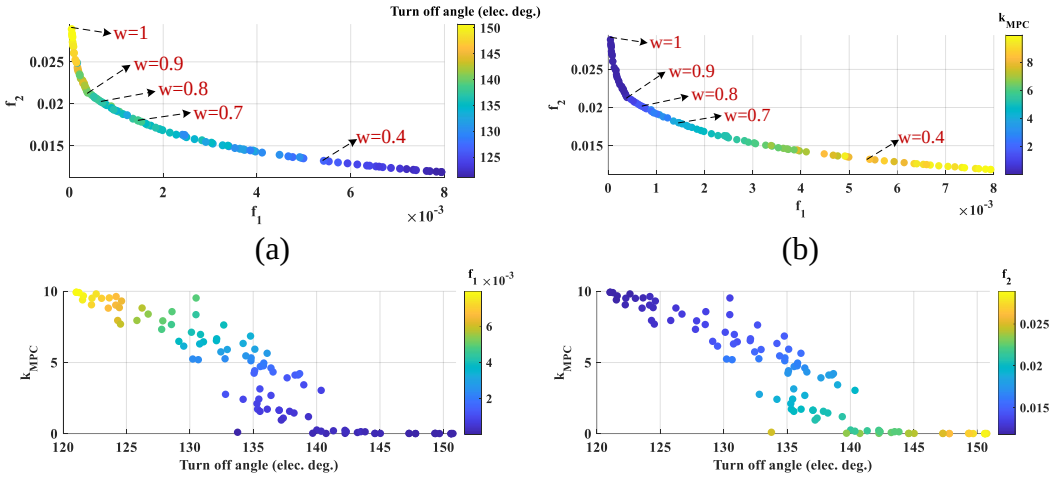

Figure 7.15: Pareto front of multi-objective optimization for SRM2 at 5000 rpm under 3 Nm; (a) variation of optimal turn off angle on pareto front, (b) variation of optimal k_{MPC} on pareto front, (c) variation of f_1 with optimization variables, and (d) variation of f_2 with optimization variables.

As stated earlier, torque tracking term (f_1) is considered the primary objective for this multi-objective optimization problem. The best torque tracking is achieved when the weighting factor (w) is set to 1. However, as discussed earlier, this condition results in undesirable switchings, non-smooth phase currents, higher rms phase current, and consequently, lower efficiency. In order to overcome this issue, the weighting factor (w) is selected as close as possible to 1 to have the minimum torque tracking error while achieving a smooth phase current waveform. Considering the optimization results at both low speed and base speed given in Figure 7.14 and Figure 7.15, respectively, the optimal weighting factor for SRM2 is selected to be $w = 0.9$ in the entire speed range.

7.4.2 Counter plots of optimal solution for SRM2

The counter plots of the GA optimization results with the selected optimal weighting factor of $w = 0.9$ are demonstrated in Figure 7.16. In all the figures, the horizontal axis represents the speed, and the vertical axis represents the shaft torque, except for Figure 7.16-a in which the vertical axis shows the reference torque. It can be concluded from Figure 7.16-a that the torque tracking error increases at higher speeds. In other words, a higher reference torque is needed to achieve a specific shaft torque at higher speeds. According to Figure 7.16-b, the optimal turn-off angle decreases by increasing the speed to limit the negative phase torque production in the generating region. The optimal k_{MPC} is dependent on both torque and speed as shown in the counter plots given in Figure 7.16-c. It can be understood from Figure 7.16-d that the rms phase current increases almost linearly with torque in the low-speed region. According to the counter plots of both percentage of torque ripple and rms torque ripple, presented in Figure 7.16-e and f respectively, it can be understood that the torque ripple increases with both speed and torque. Finally, Figure 7.16-g represents the counter plots for the peak phase current and its increase with the torque level.

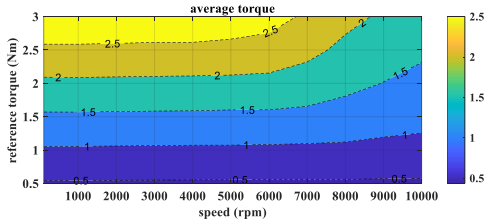

(a)

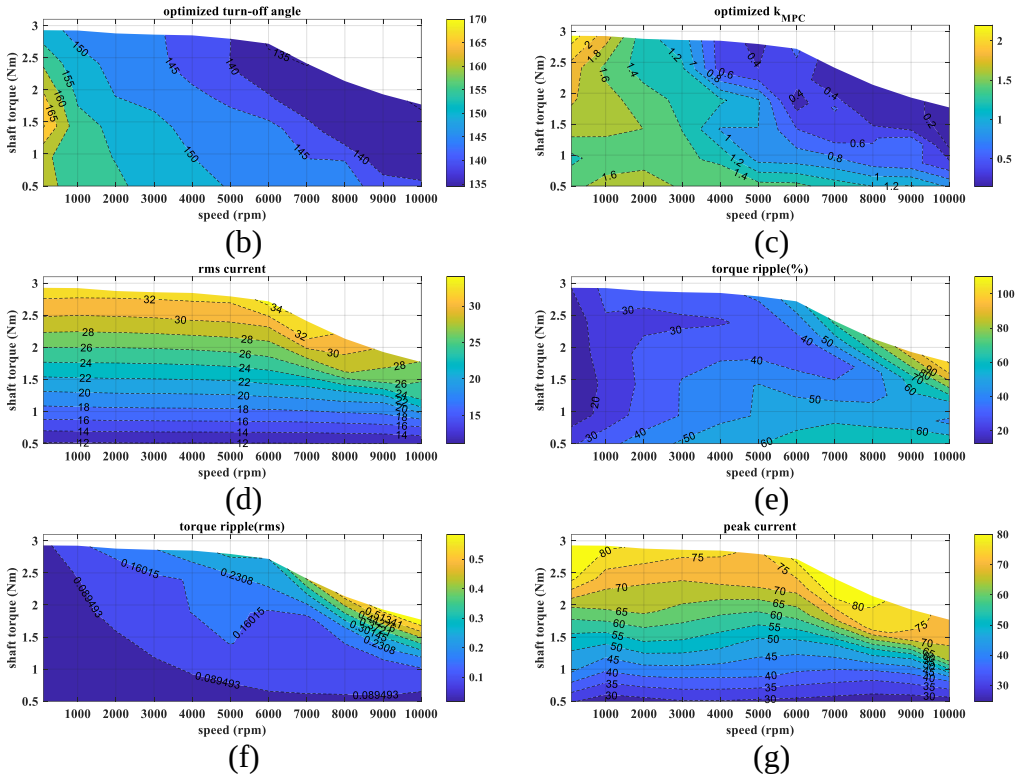

Figure 7.16: GA Optimization results for SRM2 with $w = 0.9$; (a) average torque, (b) optimum turn-off angle, (c) optimum k_{MPC}, (d) rms current, (e) torque ripple (%), (f) torque ripple (rms), and (g) peak current.

7.5 Experimental results for 12/8 5.5 kW SRM (SRM2)

The experimental test results at $n_{ref} = 2000\,rpm$ (low speed) under the load torque of $T_{ref} = 3\,Nm$ are presented in Figure 7.17. Similar to the previous experimental results, the control frequency is 20 kHz. The optimal turn-off angle and k_{MPC} (with w=0.9) at $n_{ref} = 2000\,rpm$ with the reference torque of $T_{ref} = 3\,Nm$ are 147.27° and 1.26, respectively. Comparing Figure 7.17-b and Figure 4.9-b reveals that the optimal turn-off angle is slightly advanced with the proposed

offline method compared to the conventional FCS-MPTC. As a result, the phase current peak is considerably reduced compared to the conventional FCS-MPTC as can be understood by comparing Figure 7.17-b and d with Figure 4.9-b and d, respectively. The negative phase torque is negligible according to both Figure 7.17-c and e, as the SRM operates at low-speed.

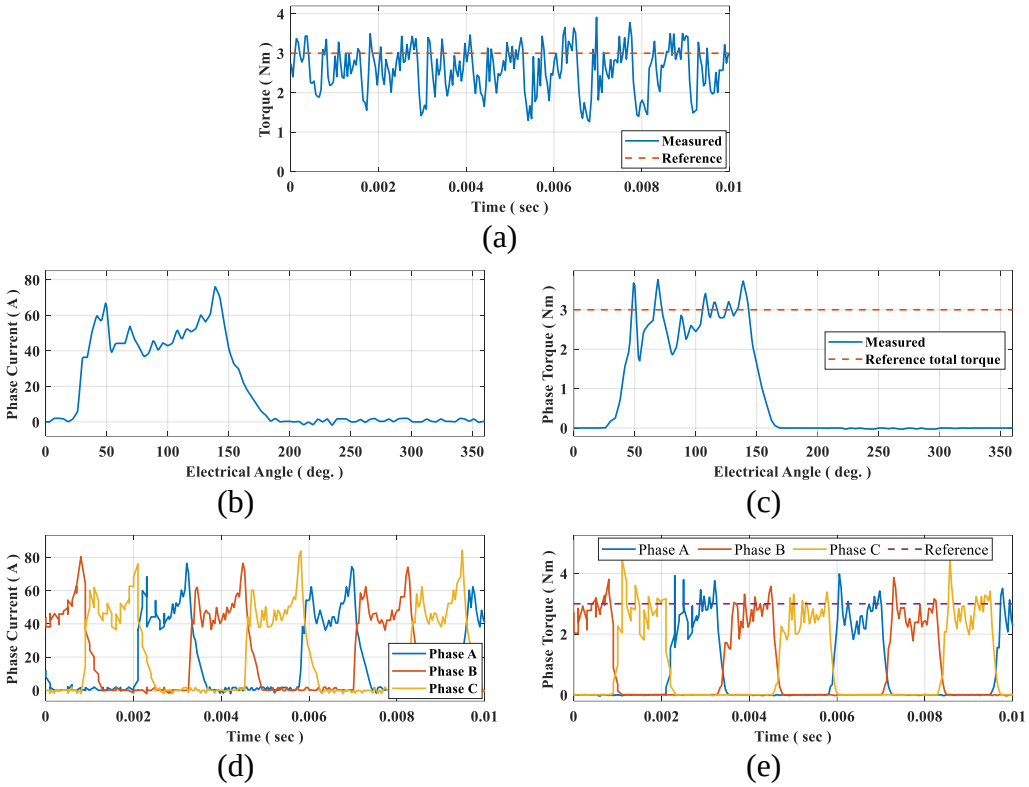

Figure 7.17: Experimental test results of SRM2 with the proposed offline optimization-based method (with w=0.9 at 20 kHz) at n_{ref}=2000 rpm (low-speed) and T_{ref}=3 Nm; (a) torque, (b) phase current in one electrical cycle, (c) phase torque in one electrical cycle, (d) phase currents, and (e) phase torques.

The experimental results of the test SRM2 for the optimal solution (with w=0.9) at $n_{ref} = 4000\,rpm$ under the load torque of $T_{ref} = 3\,Nm$ are presented in Figure

7.18. The optimal turn-off angle and k_{MPC} are 143.16° and 0.5, respectively. Comparing Figure 7.18-b with Figure 4.10-b reveals that the commutation angles are advanced with the proposed method to reduce the current tail in the generating region after the phase is turned off, and hence to reduce the phase negative torque (see Figure 7.18-c and e). Besides, the phase current peak is significantly reduced compared to the conventional FCS-MPTC as can be understood by comparing Figure 7.18-b and d with Figure 4.10-b and d, respectively. According to Figure 7.18-a and Figure 4.10-a, there is a significant improvement in the average torque with the proposed method. By comparing the measured phase current in Figure 7.18-b with both Figure 5.7-b and Figure 6.5-b, it can be concluded that the optimal phase turn-off angle with the proposed offline method is bigger than the turn-off angle with the first online method and smaller than the turn-off angle with the second online method.

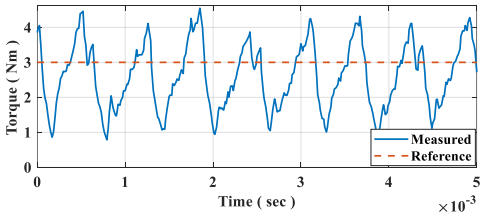

(a)

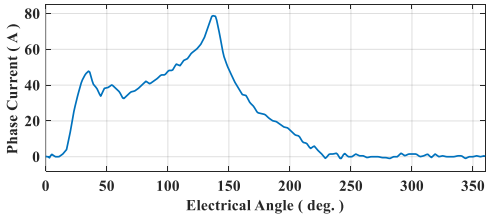

(b)

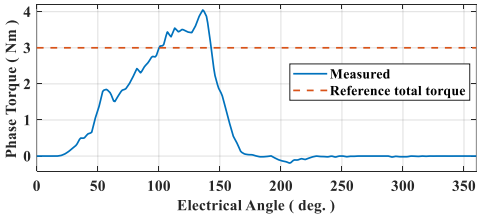

(c)

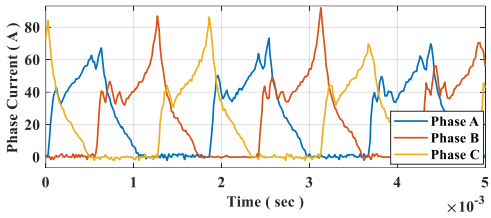

(d)

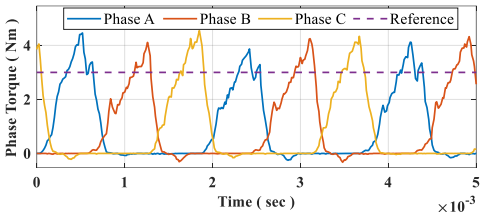

(e)

Figure 7.18: Experimental test results of SRM2 with the proposed offline optimization-based method (with w=0.9 at 20 kHz) at n_{ref}=4000 rpm and T_{ref}=3 Nm; (a) torque, (b) phase current in one electrical cycle, (c) phase torque in one electrical cycle, (d) phase currents, and (e) phase torques.

7.6 Summary

An offline multi-objective optimization-based commutation angle control method is proposed in this chapter for FCS-MPTC of SRM drives. The multi-objective optimization problem with two objective functions (average torque tracking and rms current minimization) is formulated and solved using GA optimization to determine the optimal turn-off angle and k_{MPC} in the entire operating torque and speed ranges of SRM. The optimal solution is selected after analyzing the pareto-front of the optimization problem. After presenting the contour plots of the optimal solution, the simulation results of the test SRM1 on two selected points are given to validate the performance of the proposed offline turn-off angle control method. Finally, the experimental results of SRM2 at two selected optimal points (low-speed and high-speed) show the effectiveness of the proposed offline method in adaptively controlling the commutation angles compared to the conventional FCS-MPTC.

Chapter 8

Performance Comparison of the Proposed Commutation Angle Control Methods

In this chapter, after a brief description of the indirect average torque control method with optimized conduction angles and presenting the corresponding simulation and experimental results, a quantitative comparison is carried out between the conventional FCS-MPTC, the proposed methods, and the conventional indirect average torque control with optimized angles based on simulation results for the test SRM1. Then, the simulation results of the test SRM1 for both conventional and predictive (both conventional and the proposed) torque control methods are also presented under speed dynamics. The results are then compared and discussed. Finally, a comprehensive comparative analysis is carried out based on the experimental results of the test SRM2 for conventional FCS-MPTC, the proposed methods, and the optimized hysteresis controller.

8.1 Indirect average torque control with optimized conduction angles

As the indirect average torque control is the mostly used control scheme for SRM in both literature and industrial applications, the simulations and experimental results of FCS-MPTC with and without commutation angle control are compared to the optimized indirect average torque controller. Indirect average torque controller in not capable of shaping the phase current and the current is controlled to follow a pre-defined reference current in the conduction period. However, the phase current is shaped using FCS-MPTC by selecting the optimal switching state at each sample time to achieve the desired performance. Either PWM or hysteresis current controller can be implemented to track the reference current. SRM can be controlled using conventional indirect average torque controller if three control parameters ($-90° \leq \theta_{on} \leq 90°$, $90° \leq \theta_{off} \leq 180°$, $0 \leq I_{ref} \leq I_{max}$) are known. GA optimization is used to determine the optimal control parameters to achieve the desired performance dictated by the objective function of GA as

$$f_{GA,hyst} = (T_{avg} - T_{ref})^2 + 0.5\left(\frac{I_{rms}^2}{I_{max}^2}\right) + 0.1(\Delta T_{rms})^2 \qquad (8.1)$$

under maximum rms current limit ($I_{rms} \leq 14.15$ A) of the reference SRM1. For a specific operating point (reference torque and reference speed), GA optimization is run to find the optimum control parameters (θ_{on}, θ_{off} and I_{ref}). The weighting factors are selected by trial and error in a manner to give the highest priority to average

torque tracking term. The weight of rms current minimization term is set to be half of the average torque tracking term. Torque ripple minimization term has the lowest weighting factor. Number of populations, number of stall generations, objective function tolerance and number of elite count are set to 100, 30, 0.01 and 10, respectively.

8.1.1 Simulation results

The simulation results of the optimized indirect average torque controller with hysteresis current control (soft switching) for SRM1 at n_{ref}=2000 rpm and T_{ref}=3 Nm are presented in Figure 8.1. The optimal control parameters are found to be θ_{on}=22.73°, θ_{off}=166.6° and I_{ref}=13.17 A. Similar to FCS-MPTC soft switching is implemented and the hysteresis band is set to be within 2% of the reference current in both sides.

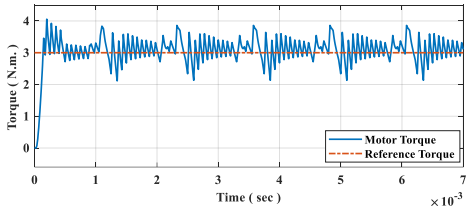

(a)

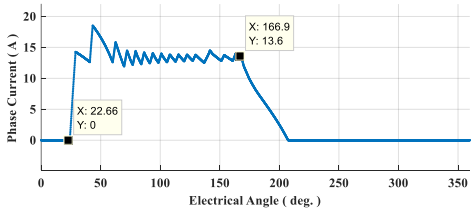

(b)

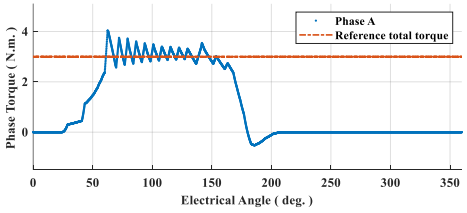

(c)

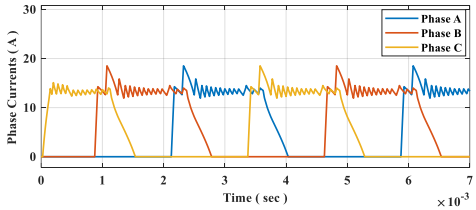

(d)

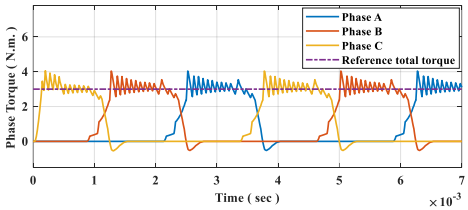

(e)

Figure 8.1: Simulation results of the test SRM1 with optimized hysteresis controller at n_{ref}=2000 rpm (low-speed) and T_{ref}=3 Nm; (a) torque, (b) phase current in one electrical cycle, (c) phase torque in one electrical cycle, (d) phase currents, and (e) phase torques.

It can be observed that the optimized hysteresis controller has a wider conduction period at 2000 rpm than FCS-MPTC leading to higher rms current. The turn-on angle is advanced more in optimized hysteresis controller compared to FCS-MPTC. The simulation results of the optimized hysteresis controller for SRM1 at n_{ref}=6000 rpm and T_{ref}=1.5 Nm are given in Figure 8.2.

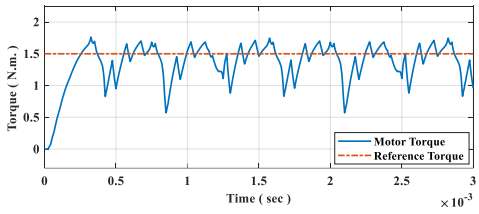

(a)

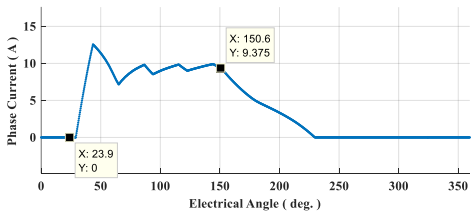

(b)

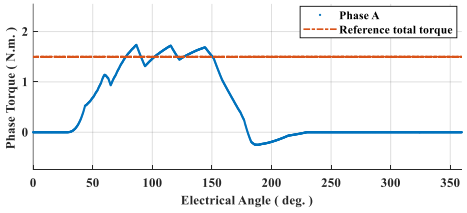

(c)

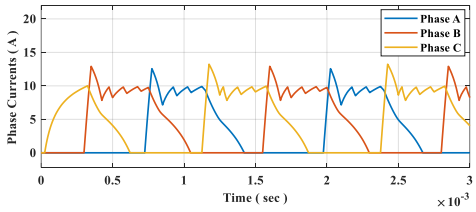

(d)

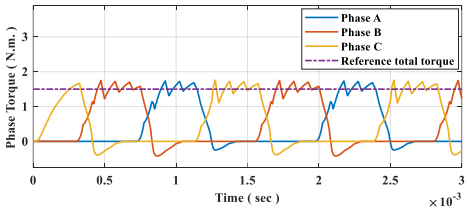

(e)

Figure 8.2: Simulation results of the test SRM1 with optimized hysteresis controller at n_{ref}=6000 rpm (base-speed) and T_{ref}=1.5 Nm; (a) torque, (b) phase current in one electrical cycle, (c) phase torque in one electrical cycle, (d) phase currents, and (e) phase torques.

It can be seen that the optimized turn-on angle is advanced more using the indirect average torque controller compared to FCS-MPTC. However, the optimized turn-off angle with indirect average torque controller is very close to both proposed online and offline FCS-MPTCs leading to a wider conduction period with optimized indirect average torque control.

8.1.2 **Experimental results**

A similar genetic algorithm optimization problem is formulated and solved for SRM2 to determine the optimal control parameters (θ_{on}, θ_{off} and I_{ref}). Look up tables of optimal control parameters (3, 2-D look up tables) in the entire operating torque and speed ranges are obtained to be used in the experimental implementations. The optimal turn-on angle, turn-off angle and the reference current at $n_{ref} = 2000\ rpm$ (low-speed) under the load torque of $T_{ref} = 3\ Nm$ are θ_{on} =24.41°, θ_{off} =162.78°, and I_{ref} =52.01 A, respectively. The experimental test results at this operating point are presented in Figure 8.3. Note that soft switching is implemented to control the

phase currents. Similar to all the previous experimental tests for predictive torque control methods, the control frequency is set to 20 kHz.

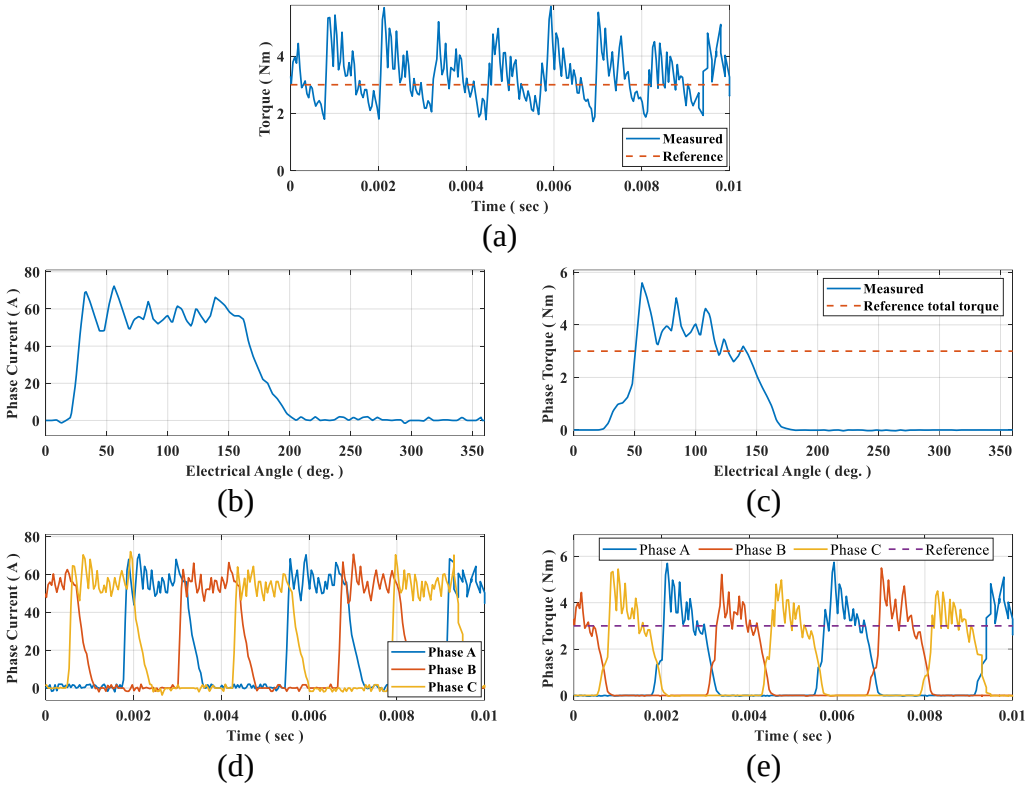

Figure 8.3: Experimental test results of SRM2 with the optimized hysteresis controller (20 kHz) at n_{ref}=2000 rpm (low-speed) and T_{ref}=3 Nm; (a) torque, (b) phase current in one electrical cycle, (c) phase torque in one electrical cycle, (d) phase currents, and (e) phase torques.

It can be observed from Figure 8.3-b that optimized hysteresis controller is not capable of shaping the phase current and the current is tracking a pre-determined reference value inside the conduction period. Moreover, it can be seen that the phase current can quickly decay to zero after the turn-off angle. According to Figure 8.3-c and e, it can be understood that the negative phase torque is negligible for SRM2 at 2000 rpm (low-speed).

The experimental test results of SRM2 at $n_{ref} = 4000\ rpm$ under the load torque of $T_{ref} = 3\ Nm$ are presented in Figure 8.4. The optimal control parameters at this operating point are found to be θ_{on} =22.05°, θ_{off} =159.3°, and I_{ref} =52.83 A.

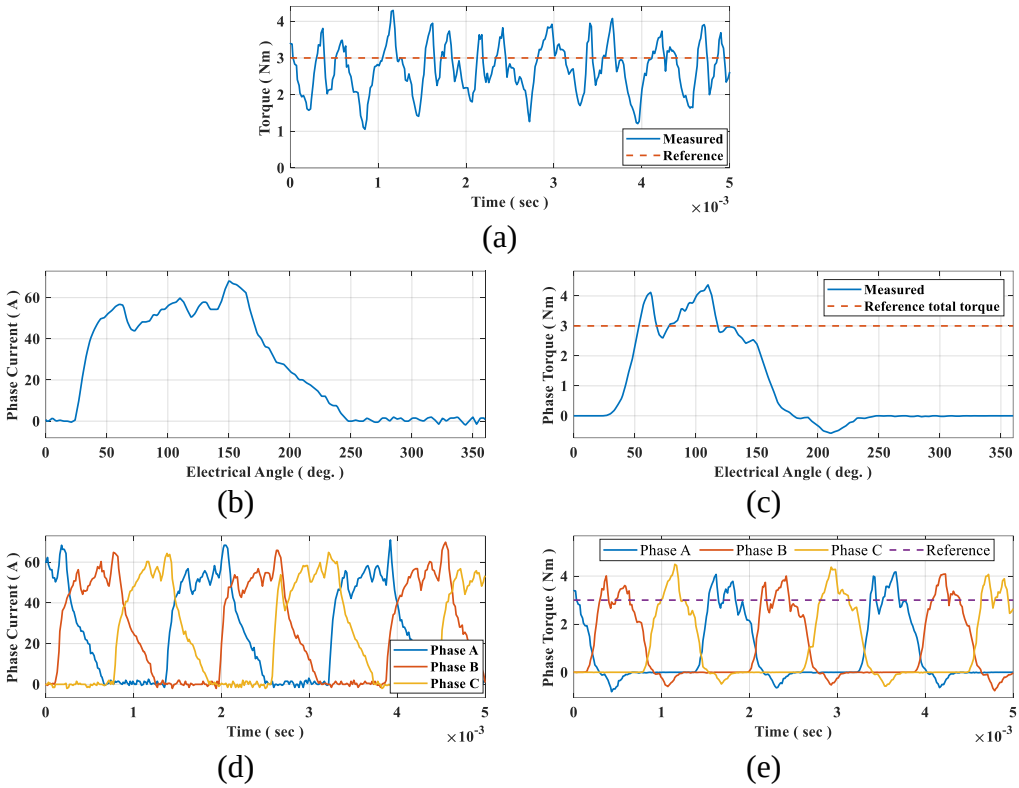

Figure 8.4: Experimental test results of SRM2 with the optimized hysteresis controller (20 kHz) at n_{ref}=4000 rpm and T_{ref}=3 Nm; (a) torque, (b) phase current in one electrical cycle, (c) phase torque in one electrical cycle, (d) phase currents, and (e) phase torques.

It can be concluded from Figure 8.4-b that the phase current cannot quickly decay to zero after the phase is turned off, and there is a current tail in the inductance falling region resulting in the phase negative torque as can be observed in both Figure 8.4-c and e.

The performance of the optimized hysteresis controller for both SRM1 and SRM2 will be compared to the conventional FCS-MPTC and the proposed control methods in this chapter.

8.2 Performance comparison for SRM1 at 2000 and 6000 rpm

The simulated performance of the reference SRM1 is summarized in Table 8.1 for FCS-MPTC with and without proposed turn-off angle control and optimized indirect average torque control with hysteresis current controller under load torque of 3.6 Nm (rated torque) at both 2000 rpm and 6000 rpm (base-speed).

Table 8.1: Comparison of the simulation results for SRM1 with the conventional FCS-MPTC, the proposed online and offline methods and the optimized hysteresis controller

Performance parameters		θ_{on} (elec. deg)	θ_{off} (elec. deg)	I_{ref} (A)	T_{avg} (Nm)	I_{RMS} (A)	T_{ripple} (%)	T_{ripple} (rms)
n_r=2000 rpm T_{ref}=3.6 Nm	Conventional FCS-MPTC	36.5	169.7	---	3.38	8.96	50.76	0.2875
	First proposed online method [32]	37.92	158.5	---	3.41	8.85	53.87	0.3687
	Second proposed online method	46	169.5	---	3.35	8.78	53.5	0.3137
	Proposed offline method (w=0.8)	42.9°	165.19°	---	3.26	8.49	48.6	0.305
	Proposed offline method (w=1)	40.42	163.92°	---	3.45	8.83	46.2	0.3082
	Optimized indirect average torque control	39.94	167.39	14.75	3.67	9.22	65.55	0.4157
n_r=6000 rpm T_{ref}=3.6 Nm	Conventional FCS-MPTC	30	173	---	1.99	10.64	219.04	1.1186
	First proposed online method	21.31	137.4	---	2.98	8.81	97.26	0.7412
	Second proposed online method	35.14	151.5	---	3.24	9.35	69.98	0.5794
	Proposed offline method (w=0.8)	27.94	149.62°	---	3.27	9.23	69.2	0.5508
	Proposed offline method (w=1)	28.8	154.64°	---	3.53	10.15	59.4	0.4795
	Optimized indirect average torque control	20.16	151.24	16.66	3.17	9.67	57.02	0.4201

The optimal turn-off angle and k_{MPC} at 2000 rpm in the offline method with w=0.8 are 165.19° and 7.02, respectively. These values are 163.92° and 2.6 if w=1 is used

in the offline method. At 6000 rpm, optimized turn-off angle and k_{MPC} are 149.62° and 1.71, respectively, in the offline method with w=0.8. With w=1, these values are 154.64° and 0.2896, respectively.

The variation of both turn-off angle and turn-on angle versus speed are plotted for the conventional FCS-MPTC and the proposed online and offline (with w=0.8) methods. The results are presented in Figure 8.5.

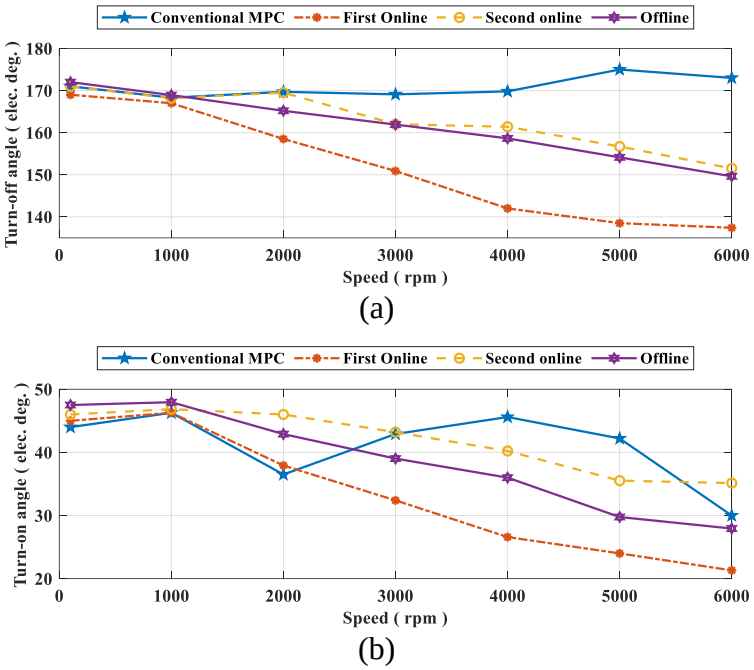

Figure 8.5: Variation of commutation angles versus speed for SRM1; (a) phase turn-off angle, and (b) phase turn-on angle.

The incapability of the conventional FCS-MPTC in controlling the commutation angles can be understood from this figure. On the other hand, it can be observed that the commutation angles are effectively advanced using the proposed online and offline methods as speed increases. The optimal commutation angles with the

second online method are closer (compared to the first online method) to the commutation angles of the proposed offline method.

For a better comparative illustration, the variation of average torque, rms current, rms torque ripple, and the percentage of torque ripple, reported in Table 8.1, are plotted in bar charts at both 2000 and 6000 rpm. The results are presented in Figure 8.6.

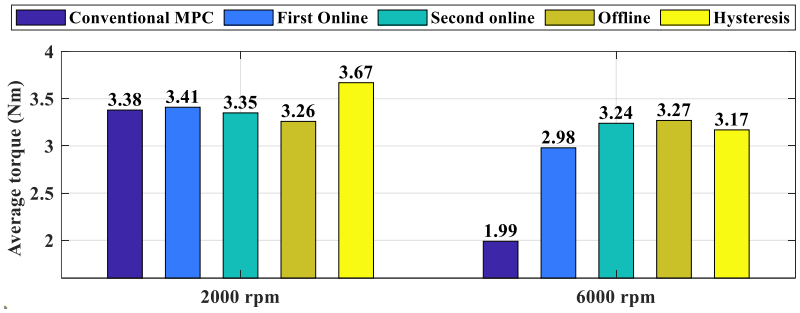

(a)

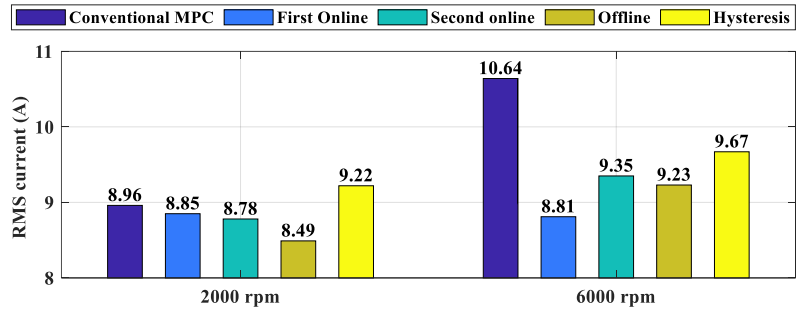

(b)

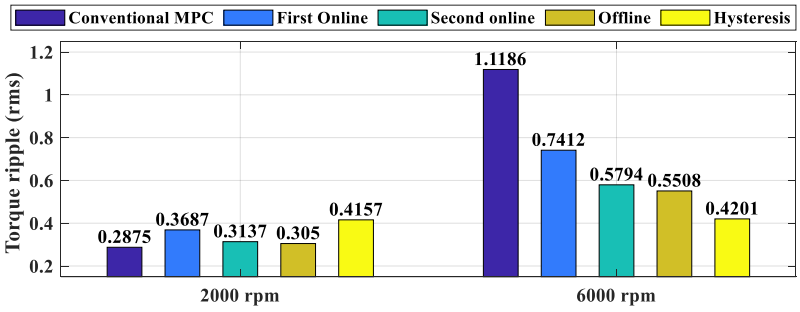

(c)

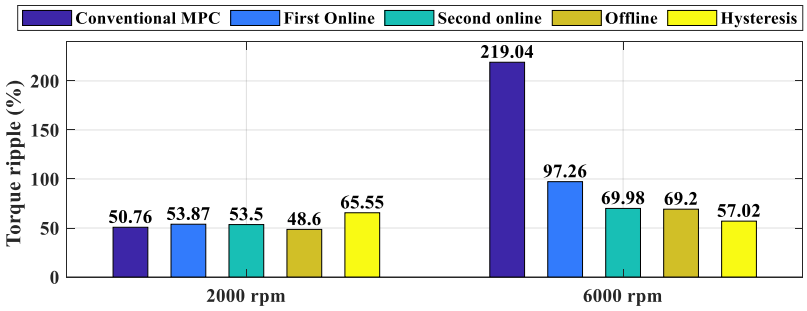

(d)

Figure 8.6: Performance comparison for SRM1 with the indirect average torque control, the conventional FCS-MPTC, and the proposed methods; (a) average torque, (b) rms current, (c) torque ripple (rms), and (d) torque ripple (%).

Considering Table 8.1, Figure 8.5 and Figure 8.6, the superior performance achieved with the proposed online and offline turn-off angle control methods can be observed by comparing the results with the conventional FCS-MPTC at 6000 rpm (base-speed). The second proposed online method shows better performance in terms of average output torque and torque ripple compared to first proposed online method and the conventional FCS-MPTC. Comparing the results of the second proposed online method with the offline optimization-based method with w=0.8 shows that both methods have almost similar performance at 6000 rpm. The turn-on angle is 8° earlier with the offline method resulting in the longer phase conduction period. The steady state average torque error which is considered as one of the main drawbacks of FCS-MPTC is observed in almost all the proposed techniques and the conventional FCS-MPTC. As stated earlier, by increasing the importance of the torque tracking term in the objective function this steady state torque error is reduced, however, less smooth current waveforms and extra unnecessary switchings are observed which results in the degraded performance of

the controller in terms of efficiency. As can be seen from the results of offline method with w=1 (torque tracking is the only objective), the torque tracking error is much lower compared to the other methods.

Comparing the results at 2000 rpm for conventional FCS-MPTC and the first proposed online method reveals that a slightly higher average torque is achieved with the online method, however, the rms current is lower. Hence, the first online method outperforms the conventional FCS-MPTC in terms of copper losses and torque tracking error. The second proposed online method results in a similar torque ripple (%) with first online method, but a lower rms torque ripple, which is a measure of torque quality in the SRM. The offline method with w=0.8 achieves the best performance in terms of torque ripple compared to both online methods, however, the average torque is slightly lower. This torque tracking error is significantly reduced when offline method with w=1 is used.

All the proposed methods outperform the optimized hysteresis controller in terms of torque ripple at 2000 rpm. However, at 6000 rpm the torque ripple is slightly lower with the hysteresis controller with optimized conduction angles. Finally, all the proposed online and offline methods show a better performance in terms of torque tracking and achieving a lower torque ripple and rms current at 6000 rpm compared to conventional FCS-MPTC. At 2000 rpm, the offline method has lower percentage of torque ripple compared to conventional FCS-MPTC, however, the

percentage of torque ripple is slightly higher with both proposed online commutation angle methods.

The copper losses can be calculated using

$$P_{cu} = mRI_{rms}^2 \tag{8.2}$$

where the phase winding resistance and number of phases are $R = 0.2117\ \Omega$ and $m = 3$ for SRM1. The calculated copper losses for the conventional FCS-MPTC, the proposed methods and the optimized hysteresis controller are compared in bar charts given in Figure 8.7. It can be observed that the proposed online and offline methods have lower copper losses compared to the conventional FCS-MPTC and the optimized hysteresis controller at both low-speed and base-speed. At base-speed, the average torque is significantly higher with the proposed methods compared to the conventional FCS-MPTC. At 2000 rpm, the average torque is slightly higher with the optimized hysteresis controller compared to the proposed predictive methods.

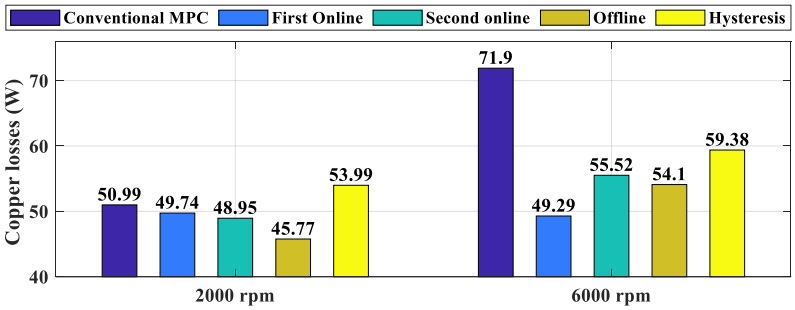

Figure 8.7: Comparison of copper losses for SRM1 with the indirect average torque control, the conventional FCS-MPTC, and the proposed methods.

The ratio of average torque over rms phase current (T_{avg}/I_{rms}), which is a representative of the torque production capability with the implemented control scheme, is calculated for the conventional FCS-MPTC, the proposed methods and the optimized hysteresis controller. The results are presented in Figure 8.8. It can be observed that the torque per ampere ratio with the proposed methods at 2000 rpm is slightly higher compared to the conventional FCS-MPTC and slightly lower than the optimized hysteresis controller. However, at 6000 rpm, the torque per ampere ratio is significantly higher with the proposed methods compared to the conventional FCS-MPTC. The torque per ampere ratio of the proposed methods is also higher compared to the optimized hysteresis controller.

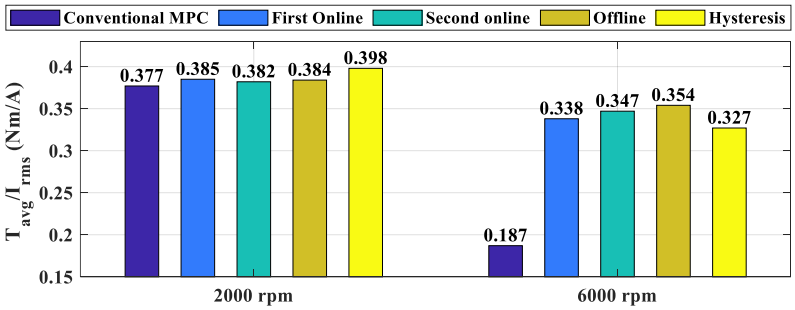

Figure 8.8: Comparison of torque per ampere ratio for SRM1 with the indirect average torque control, the conventional FCS-MPTC, and the proposed methods.

As mentioned earlier, the steady state torque tracking error is considered as one of the drawbacks of FCS-MPTC. In the proposed offline method, selecting w closer to 1 will reduce the steady state torque error with FCS-MPTC, however, rms current will increase and excessive undesirable switching will appear leading to a non-smooth current waveform and additional switching losses. Average torque tracking

capability of FCS-MPTC needs to be further improved, so that it could compete with optimized hysteresis controller.

To have a better comparison and to be able to rank the methods, the normalized performance results for the test SRM1 with conventional and proposed methods are presented in Table 8.2. In this table, the method with the best performance in terms of the specific performance parameter gets the score of 1. The scores for the other methods are calculated considering how far its performance is from the best achieved performance. Besides, the best scores and worst scores for each performance parameter are highlighted with green and red, respectively. It can be understood that the conventional FCS-MPTC has the worst performance at 6000 rpm. The proposed offline method achieves the best performance in terms of average torque and torque per ampere ratio at 6000 rpm. The first online method has the lowest copper losses. Note that optimized hysteresis controller outperforms the predictive approaches in terms of both rms and percentage of torque ripple at 6000 rpm. At 2000 rpm, the proposed offline method achieves the best performance in terms of copper losses and percentage of torque ripple. The optimized hysteresis controller has the worst performance in terms of copper losses and torque ripple at 2000 rpm.

Offline and online computational burden of both conventional and predictive methods are also compared in Table 8.2. The proposed offline method and optimized hysteresis controller require time consuming offline optimizations in the

entire operating ranges, however, the offline computational burden is low with the proposed online methods and conventional FCS-MPTC. On the other hand, the proposed online methods have a high online computational burden. The online calculation burden is lower with the offline method and the conventional FCS-MPTC. The optimized hysteresis controller has the lowest online computational burden.

Table 8.2: Normalized performance comparison for SRM1 with the indirect average torque control, the conventional FCS-MPTC, and the proposed methods.

Performance parameters		T_{avg}	P_{cu}	T_{avg}/I_{rms}	T_{ripple} (%)	T_{ripple} (rms)	Online computational burden	Offline Computational burden
n_r=2000 rpm T_{ref}=3.6 Nm	Conventional FCS-MPTC	0.921	0.897	0.947	0.957	1	medium	low
	First online method	0.93	0.92	0.967	0.902	0.78	high	low
	Second online method	0.913	0.935	0.96	0.908	0.917	high	low
	Offline method	0.888	1	0.965	1	0.943	medium	high
	Optimized hysteresis	1	0.847	1	0.741	0.691	low	high
n_r=6000 rpm T_{ref}=3.6 Nm	Conventional FCS-MPTC	0.609	0.686	0.528	0.26	0.375	medium	low
	First online method	0.911	1	0.955	0.586	0.567	high	low
	Second online method	0991	0.888	0.98	0.815	0.725	high	low
	Offline method	1	0.911	1	0.824	0.763	medium	high
	Optimized hysteresis	0.97	0.83	0.924	1	1	Low	high

To compare the overall performance of the control methods at 2000 rpm, the spider (radar) charts, presented in Figure 8.9, are plotted. To derive the spider charts, the values of the specific control parameter for different methods are normalized with respect to the control scheme achieving the best performance in terms of that control parameter (the results are presented in Table 8.2). According to Figure 8.9, the offline method achieves the best performance in terms of copper losses and

percentage of the torque ripple. It can be concluded that the conventional FCS-MPTC has a comparable performance with respect to the proposed methods at low-speed. It even outperforms the proposed methods in terms of rms torque ripple. The optimized hysteresis controller achieves the best performance in terms of average torque and torque per ampere ratio, however, it has the worst performance in terms of copper losses, percentage of torque ripple and rms torque ripple. There is not a considerable difference between the performance of the proposed first and second online methods except for the rms torque ripple; the second online method achieves a lower rms torque ripple.

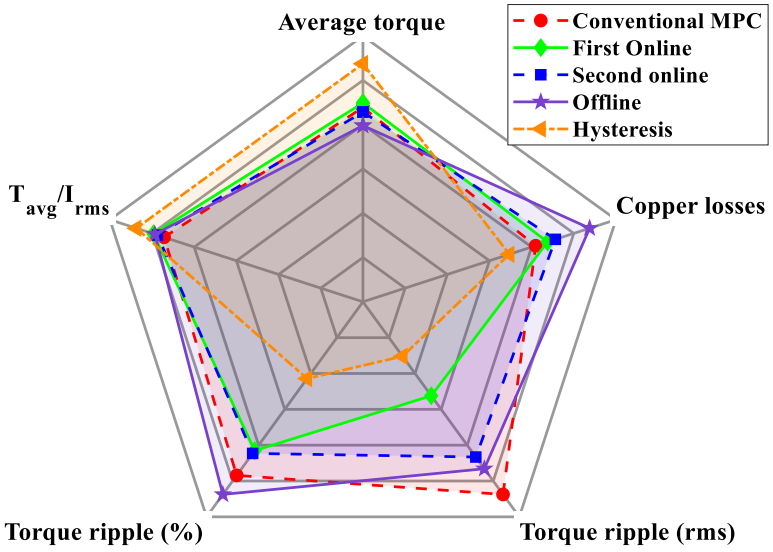

Figure 8.9: Overall performance comparison for SRM1 at 2000 rpm with the indirect average torque control, the conventional FCS-MPTC, and the proposed methods.

A similar spider chart is plotted to compare the overall performance of different control methods at 6000 rpm (base-speed). The spider chart is presented in Figure 8.10. It can be observed that the proposed online and offline methods have

significantly better overall performance compared to the conventional FCS-MPTC. The proposed second online method and the offline method reveal quite similar performance at the base-speed, and they achieve the highest average torque and torque per ampere ratio. The first proposed online method has the best performance in terms of copper losses. The optimized hysteresis controller has the lowest torque ripple (both rms and the percentage of torque ripple). Its overall performance outperforms the conventional FCS-MPTC, however all the proposed predictive approaches have higher torque per ampere ratio and lower copper losses compared to the optimized hysteresis controller. It can also be understood that the second online method and the offline method have better overall performance compared to the first online method, except the first online method has a lower rms current (copper losses).

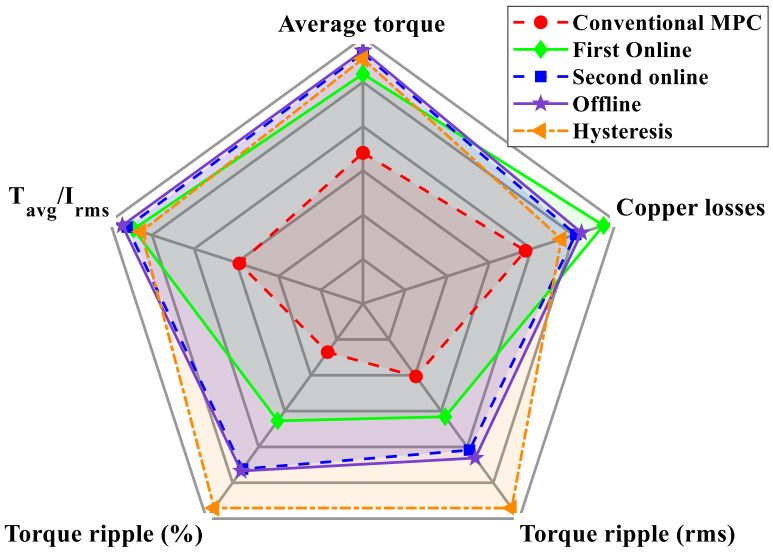

Figure 8.10: Overall performance comparison for SRM1 at 6000 rpm (base-speed) with the indirect average torque control, the conventional FCS-MPTC, and the proposed methods.

Comparing the overall performance of the conventional FCS-MPTC, the proposed methods and the optimized hysteresis controller at both 2000 rpm and 6000 rpm reveals the effectiveness of the proposed methods in adaptively adjusting the commutation angles as the speed increases to achieve a considerably enhanced performance compared to the conventional FCS-MPTC.

8.3 Simulation results of SRM1 under speed dynamics

Figure 8.11 shows the simulation results of SRM1 controlled by two conventional methods (ITC with optimum conduction angles (Figure 8.11-a) and linear TSF (Figure 8.11-b)) and four predictive control approaches (conventional FCS-MPTC (Figure 8.11-c), first proposed online method (Figure 8.11-d) [32], second proposed online method (Figure 8.11-e), and the proposed offline method (Figure 8.11-f)). The test 3-phase, 12/8, 2.3 kW SRM (SRM1) driven by an asymmetric bridge converter with the DC link voltage of 300 V and the flux linkage and torque characteristics given in Figure 2.2 is simulated to evaluate the performance of these techniques at different speeds. A constant reference torque of 2.5 N.m. is set while the speed changes from 1000 to 6000 rpm to investigate the performance of the controllers in a wide speed range. By neglecting mechanical transients, it is assumed that the SRM speed is dictated by a stiff load (dyno machine) in a back to back connection. To have a fair comparison, the maximum switching frequency is set to 20 kHz in all the controllers.

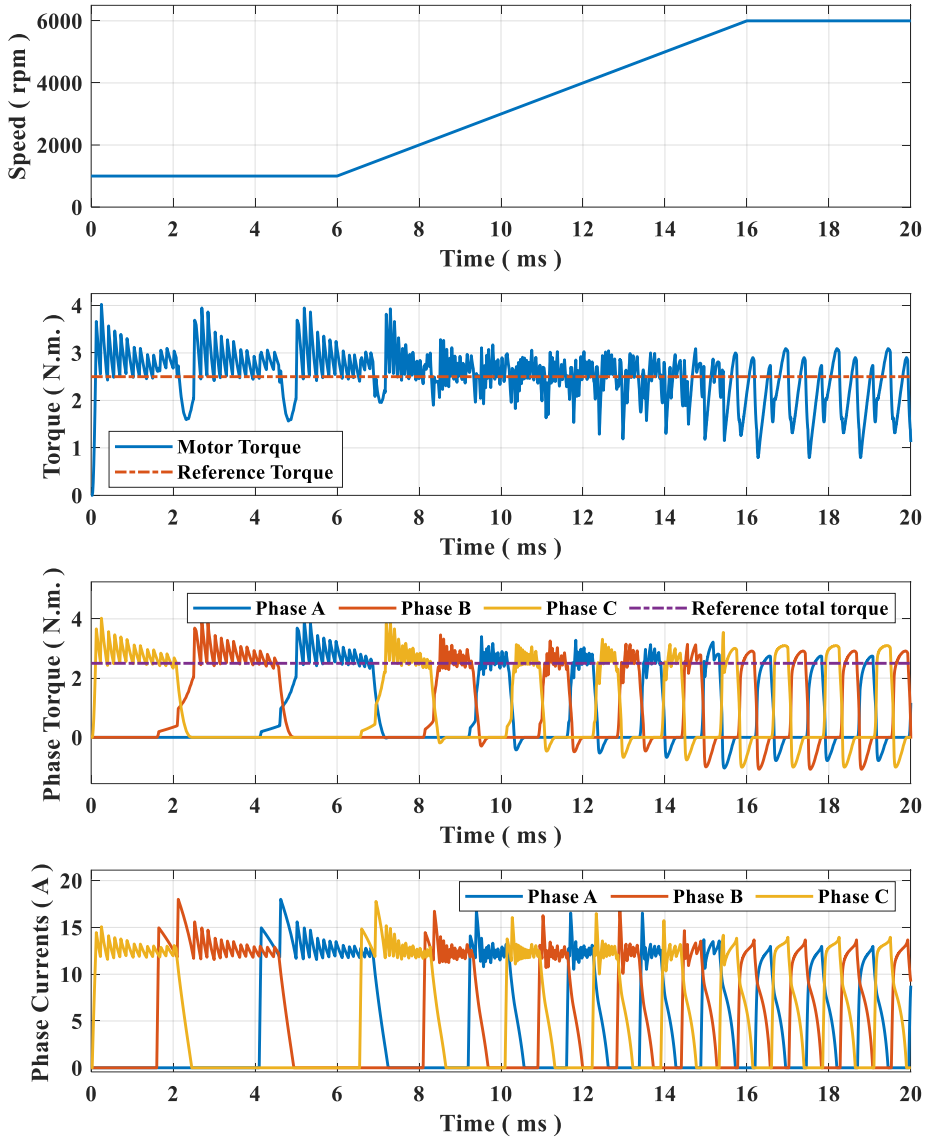
Speed (rpm)
Time (ms)
Torque (N.m.)
Motor Torque
Reference Torque
Phase Torque (N.m.)
Phase A
Phase B
Phase C
Reference total torque
Phase Currents (A)

(a)

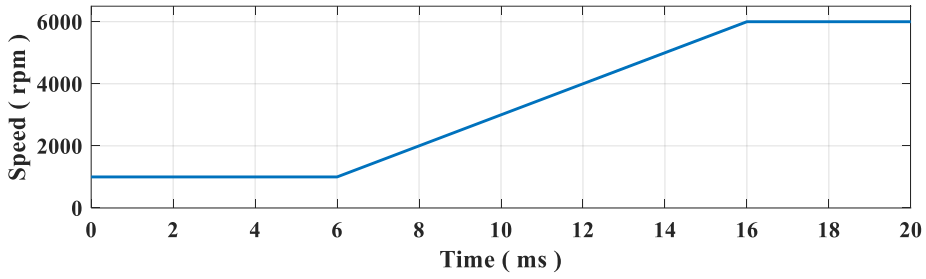
Speed (rpm)
Time (ms)

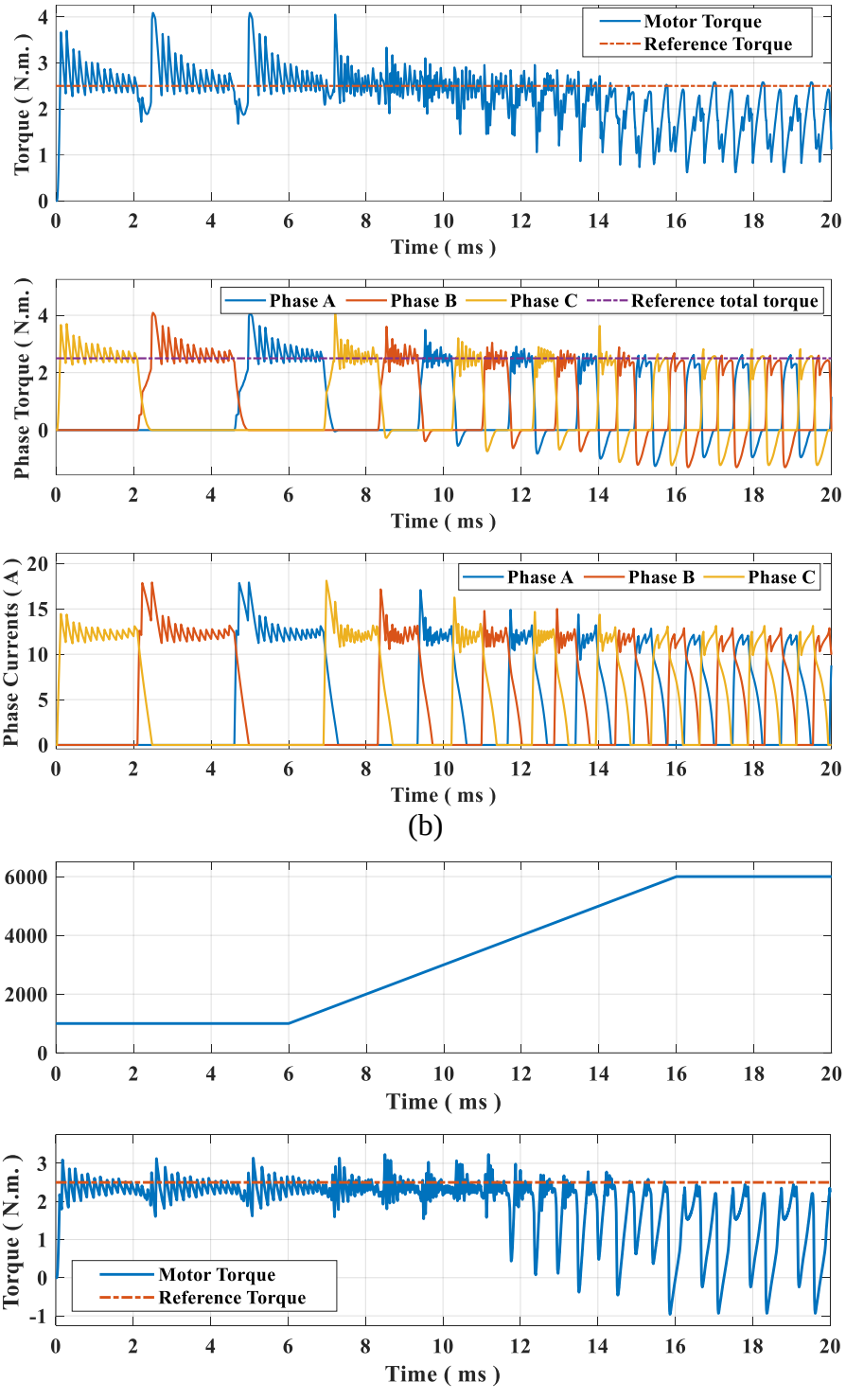
Motor Torque
Reference Torque
Torque (N.m.)
Time (ms)
Phase A
Phase B
Phase C
Reference total torque
Phase Torque (N.m.)
Time (ms)
Phase A
Phase B
Phase C
Phase Currents (A)
Time (ms)
Speed (rpm)
Time (ms)
Motor Torque
Reference Torque
Torque (N.m.)
Time (ms)

(b)

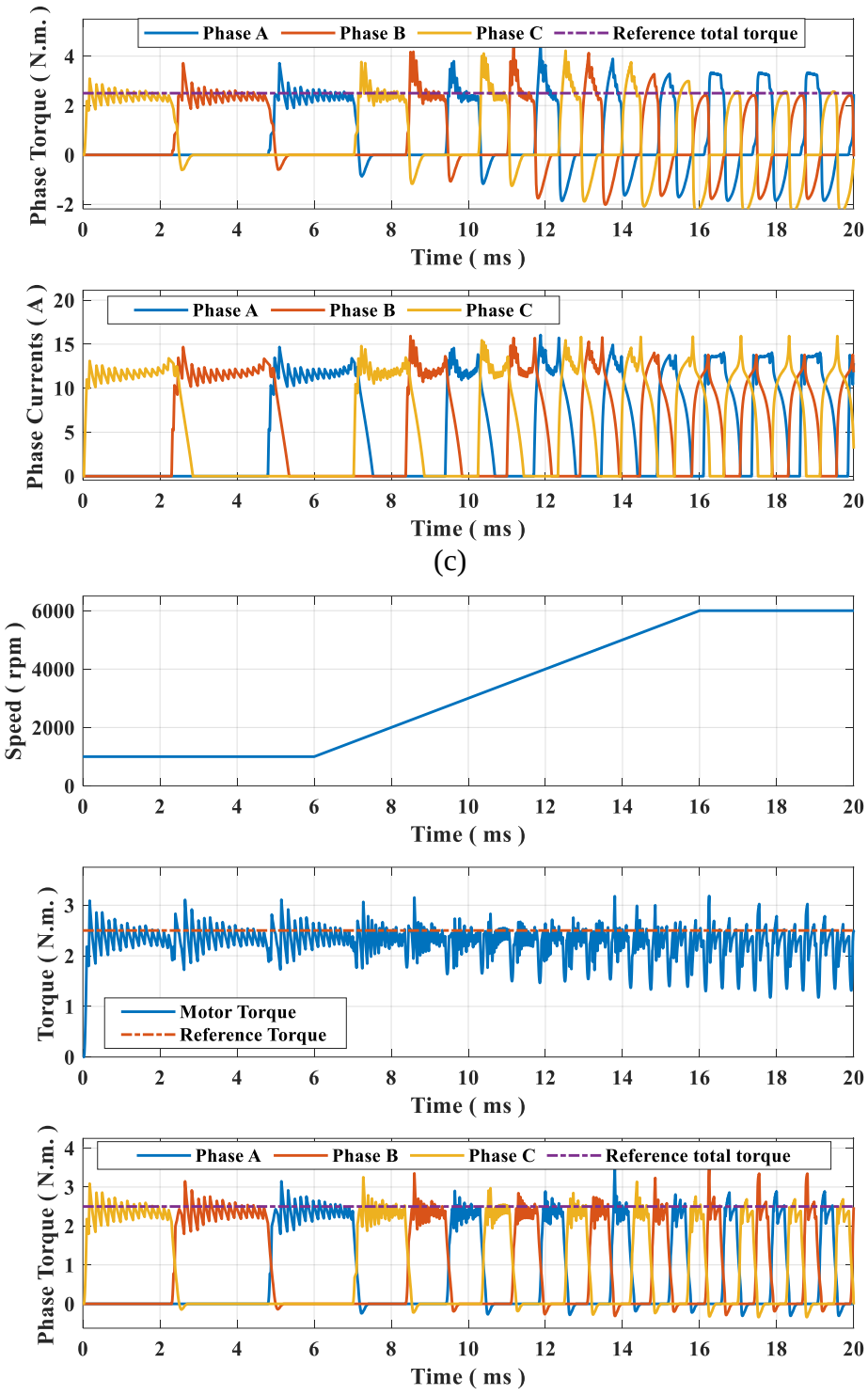
Phase A
Phase B
Phase C
Reference total torque
Phase Torque (N.m.)
Time (ms)
Phase A
Phase B
Phase C
Phase Currents (A)
Time (ms)
Speed (rpm)
Time (ms)
Motor Torque
Reference Torque
Torque (N.m.)
Time (ms)
Phase A
Phase B
Phase C
Reference total torque
Phase Torque (N.m.)
Time (ms)

(c)

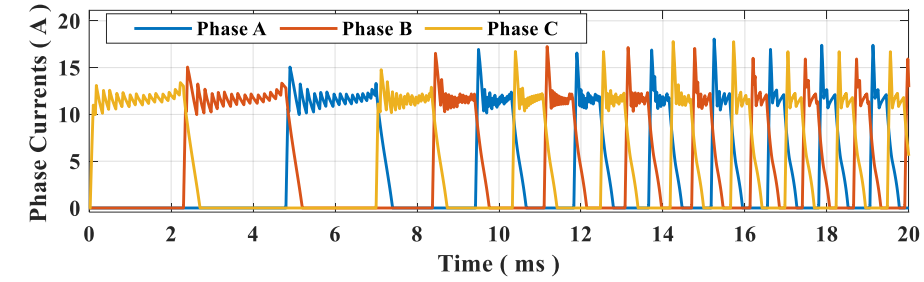
Phase A
Phase B
Phase C
Phase Currents (A)
Time (ms)

(d)

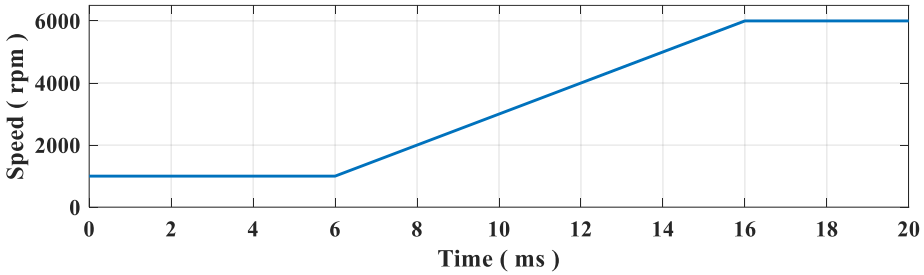
Speed (rpm)
Time (ms)

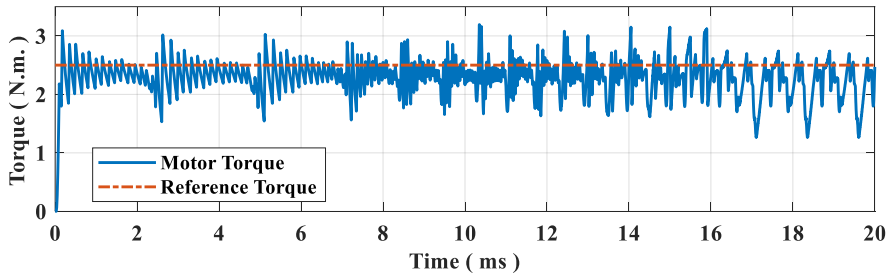
Motor Torque
Reference Torque
Torque (N.m.)
Time (ms)

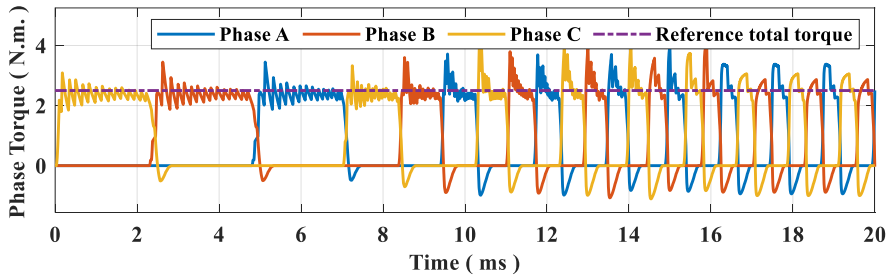
Phase A
Phase B
Phase C
Reference total torque
Phase Torque (N.m.)
Time (ms)

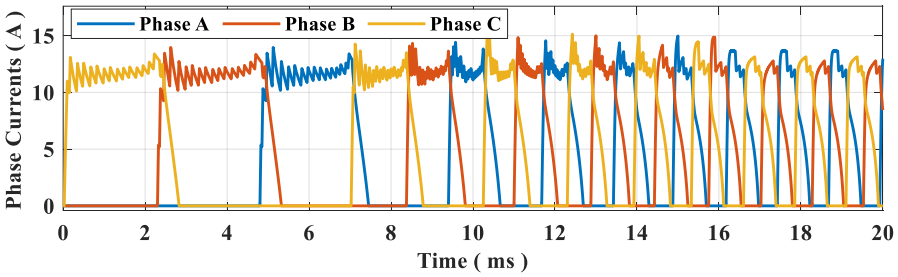
Phase A
Phase B
Phase C
Phase Currents (A)
Time (ms)

(e)

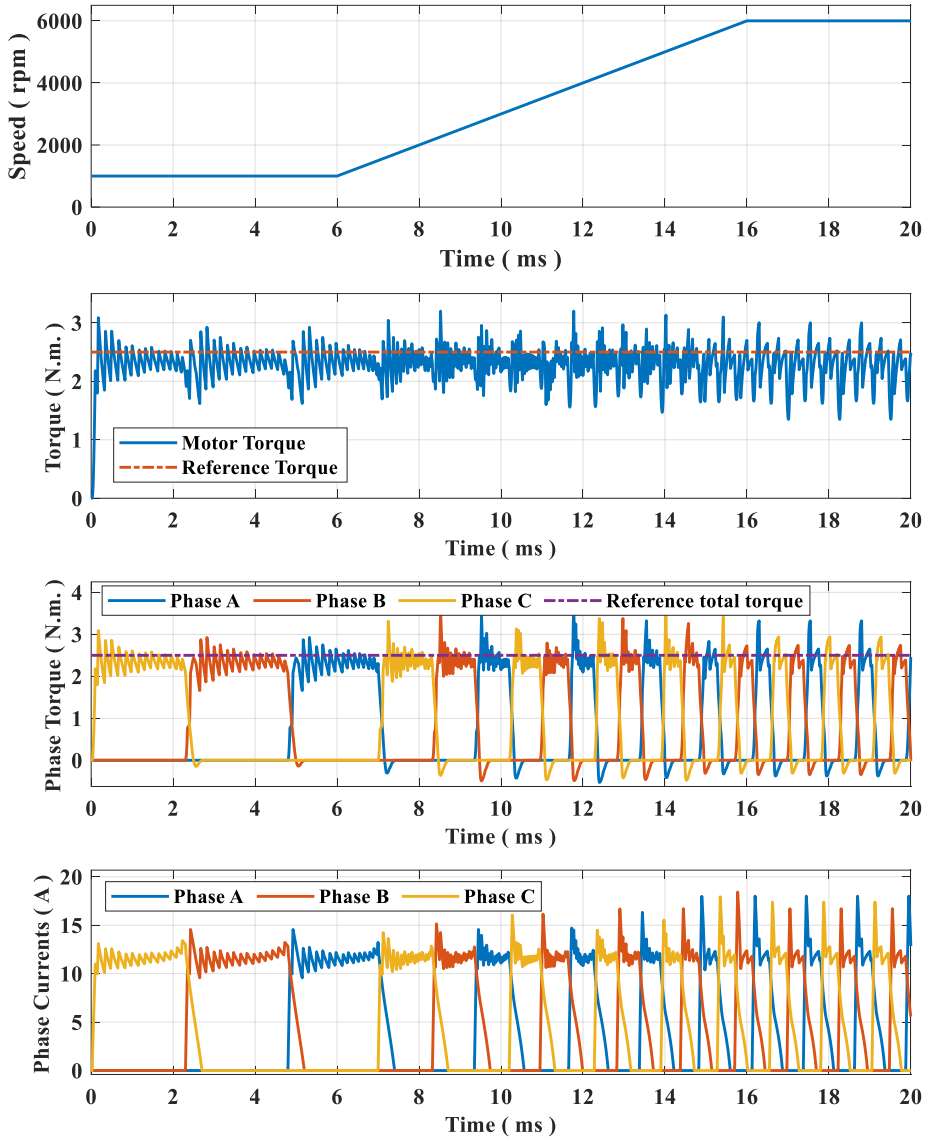

(f)

Figure 8.11: Performance of torque control techniques in SRM: (a) indirect torque control with optimum conduction angles, (b) linear TSF, (c) conventional FCS-MPTC, (d) FCS-MPTC with the first proposed online method, (e) FCS-MPTC with the second proposed online method, and (f) FCS-MPTC with the proposed offline method.

Figure 8.11-a shows the results for ITC control with optimized conduction angles.

Genetic algorithm (GA) optimization is used to obtain optimal commutation angles

(θ_{on}, θ_{off}) and reference currents to minimize both current and torque ripple [44]. Although the reference torque is tracked, torque ripple at low speed is still high, as the controller fails to evenly distribute the torque during phase commutation. Moreover, at high-speed, the machine operates in single-pulse mode, thus matching the average torque but increasing ripple. On the other hand, the θ_{on}, θ_{off} and overlapping angles for the linear TSF in Figure 8.11-b are selected to be 5°, 20° and 2.5° (mechanical), respectively. These angles are obtained from optimization to minimize the copper losses [23]. This technique, however, is not suitable for high-speed without the proper back-emf compensation [26]. Note that hysteresis current controller with soft switching is integrated with both ITC and TSF to track the reference phase currents.

Figure 8.11-c shows the response considering the conventional FCS-MPTC like the one proposed in [21], while Figure 8.11-d enhances this technique by adaptively controlling the commutation angles using the first proposed online method [32]. The simulation results of the second proposed online method and the proposed offline method are presented in Figure 8.11-e and f, respectively. In the low-speed region, the reference torque is properly tracked in predictive methods, with a lower torque and current ripples than in the conventional ones in Figure 8.11-a and b. As a result, higher efficiency and lower vibrations might be obtained. Figure 8.11-c evidences the lack of tracking ability of the conventional FCS-MPTC in the high-speed region. In practice, a suitable solution considers advancing θ_{on} so the current

has enough time to build up, and hence, the operating speed range of SRM can be extended. This is known as the natural field weakening of the SRM. The incapability of the conventional FCS-MPTC in Figure 8.11-c of considering negative angles comes from the definition of the cost function. As the cost function minimizes the torque ripple, it is not possible to consider the inclusion of negative torque production from the advanced angle, as discussed in [32]. Fortunately, the flexibility in the problem definition in predictive control allows defining an adaptive commutation angle control to improve the performance in high-speed region, thus guaranteeing a proper tracking in Figure 8.11-d and Figure 8.11-e. The control of commutation angles is done based on multi-objective optimization results in Figure 8.11-f. By advancing the turn-off angle, the outgoing phase takes time to reduce the current, and a small negative torque is produced before it turns-off. The negative torque is compensated by the upcoming phase, thus increasing the total current and degrading the efficiency. Figure 8.11-a to c evidence this issue, which is solved by a proper consideration of the deactivation time within the compensated angles in Figure 8.11-d, e and f. Comparing the results of three proposed predictive approaches reveals that the first proposed online method has the minimum negative phase torque. In other words, it has the maximum advancement of the turn-off angle. On the other hand, the second proposed online method has the largest phase negative torque, and consequently it does not have the high current peaks near the unaligned position at higher speeds which is observed with both first online and the offline methods. It is also worth mentioning that

conventional techniques require extensive computational burden for offline optimizations and larger memory space for look up tables during experimental implementation. However, there is no need for offline calculations in FCS-MPTC.

8.4 Performance comparison for SRM2

In this section, the performance of the test SRM2 is compared for the conventional FCS-MPTC, the proposed methods and the optimized hysteresis controller. The measured phase currents and phase torques of SRM2 at $n_{ref} = 2000\ rpm$ (low-speed) under the load torque of $T_{ref} = 3\ Nm$ are compared in Figure 8.12-a and Figure 8.12-b, respectively. It can be understood from Figure 8.12-a that the conventional FCS-MPTC is not capable of controlling the turn-off angle. Consequently, there is a huge current peak close to the aligned position with the conventional FCS-MPTC. According to Figure 8.12-a, the proposed offline method has the most advanced turn-off angle. The turn-off angle is advanced more with the first online method compared to the second online method. Advancing the phase turn-off angle with the proposed methods results in a significantly reduced phase current peak as can be seen in Figure 8.12-a. Note that the turn-on angle is also automatically advanced by the predictive controller to deliver the desired reference torque on the shaft. Note that the optimized hysteresis controller is not capable of shaping the current and a pre-determined reference current is tracked inside the conduction period. Hence, the predictive approach leads to a better performance in

terms of torque ripple compared to the optimized hysteresis controller at lower speeds. It can be observed that the phase negative torque is negligible at 2000 rpm with all the methods as can be understood from Figure 8.12-b.

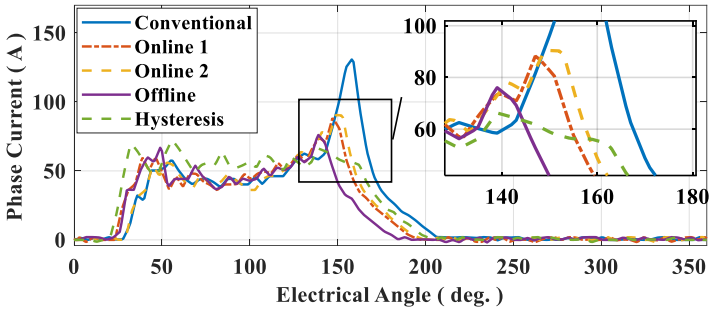

(a)

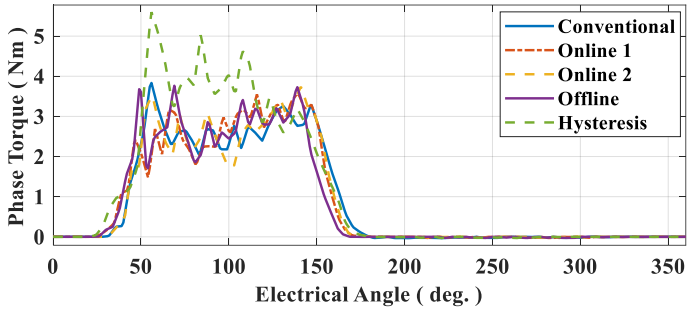

(b)

Figure 8.12: Performance comparison for the test SRM2 at 2000 rpm under load torque of 3 Nm (a) measured phase current, and (b) measured phase torque.

The total torque of the SRM2 obtained using experimental results is presented in Figure 8.13 for the conventional FCS-MPTC, the proposed methods and the optimized hysteresis controller at 2000 rpm with the reference torque of 3 Nm. It is obvious that the torque ripple is higher with the conventional FCS-MPTC compared to the proposed methods. According to Figure 8.13, the torque ripple is also high with the optimized hysteresis controller, as it is not capable of shaping the phase current.

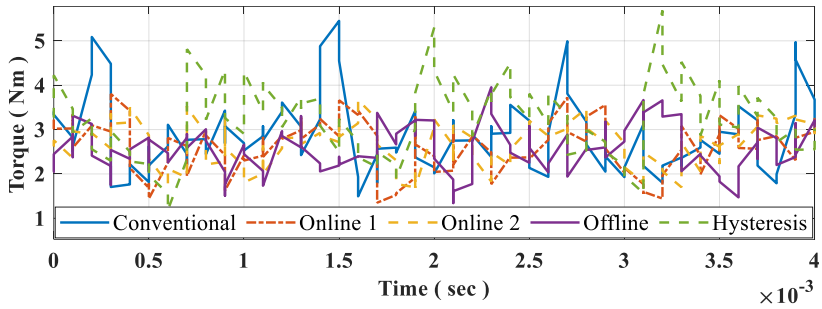

Figure 8.13: Comparison of the total torque of SRM2 obtained using experimental tests at 2000 rpm, and under load torque of 3 Nm.

The measured phase currents and phase torques of the test SRM 2 at $n_{ref} = 4000\ rpm$ under the load torque of $T_{ref} = 3\ Nm$ are compared in Figure 8.14-a and b, respectively. The incapability of the conventional FCS-MPTC in advancing the commutation angles as the speed increases is obvious from Figure 8.14-a. This results in a large peak phase current and large phase negative torque with the conventional FCS-MPTC according to Figure 8.14-a and b, respectively. The first proposed online method has the maximum commutation angle advancement and the smallest phase negative torque. The commutation angle advancement with the proposed offline method is smaller than the first online method and bigger than the second online method. It reveals that the optimal phase negative torque (which is achieved with the offline method) is smaller than the negative torque with the second method and bigger than the phase negative torque with the first method. According to Figure 8.14-b, the phase negative torque with the hysteresis controller is larger than the proposed control strategies and smaller than the conventional FCS-MPTC.

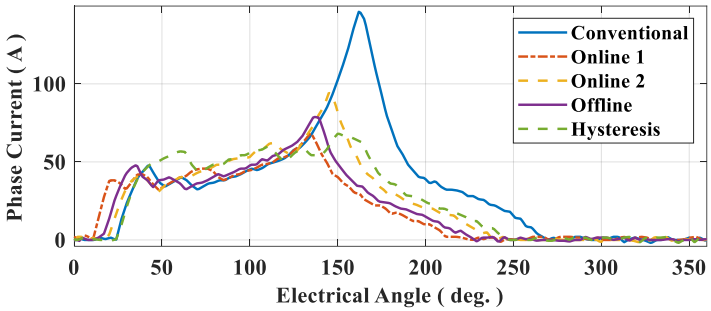

(a)

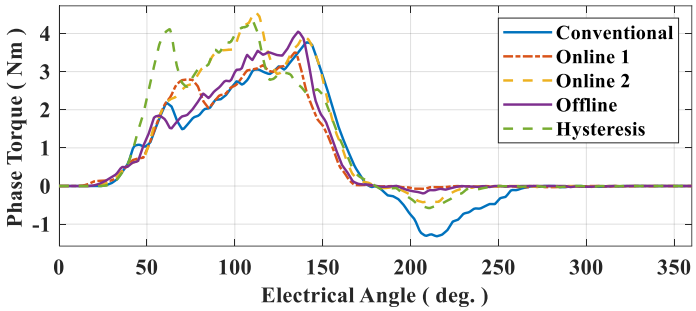

(b)

Figure 8.14: Performance comparison for the test SRM2 at 4000 rpm under load torque of 3 Nm (a) measured phase current, and (b) measured phase torque.

The torque waveform of the test SRM2 obtained using experimental results at 4000 rpm with the reference torque of 3 Nm is demonstrated in Figure 8.15 for the conventional FCS-MPTC, the proposed methods and the optimized hysteresis controller. The conventional FCS-MPTC has a lower average torque compared to the other control schemes. In the next section, a quantitative comparison is carried out for a more detailed performance analysis with different methods.

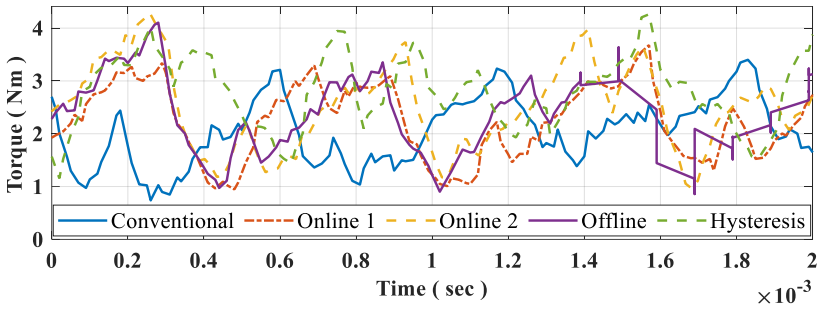

Figure 8.15: Comparison of the total torque of SRM2 obtained using experimental tests at 4000 rpm, and under load torque of 3 Nm.

Table 8.3 summarizes the experimental performance calculation results for the test SRM2 with the conventional FCS-MPTC, the proposed methods and the optimized hysteresis controller at both 2000 rpm and 4000 rpm under the load torque of 3 Nm.

Table 8.3: Comparison of the experimental results for SRM2 with the conventional FCS-MPTC, the proposed online and offline methods and the optimized hysteresis controller

Performance parameters		T_{avg} (Nm)	I_{RMS} (A)	T_{ripple} (%)	T_{ripple} (rms)
n_r=2000 rpm T_{ref}=3 Nm	Conventional FCS-MPTC	2.78	40.5	165.2	0.6652
	First proposed online method	2.65	32.7	112	0.6208
	Second proposed online method	2.73	35.76	114.6	0.5442
	Proposed offline method (w=0.9)	2.58	31.26	108.5	0.585
	Optimized indirect average torque control	3.27	35.4	142.7	0.8722
n_r=4000 rpm T_{ref}=3 Nm	Conventional FCS-MPTC	2.12	45.6	146.8	0.7453
	First proposed online method	2.32	28.68	145.3	0.7396
	Second proposed online method	2.58	34.12	135.6	0.6858
	Proposed offline method (w=0.9)	2.59	31.24	141.2	0.7125
	Optimized indirect average torque control	2.74	34.2	125.9	0.6778

For a better comparative illustration, the experimental performance for different control methods is compared using the bar charts presented in Figure 8.16. It can be observed that at 2000 rpm (low speed) the proposed control methods have lower

rms current and torque ripple (both rms and percentage of torque ripple) compared to the conventional FCS-MPTC. The average torque is slightly higher with the conventional FCS-MPTC. As the optimized hysteresis controller is not capable of shaping the phase current, it has the highest rms torque ripple at low-speed according to Figure 8.16-c. The percentage of torque ripple is also higher with the optimized hysteresis controller compared to the proposed predictive methods. On the other hand, the average torque is higher with the optimized hysteresis controller.

At 4000 rpm, all the proposed methods achieve higher average torque, lower rms current and lower torque ripple (both rms and the percentage of torque ripple) compared to the conventional FCS-MPTC, hence, proving the promising performance of the proposed control methods at higher speeds. The second online and offline methods have almost similar performance in terms of average torque. Besides, they achieve a higher average torque than the first online method. The second online method achieves lower torque ripple compared to both first online and offline methods, however it has a higher rms current. The optimized hysteresis controller has a higher average torque and rms current compared to the proposed predictive schemes. Furthermore, it has a lower torque ripple (both rms and percentage of torque ripple) than the proposed methods. It can be concluded that with the significant performance improvements achieved with the proposed methods, the predictive controller can compete with the optimized hysteresis controller at higher speeds.

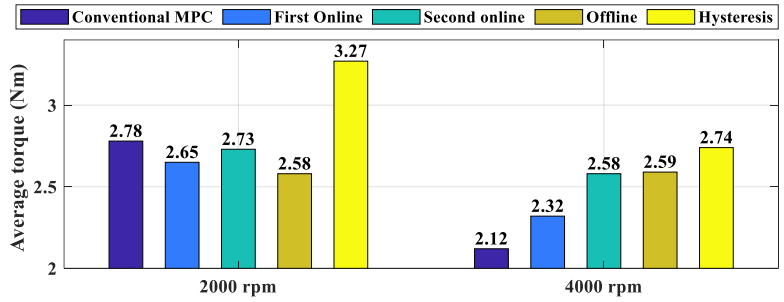

(a)

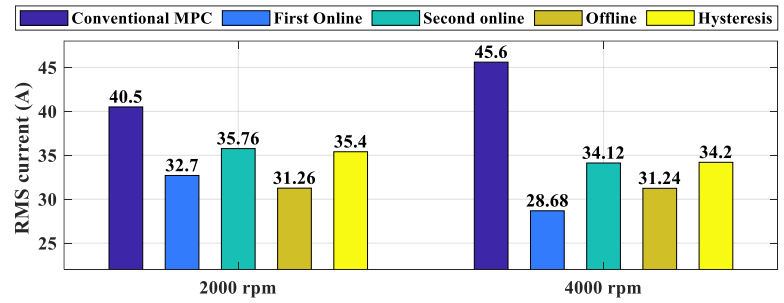

(b)

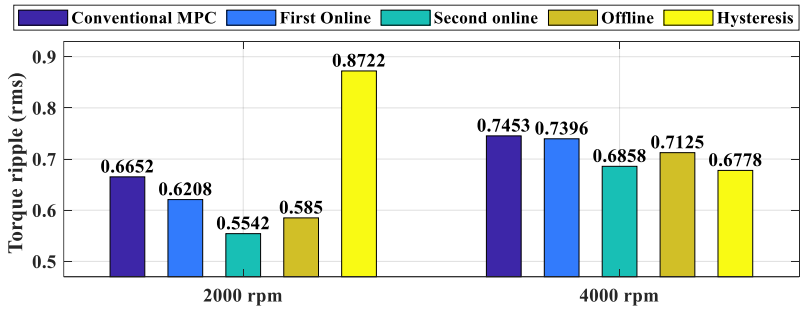

(c)

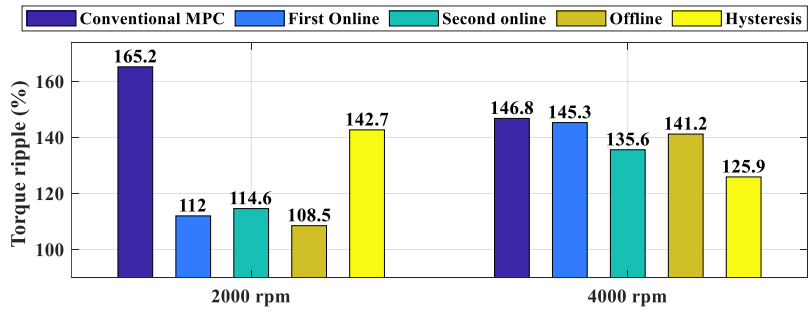

(d)

Figure 8.16: Comparison of the experimental results for SRM2 with the indirect average torque control, the conventional FCS-MPTC, and the proposed methods; (a) average torque, (b) rms current, (c) torque ripple (rms), and (d) torque ripple (%).

The copper losses are calculated for different control methods using equation (8.2). Note that the measured phase resistance and the number of phases for SRM2 are $R = 7.6\,m\Omega$ and $\mathrm{m} = 3$, respectively. The copper loss calculation results are presented in Figure 8.17. The conventional FCS-MPTC has higher copper losses compared to the proposed methods and the optimized hysteresis controller at 2000 rpm. It can be observed that there is a significant reduction in copper losses with the proposed methods compared to the conventional FCS-MPTC at 4000 rpm. Note that at 4000 rpm a higher average torque is also achieved with the proposed schemes.

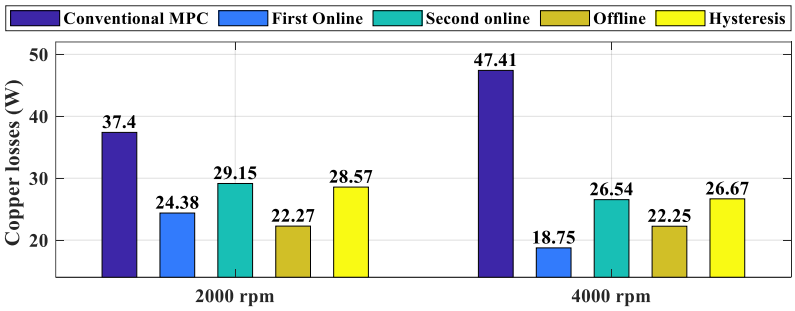

Figure 8.17: Comparison of copper losses for SRM2 with the indirect average torque control, the conventional FCS-MPTC, and the proposed methods.

To investigate the torque production capability of the control methods, the torque per ampere ratio is compared in Figure 8.18. It can be observed that the proposed methods achieve a higher torque per ampere ratio compared to the conventional FCS-MPTC at 2000 rpm. The optimized hysteresis controller has the highest torque per ampere ration at 2000 rpm. At 4000 rpm, a significant improvement is observed with the proposed control schemes compared to the conventional FCS-MPTC. The offline and first online methods achieve slightly higher torque per ampere ratio

compared to the optimized hysteresis controller. The second online method has the lowest torque per ampere ratio compare to both offline and first online methods at both low speed and high speed operations.

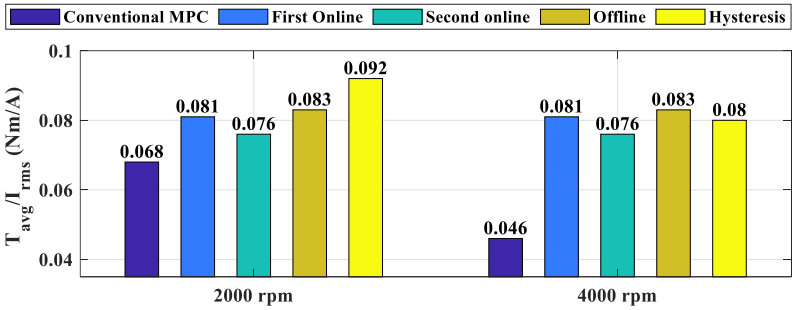

Figure 8.18: Comparison of torque per ampere ratio for SRM2 with indirect average torque control, conventional FCS-MPTC, and proposed methods.

To have a better comparative understanding of the performance of both conventional and predictive methods, the normalized performance of SRM2 is calculated for different control schemes at both 2000 and 4000 rpm. In this normalization, the method with the best performance gets the score of 1. Then, the scores for other methods are calculated considering how degraded their performance is compared to the best achieved performance. The calculation results are summarized in Table 8.4. It can be observed that the conventional FCS-MPTC has the worst performance in terms of copper losses, torque per ampere ratio and the percentage of torque ripple at 2000 rpm. The optimized hysteresis controller has the worst performance in terms of rms torque ripple. At 2000 rpm, the proposed offline method achieves the best performance in terms of both copper losses and percentage of torque ripple. The second proposed online method has the lowest rms

torque ripple compared to other methods. Note that the optimized hysteresis controller achieves the best performance in terms of average torque and torque per ampere ratio.

At 4000 rpm, the conventional FCS-MPTC has the worst performance in terms of average torque, copper losses, torque per ampere ratio, and torque ripple (both rms and percentage of torque ripple). The proposed offline method achieves the best performance in terms of torque per ampere ratio. The first online method has the lowest copper losses compared to other control strategies. The best performance in terms of average torque and torque ripple at 4000 rpm is achieved with the optimized hysteresis controller.

The online and offline computational burden of the conventional and proposed methods are also compared in Table 8.4. Both offline and optimized hysteresis controller require significant offline calculation burden for GA optimizations in the entire operating ranges. However, the offline computational burden is very low with the conventional FCS-MPTC and the proposed online methods. On the other hand, the proposed online methods have a higher online computational burden. The online computational burden is lower with both offline and conventional FCS-MPTC. The optimized hysteresis controller has the lowest online computational burden.

Table 8.4: Normalized performance comparison for SRM2 with the indirect average torque control, the conventional FCS-MPTC, and the proposed methods.

Performance parameters		T_{avg}	P_{cu}	T_{avg}/I_{rms}	T_{ripple} (%)	T_{ripple} (rms)	Online computational burden	Offline Computational burden
n_r=2000 rpm T_{ref}=3 Nm	Conventional FCS-MPTC	0.85	0.595	0.739	0.657	0.833	medium	low
	First online method	0.81	0.914	0.88	0.969	0.893	high	low
	Second online method	0.835	0.764	0.826	0.947	1	high	low
	Offline method	0.789	1	0.902	1	0.947	medium	high
	Optimized hysteresis	1	0.779	1	0.76	0.635	low	high
n_r=4000 rpm T_{ref}=3 Nm	Conventional FCS-MPTC	0.774	0.396	0.554	0.857	0.909	medium	low
	First online method	0.847	1	0.976	0.867	0.916	high	low
	Second online method	0.942	0.707	0.916	0.929	0.988	high	low
	Offline method	0.945	0.843	1	0.892	0.951	medium	high
	Optimized hysteresis	1	0.703	0.964	1	1	low	high

To compare the overall performance of the conventional FCS-MPTC, the proposed methods and the optimized hysteresis controller at 2000 rpm, the spider charts are plotted considering five different performance parameters as shown in Figure 8.19. It can be understood that the area for the conventional FCS-MPTC is significantly smaller than the other methods. In other words, it has a considerably degraded performance compared to the proposed methods. The optimized hysteresis controller has the worst performance in terms of torque ripple (both rms and the percentage of torque ripple) compared to the proposed predictive approaches, as it is not capable of shaping the phase current. However, it has the best performance in terms of average torque and torque per ampere ratio.

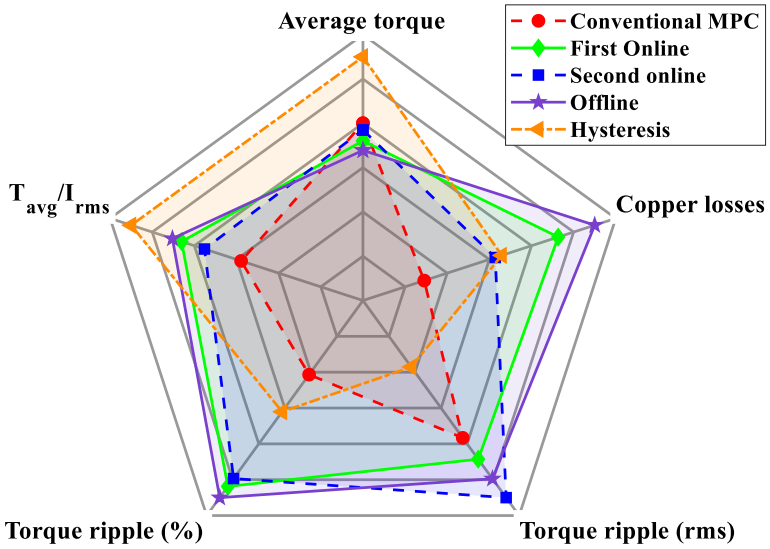

Figure 8.19: Overall performance comparison for SRM2 (2000 rpm) with indirect average torque control, conventional FCS-MPTC and proposed methods.

A similar spider chart is plotted in Figure 8.20 to compare the overall performance of different control methods at 4000 rpm. It can be observed that the conventional FCS-MPTC has the worst overall performance, hence the effectiveness of the proposed control schemes in adaptively controlling the commutation angles to improve the performance of SRM at higher speeds is validated. The second online method achieves the lowest torque ripple (both rms and the percentage of torque ripple) in comparison with other predictive approaches. The first online method has the lowest copper losses, however, it should be noticed that it achieves a lower average torque compared to the second online method, the offline method, and the optimized hysteresis controller. The optimized hysteresis controller has a slightly better performance in terms of torque ripple compared to the proposed predictive approaches.

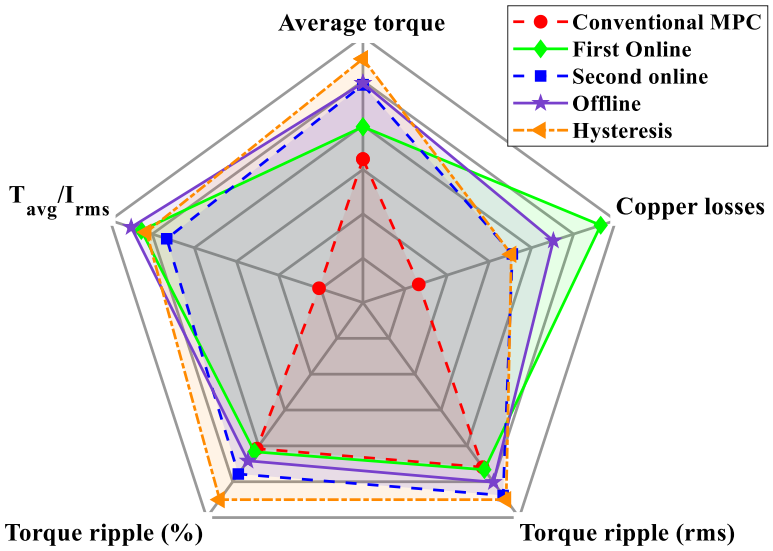

Figure 8.20: Overall performance comparison for SRM2 (4000 rpm) with indirect average torque control, conventional FCS-MPTC and proposed methods.

According to Figure 8.20, the optimized hysteresis controller achieves a higher average torque compared to the proposed predictive methods because of the steady state torque tracking error of FCS-MPTC, which is considered as one of its main shortcomings. The predictive approach needs to be further improved to achieve a minimized torque tracking error.

One of the main advantages of the proposed online methods over the optimization-based offline method is their robustness to parameter variations. Motor parameters can change over time for various reasons including aging, temperature, etc. resulting in a different optimal commutation angles for a specific operating point. Combining the proposed online methods with the online parameter estimation techniques can result in a more robust controller compared to the proposed offline predictive approach. The first online method has a lower online computational

burden compared to the second online method, as there is no need for prediction of the phase torque and calculation of the area under torque-time curve.

The proposed offline method also has a huge offline computational burden and it requires a larger memory space to store the optimal k_{MPC} and turn-off angle look up tables in the entire operating regions. On the other hand, the proposed offline method has a significantly lower online computation time compared to the proposed online methods.

As the optimal commutation angles are calculated using the GA optimization in the entire operating ranges in the offline method, it is expected to achieve a better overall performance with the proposed offline method compared to the online methods. However, due to the limited control frequency, the number of control points per electrical cycle is limited and this number reduces as speed increases. For this reason, it is not possible to apply the exact optimal turn-off angle in the experimental tests. For example, the electrical angle difference between the consecutive control points at 4000 rpm under 20 kHz is 9.6° electrical, hence, there might be a maximum error of 9.6° electrical in turning off the phase. This will affect the results obtained using a specific method. The effect of sampling is considerably lower at lower speeds. The effect of sampling is also higher at lower control frequencies. In other words, the difference between the proposed methods may not even be clearly distinguished if a very low control frequency is used. The stability

of the controller might even be affected if a very low control frequency is used at a high operating speed.

In this thesis, the online methods are implemented by calculating the optimal turn-off angle using simulations and implementing it using the look up tables of the optimal points. The maximum control frequency that can be achieved with the proposed offline method and using the sector partition technique is around 20 kHz, which is used in all the experimental results in this thesis. The computation time for the conventional FCS-MPTC without using the sector partition technique is much higher compared to the proposed methods. The measured online execution time for the conventional FCS-MPTC, the FCS-MPTC with sector partition technique and the optimized hysteresis controller are presented in Table 8.5.

Table 8.5: Comparison of online execution time for conventional and proposed FCS-MPTC, and optimized hysteresis controller

Method	Online execution time	Maximum achievable control frequency
Conventional FCS-MPTC	83 µs	12 kHz
Proposed FCS-MPTC	48 µs	20.8 kHz
Optimized hysteresis controller	30 µs	33.3 kHz

It can be observed from Table 8.5 that the real-time computation time is reduced around 42% using the sector partition technique. It needs to be mentioned that the maximum achievable frequency for the online methods will be lower than 20 kHz (if the optimality condition algorithm is executed online). Hence, the performance of the online methods will be degraded if the proposed current tail calculation

algorithm is executed in real-time. Moreover, the maximum control frequency with the conventional FCS-MPTC is around 12 kHz, which is not enough to control SRM2 at speeds higher than 3500 rpm. Note that, as mentioned earlier, the number of control points per electrical cycle reduces by increasing the speed. In this thesis, to have a fair comparison, the control frequency in the experimental results for all the methods (including online and conventional FCS-MPTC) is set to 20 kHz. In other words, the sector partition technique is also integrated with the conventional FCS-MPTC in all the experimental results to achieve the control frequency of 20 kHz. It means that the achieved overall performance with the conventional FCS-MPTC will be even more degraded if the sector partition technique is not integrated with it.

8.5 Summary

The simulations and experimental results of the indirect average torque control with optimized conduction angles, which is the mostly used conventional torque control method for SRM drives, are presented in this chapter. The simulation results of SRM1 are then quantitively compared to both conventional and proposed FCS-MPTC methods. It can be observed that the proposed methods can adaptively control the commutation angles in the entire speed range. It is concluded that the proposed methods have a better performance in terms of torque ripple and rms current compared to the conventional FCS-MPTC, especially in the high-speed

region. Comparing the performance of the conventional and predictive torque control methods under speed dynamics for SRM1 reveals the superior performance of the predictive control methods, especially in the low-speed region. At higher speeds, the proposed FCS-MPTC methods achieve lower torque ripple compared to the conventional FCS-MPTC by adaptively advancing the commutation angles, as the speed increases. The experimental results of the test SRM2 are compared for the conventional FCS-MPTC, the proposed methods and the optimized hysteresis controller. The optimized hysteresis controller has a higher torque ripple at low speed (2000 rpm) because of its incapability in shaping the phase currents. Furthermore, it is concluded that the proposed commutation angle control strategies achieve a lower negative phase torque, and consequently a considerably better overall performance compared to the conventional FCS-MPTC by adaptively advancing the commutation angles as speed increases.

Chapter 9

Steady State Torque Tracking Error Minimization of FCS-MPTC for SRM Drives

A new method to reduce the steady state torque tracking error of finite control set model predictive torque control for switched reluctance motor drives is proposed in this chapter. The steady state tracking error is considered as one of the main shortcomings of the conventional FCS-MPC. This can happen due to parameter uncertainties or when the multiple objectives are achieved by a single function with weighting factors. In the conventional model predictive torque control for SRM, the optimal switching state which minimizes a multi-objective cost function designed to track a reference torque while minimizing the phase currents over the prediction horizon is selected and applied at each switching instant, which results in the steady state torque tracking error. In this chapter, in order to minimize the torque tracking error, a compensation term is added to the reference torque at each sampling instant. The compensation term is calculated based on the estimated average torque tracking error in the previous sample times. Simulation results on a

three phase, 12/8, 2.3 kW SRM (SRM1) show promising results with the proposed method as compared to the conventional FCS-MPTC.

9.1 Proposed method

In majority of the predictive methods in the literature, weighting factors are often used to control several control objectives using a single objective function. Having several control objectives along with the torque tracking term in the objective function of FCS-MPTC can result in steady state torque tracking error, as it is impossible to achieve all the control objectives simultaneously. Any uncertainties in parameter estimations of the SRM can further increase the torque tracking error, which is considered as one of the main drawbacks of FCS-MPTC resulting in its degraded performance. An inductance auto-calibration algorithm to cope with measurement errors and parameter uncertainties is proposed in [19], [20] for model predictive current control of SRM drives. Several approaches have been proposed in the literature to increase the robustness of FCS-MPC towards parameter variations for predictive current, speed and torque control of IM and PMSM drives. Active disturbance rejection-based MPTC is proposed in [87] to alleviate the torque prediction error resulting from parameter mismatch for induction machines. A novel current update mechanism is proposed in [88] to reduce the sensitivity of FCS-MPC to parameter variations for current control of SPMSM drives.

The main contribution of this chapter is proposing a method to reduce the torque tracking error of the FCS-MPTC for torque control of SRM drives. In the proposed method, the reference torque is compensated at each sample time using a compensation term which is calculated considering the estimated average torque error in the previous sample times. The effectiveness of the proposed method in alleviating the torque tracking error of FCS-MPTC for SRM drives is demonstrated through simulations.

Using the weighting factor (k_{MPC}) in the objective function of FCS-MPTC, given in equation (4.9), is necessary to achieve a smooth phase current waveform, however, it results in the steady state torque tracking error. The variation of torque tracking error versus k_{MPC} for the test SRM1 at three different speeds and under constant load torque of 3 Nm is presented in Figure 9.1. The tracking error is bigger as k_{MPC} increases. In addition, operating at higher speeds results in a more degraded performance with bigger tracking error.

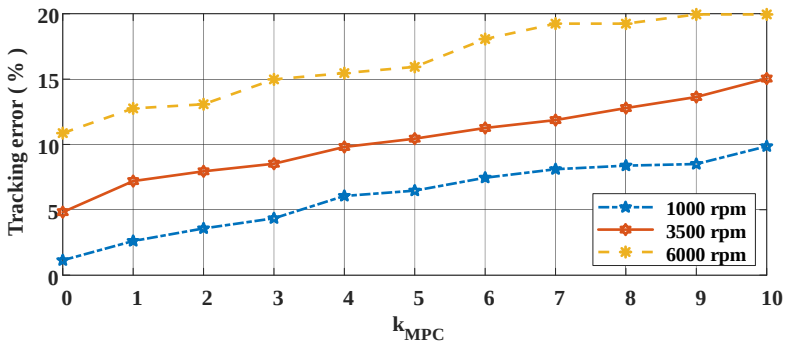

Figure 9.1: Variation of torque tracking error versus k_{MPC} under load torque of 3 Nm for SRM1.

In the conventional single-step FCS-MPTC, the optimal switching state at each sample time is decided based on the predicted performance of SRM in one future time step using the instantaneous position and current feedbacks at that sample time. To reduce the tracking error with FCS-MPTC, a method is proposed in this chapter by adding a compensation term to the desired reference torque at each sample time by calculating the estimated average torque tracking error in the previous sample times. Assuming a desired average reference torque of T_{ref}, calculating the arithmetic mean of the (N+1) torque points, including the estimated torque values at N previous sample times and the reference torque at time instant (k) (T^*_{ref}) yields:

$$T_{ref} = \frac{\sum_{i=1}^{N} T_i + T_{ref}^*}{N+1} \tag{9.1}$$

where $\sum_{i=1}^{N} T_i$ is the sum of estimated average torque values in N previous sample times. Rearranging equation (9.1) results in

$$T_{ref}^* = T_{ref} + \left(NT_{ref} - \sum_{i=1}^{N} T_i \right) \tag{9.2}$$

where the term $\left(NT_{ref} - \sum_{i=1}^{N} T_i\right)$ is the accumulative torque tracking error over N previous sample times. By assuming a very large N ($N \to \infty$),

$$T_{ref}^* = T_{ref} + \sum_{i=1}^{\infty} E_{T,i} \tag{9.3}$$

where $\sum_{i=1}^{\infty} E_{T,i}$ is the accumulative torque tracking error over time. Hence, the reference torque at time instant (k) (T^*_{ref}) can be determined by adding the accumulative torque tracking error in the previous sample times as the compensation term to the desired average reference torque (T_{ref}).

9.2 Simulation results

The simulation results on the test SRM1 are presented in this section to show the effectiveness of the proposed method in reducing the torque tracking error of FCS-MPTC for SRM drives. The simulation results with and without the proposed method are provided for comparison purposes. Note that the adaptive commutation angle control method to minimize the toque ripple proposed in [32] (first proposed online method) is adopted in all the simulations of FCS-MPTC in this chapter. The maximum switching frequency is limited to 20 kHz in the simulations, however, the average switching frequency will be lower. Figure 9.2 shows the simulations results for SRM1 at 2000 rpm under reference torque steps (1 to 5 Nm with the steps of 1 Nm) without the proposed torque tracking error minimization algorithm.

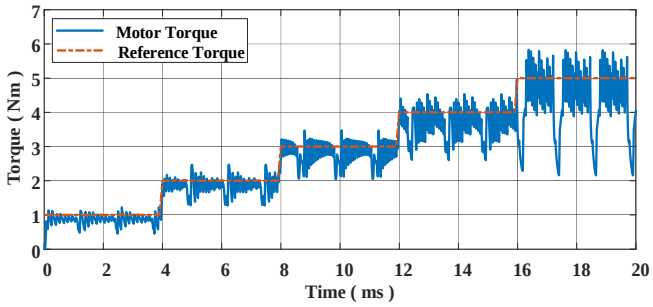

(a)

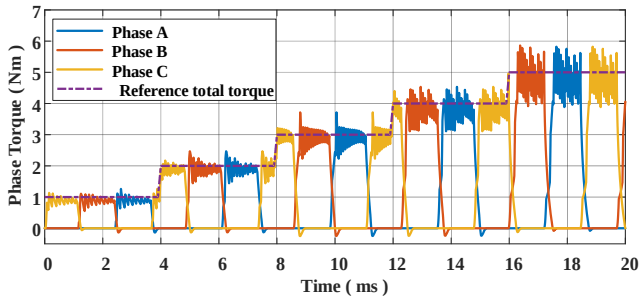

(b)

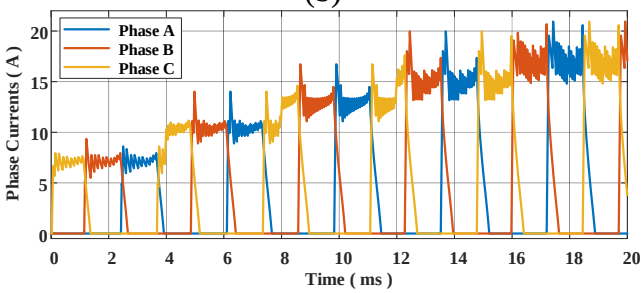

(c)

Figure 9.2: Simulation results of the FCS-MPTC without proposed method for SRM1 at 2000 rpm under torque step commands; (a) total torque, (b) phase torques, and (c) phase currents.

It can be observed from Figure 9.2-a that the average torque seems to be slightly lower than the desired reference torque in all the toque levels. Besides, the tracking error is bigger at higher reference torques. Furthermore, the torque ripple increases by increasing the reference torque as can be seen from both Figure 9.2-a and Figure 9.2-b. The simulation results for SRM1 at 2000 rpm and under similar torque step commands are depicted in Figure 9.3.

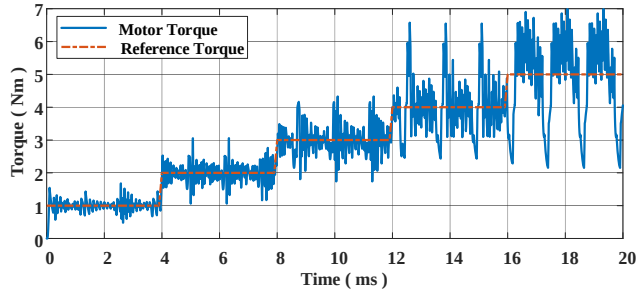

(a)

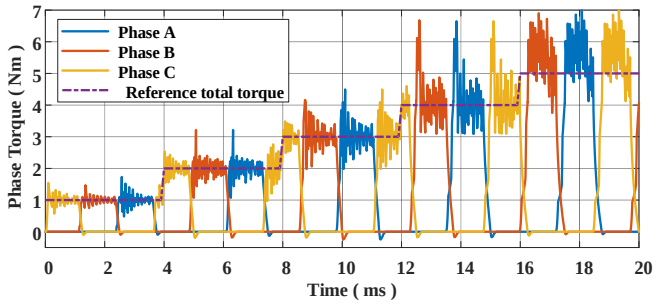

(b)

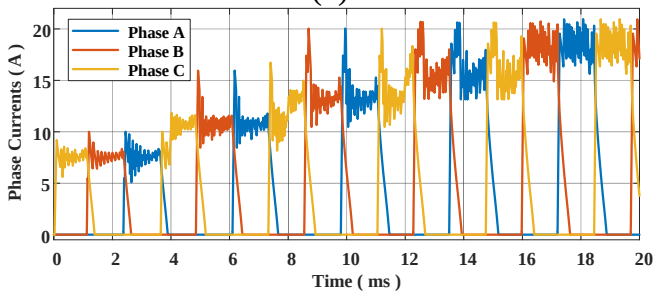

(c)

Figure 9.3: Simulation results of the FCS-MPTC with proposed method for SRM1 at 2000 rpm under torque step commands; (a) total torque, (b) phase torques, and (c) phase currents.

By comparing Figure 9.3-a with Figure 9.2-a, the increase in the average torque and hence a better torque tracking is observed with the proposed method. However, torque ripple seems to be higher with the proposed method. Both torque tracking error and rms torque ripple are calculated for different torque levels at 2000 rpm with and without applying the proposed method. The results are presented in Figure 9.4-a and Figure 9.4-b respectively.

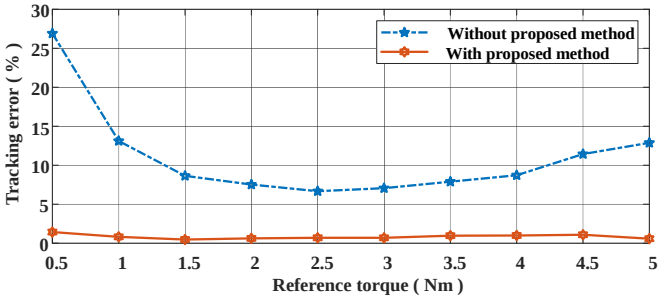

(a)

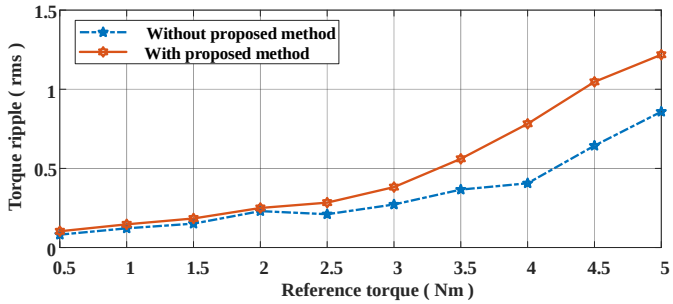

(b)

Figure 9.4: Variation of torque tracking error and rms torque ripple versus reference torque for SRM1 at 2000 rpm with and without using the proposed method; (a) torque tracking error, and (b) rms torque ripple.

It can be observed from Figure 9.4-a that the torque tracking error is significantly reduced using the proposed method. The tracking error remains below 1.4% in the entire torque range at 2000 rpm. The minimum and maximum improvement in tracking error is around 6% and 25.5% respectively. It can be observed from Figure 9.4-b that torque ripple increases with the proposed method. The increase in torque ripple is small at lower reference torques, however, it gets bigger as reference torque increases. A slight increase in torque ripple with the proposed method is expected as SRM delivers higher torque using the proposed method. It can be seen from Figure 9.4-b that torque ripple increases by increasing the load torque. Another reason for increase in torque ripple with the proposed method is updating the reference torque at each sample time. Note that the reference torque remains constant in the conventional FCS-MPTC.

To investigate the performance of the proposed method at higher speeds, the simulation results of the test SRM1 at 6000 rpm (base-speed) under reference

torque step commands (1 to 3 Nm with the steps of 1 Nm) without using the proposed method are presented in Figure 9.5.

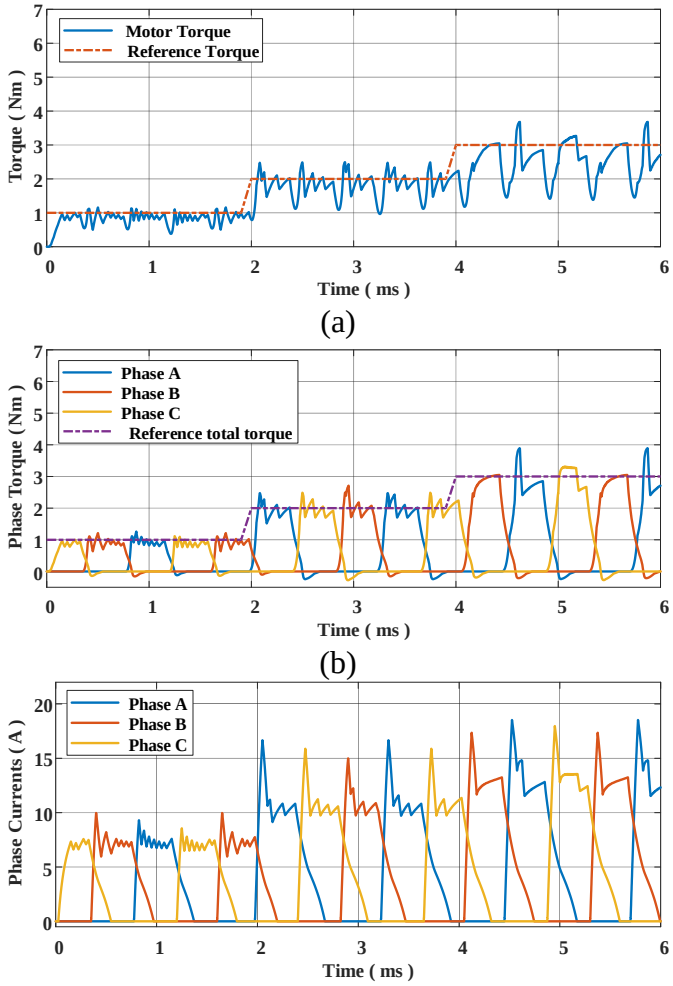

Figure 9.5: Simulation results of the FCS-MPTC without proposed method for SRM1 at 6000 rpm under torque step commands; (a) total torque, (b) phase torques, and (c) phase currents.

Similar to the results at 2000 rpm, the average torque seems to be lower than the reference torque specially under 3 Nm as can be seen from Figure 9.5-a. The simulation results with the proposed method are presented in Figure 9.6.

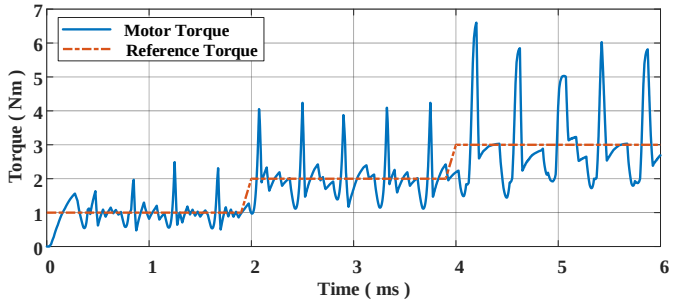

(a)

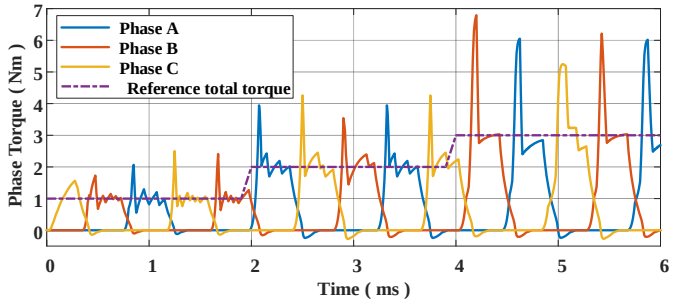

(b)

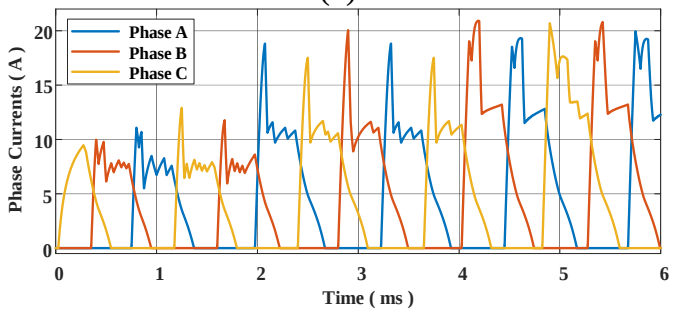

(c)

Figure 9.6: Simulation results of the FCS-MPTC without proposed method for SRM1 at 6000 rpm under torque step commands; (a) total torque, (b) phase torques, and (c) phase currents.

Comparing Figure 9.6-a and Figure 9.5-a reveals that the average torque increases with the proposed method. However, the torque ripples are bigger as can be observed by comparing Figure 9.6-a and Figure 9.6-b with Figure 9.5-a and Figure 9.5-b. Furthermore, the rms phase currents seem to be bigger with the proposed method as can be understood by comparing Figure 9.6-c and Figure 9.5-c which is expected as a higher average torque is achieved with the proposed method.

The variation of both torque tracking error and rms torque ripple versus load torque for SRM1 at 6000 rpm with and without using the proposed method are shown in Figure 9.7-a and Figure 9.7-b respectively.

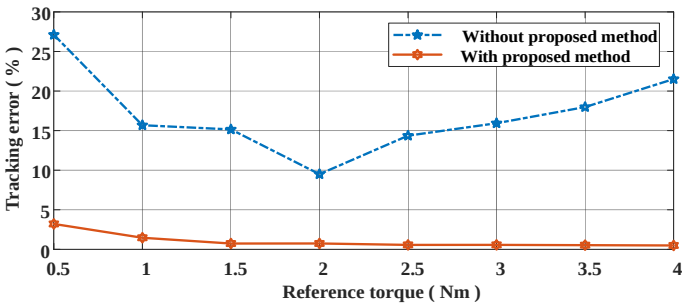

(a)

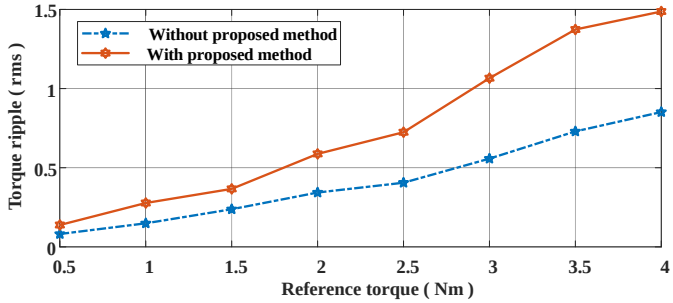

(b)

Figure 9.7: Variation of torque tracking error and rms torque ripple versus reference torque for SRM1 at 6000 rpm with and without using the proposed method; (a) torque tracking error, and (b) rms torque ripple.

The significant improvement in tracking error is observed from Figure 9.7-a in which the tracking error remains below 3.2% in the entire torque range. The minimum and maximum improvement in the torque tracking error is around 8.8% and 23.9% respectively. Similar to the results at 2000 rpm, the torque ripple is higher with the proposed method as shown in Figure 9.7-b. Part of this increase in torque ripple is due to achieving a higher average torque and updating the reference torque at each sample time as mentioned earlier. Note that achieving a higher

average torque with SRM is more challenging at higher speeds due to increased back-emf which makes it difficult to inject the current. The proposed method needs to be further improved to achieve a better performance in terms of torque ripple while maintaining the advantage of having a lower torque tracking error.

9.3 Summary

In this chapter, a method is proposed to minimize the steady state torque tracking error of FCS-MPTC for SRM drives. The torque tracking error stemming from either parameter uncertainties or achieving several performance objectives using a single objective function with weighting factors is considered as one of the main drawbacks of conventional FCS-MPTC. In this chapter, a compensation term which is calculated based on the estimated average torque error at consecutive sample times is added to the reference torque at each sample time. The effectiveness of the proposed algorithm is verified by simulations on a 3-phase, 2.3 kW, 12/8 SRM (SRM1). Simulation results at 2000 rpm and 6000 rpm (base-speed) reveal that the torque tracking error is significantly reduced using the proposed method. The torque tracking error remains below 1.4% and 3.2% in the entire torque range at 2000 rpm and 6000 rpm, respectively. The torque ripple is expectedly higher with the proposed method, as a higher average torque is achieved, and the reference torque is updated at each sample time. The performance of the proposed method

needs to be further improved to reduce torque ripples while maintaining the minimum tracking error.

Chapter 10

Conclusions and Future Work

10.1 Conclusions

The main contribution of this thesis is proposing two online methods and one optimization-based offline method to adaptively control the turn-on and turn-off angles with the FCS-MPTC for SRM drives to extend the operating speed range of the conventional FCS-MPTC. Furthermore, the real-time computational burden of the conventional FCS-MPTC is significantly reduced using the sector partition technique. Finally, a method is proposed to alleviate the steady state torque tracking error of FCS-MPTC for SRM drives.

After demonstrating the incapability of the conventional FCS-MPTC in controlling the commutation angles through simulations, the necessity of adaptively controlling the commutation angles to extend the operating speed range of the conventional FCS-MPTC is clarified. It is concluded that there exists an optimal turn-off angle

at each reference speed and reference torque to achieve an optimal performance in terms of torque ripple, average torque, rms current and efficiency.

The proposed first online method can successfully advance the commutation angles as the speed increases to minimize the phase negative torque. Significant reduction of the phase negative torque at higher speeds is achieved with the first proposed online method. Besides, the average torque is considerably increased compared to conventional FCS-MPTC for a constant reference torque at base-speed. The performance of the first proposed online method is further improved by modifying the defined optimality condition, and hence, the second online method is proposed. This method achieves an improved performance compared to the first online method by allowing a slightly larger phase negative torque. However, the second online method has a higher online computational burden compared to the first proposed online method. Hence, the issue of the large phase current peak close to the unaligned position is resolved and the higher torque production capability of the SRM close to the aligned position is better utilized. Both proposed online methods are validated with simulations and experimental results. The real time computational burden of the conventional FCS-MPTC is also considerably reduced using the sector partition technique.

To determine the globally optimal phase turn-off angle and the weighting factor for the objective function of FCS-MPTC, an offline multi-objective optimization-based method is proposed to adaptively control the phase commutation angles in

the entire operating range. After analyzing the pareto front of the optimization results, an optimal solution to the optimization problem is selected. Simulations and experimental results of the optimal solution at both low-speed and high-speed reveal the significant improvements in terms of phase negative torque, average torque, phase rms current, and torque ripple, especially at higher speeds.

The performance characteristics of the three proposed commutation angle control methods are comprehensively compared in terms of commutation angles, offline and online computational burden, average torque, rms current, and torque ripple using simulations and experimental results. Furthermore, the performance of the proposed methods is compared to the conventional FCS-MPTC, ITC with optimized conduction angles and TSF.

Finally, a method is proposed to mitigate the steady state torque tracking error of FCS-MPTC resulting from parameter uncertainties or achieving several performance objectives with a single objective function with weighting factors. Simulation results demonstrates the effectiveness of the proposed method in minimizing the torque tracking error in the entire speed and torque ranges.

10.2 **Future work**

In this thesis, the proposed online methods are experimentally validated by generating the look up tables of the optimal turn-off angles in simulations and using these look up tables for experimental implementation. Real-time calculation of the

current tail and torque-time area with both first and second online methods will add more value to the experimental results.

In this thesis, the experimental results are carried out at the maximum achievable control frequency (20 kHz). Analyzing the effects of implementing FCS-MPTC at a lower control frequency on the performance of the conventional and proposed methods can be considered as a future work.

Although, in this thesis, the performance of the proposed methods is evaluated on 2.3 kW and 5.5 kW switched reluctance motors, the proposed methods can also be implemented in high power applications including transportation electrification. Analyzing and investigating the performance of the proposed methods on a high-power SRM to investigate the capability of the methods and possible challenges can be considered as another future work.

The weighting factor of the FCS-MPTC (k_{MPC}) is kept constant in the proposed online methods. In the offline method, it is shown that k_{MPC} needs to be changed to achieve the optimized performance at different operating points. This weighting factor can also be optimized with the proposed online methods to adaptively change to achieve the improved performance in the entire operating ranges.

Efficiency is an important performance parameter that can be evaluated and compared for the proposed methods. However, it needs the measurement of the core losses of SRM which is challenging. Calculation and comparison of the

efficiency for the conventional and proposed methods can be considered as a future work.

It might be possible to quantify the amount of the phase negative torque (the negative area under torque-time curve) to investigate the variation of the performance parameters (torque ripple, rms current, etc.) with respect to the quantified phase negative torque.

Although the steady state torque tracking error is reduced with the method proposed in chapter 9, torque ripple is slightly increased especially at higher reference torque levels. The proposed method can be modified to achieve a minimized steady state tracking error with a reduced torque ripple.

Variation of the weighting factor of FCS-MPTC can significantly affect the performance of the predictive control and its tuning is an exhausting task. It might be possible to eliminate the weighting factor by adopting and improving the hierarchical predictive control schemes proposed in [89]–[92].

In both of the proposed online methods in this thesis, the optimality condition is defined by predicting the phase current in an extended time interval, much bigger than the prediction horizon of FCS-MPTC. It might be possible to achieve an optimal performance by embedding the desired optimality condition in the objective function of FCS-MPTC. This can significantly reduce the real-time computational burden of the proposed online methods.

The minimization of the average switching frequency of the FCS-MPTC can also be considered by adding a corresponding term to the objective function of FCS-MPTC to minimize the number of switchings of the inverter switches.

Variable switching frequency is one the main drawbacks of the conventional FCS-MPC. A fixed switching frequency predictive control with improved performance can be achieved by integrating duty cycle control with FCS-MPC [93], [94].

The performance of FCS-MPC is largely dependent on model accuracy. It might be possible to improve the robustness of the predictive torque control and reduce its dependence on parameter accuracy by integrating FCS-MPTC with online parameter estimation techniques.

10.3 Publications

10.3.1 Journal papers

1. Diego F. Valencia, **Rasul Tarvirdilu-Asl**, Cristian Garcia, Jose Rodriguez and Ali Emadi. "A Review of Predictive Control Techniques for Switched Reluctance Machine Drives. Part I: Fundamentals and Current Control." *IEEE Transactions on Energy Conversion* (Accepted).
2. Diego F. Valencia, **Rasul Tarvirdilu-Asl**, Cristian Garcia, Jose Rodriguez and Ali Emadi. "A Review of Predictive Control Techniques for Switched

Reluctance Machine Drives. Part II: Torque Control, Assessment and Challenges." *IEEE Transactions on Energy Conversion* (Accepted).

3. Diego F. Valencia, **Rasul Tarvirdilu-Asl**, Cristian Garcia, Jose Rodriguez and Ali Emadi. "Vision, Challenges and Future Trends of Model Predictive Control in Switched Reluctance Drives." Ready to be *Submitted.*
4. **Rasul Tarvirdilu-Asl**, Shamsuddeen Nalakath, Zekun Xia, Yingguang Sun, Jason Wiseman, and Ali Emadi. "Improved Online Optimization-Based Optimal Tracking Control Method for Induction Motor Drives." *IEEE Transactions on Power Electronics 35, no. 10 (2020): 10654-10672.*
5. Xia, Zekun, Shamsuddeen Nalakath, **Rasul Tarvirdilu-Asl**, Yingguang Sun, Jason Wiseman, and Ali Emadi. "Online Optimal Tracking Method for Interior Permanent Magnet Machines with Improved MTPA and MTPV in Whole Speed and Torque Ranges." *IEEE Transactions on Power Electronics 35, no. 9 (2020): 9755-9771.*
6. **Rasul Tarvirdilu-Asl**, Silvio Rotilli Filho, Zekun Xia, Yingguang Sun, Jason Wiseman, and Ali Emadi. "A New Online Calculation Method for Maximum Torque per Ampere Tracking Control of Induction Motor Drives Considering Core Losses." *IEEE Open Journal of Industry Applications* (Under review).
7. **Rasul Tarvirdilu-Asl**, Shamsuddeen Nalakath, Diego F. Valencia, Berker Bilgin, and Ali Emadi. "Finite Control Set Model Predictive Control for

Switched Reluctance Motor Drives with Reduced Torque Tracking Error." (In preparation).

8. **Rasul Tarvirdilu-Asl**, Shamsuddeen Nalakath, Diego F. Valencia, Berker Bilgin, and Ali Emadi. "Offline Multi-Objective Optimization-Based Commutation Angle Control for Finite Control Set Model Predictive Torque Control of SRM Drives." (In preparation).
9. **Rasul Tarvirdilu-Asl**, Shamsuddeen Nalakath, Diego F. Valencia, Berker Bilgin, and Ali Emadi. "Extended-Speed Online Commutation Angle Control for Finite Control Set Model Predictive Torque Control of SRM Drives." (In preparation).
10. **Rasul Tarvirdilu-Asl**, Silvio Rotilli Filho, Zekun Xia, Yingguang Sun, Jason Wiseman, and Ali Emadi. "A New Online Optimization-Based Maximum Efficiency Tracking Control for Induction Motor Drives Considering Core Losses." *IEEE Transactions on Power Electronics* (To be submitted).

10.3.2 Conference papers

1. **Rasul Tarvirdilu-Asl**, Shamsuddeen Nalakath, Berker Bilgin, and Ali Emadi. "A Finite Control Set Model Predictive Torque Control for Switched Reluctance Motor Drives with Adaptive Turn-off Angle."

In *IECON 2019-45th Annual Conference of the IEEE Industrial Electronics Society*, vol. 1, pp. 840-845. IEEE, 2019.

2. **Rasul Tarvirdilu-Asl**, Shamsuddeen Nalakath, Yingguang Sun, Jason Wiseman, and Ali Emadi. "Optimal Control of Induction Motor in Field Weakening Region Considering Inverter Nonlinearity." In *2019 IEEE Transportation Electrification Conference and Expo (ITEC)*, pp. 1-8. IEEE, 2019.
3. **Rasul Tarvirdilu-Asl**, and Jennifer Bauman. "Efficiency Analysis of Induction Motor Control Strategies Using a System-Level EV Model." In *2019 IEEE Transportation Electrification Conference and Expo (ITEC)*, pp. 1-6. IEEE, 2019.
4. **Rasul Tarvirdilu-Asl**, and Mehdi Narimani. "A new nine-level voltage source inverter with capacitor voltage balancing." In *IECON 2018-44th Annual Conference of the IEEE Industrial Electronics Society*, pp. 907-912. IEEE, 2018.

References

[1] B. Bilgin *et al.*, "Making The Case for Switched Reluctance Motors for Propulsion Applications," *IEEE Trans. Veh. Technol.*, pp. 1–1, May 2020.

[2] J.-W. Ahn and G. F. Lukman, "Switched reluctance motor: Research trends and overview," *CES Trans. Electr. Mach. Syst.*, vol. 2, no. 4, pp. 339–347, 2018.

[3] T. Husain, A. Elrayyah, Y. Sozer, and I. Husain, "Unified Control for Switched Reluctance Motors for Wide Speed Operation," *IEEE Trans. Ind. Electron.*, vol. 66, no. 5, pp. 3401–3411, 2019.

[4] A. Emadi, *Advanced electric drive vehicles*. CRC Press, 2014.

[5] S. J. Evangeline and S. S. Kumar, "Minimization of Torque Ripple in Switched Reluctance Motor Drive–A Review," in *Advanced Electrical and Electronics Engineering*, Springer, 2011, pp. 287–294.

[6] R. T. Asl, "Optimum Pole Combination to Maxmize Torque Density in Switched Reluctance Motors for Electric Vehicle Applications." Middle East Technical University, 2016.

[7] J. W. Jiang, B. Bilgin, and A. Emadi, "Three-phase 24/16 switched reluctance machine for a hybrid electric powertrain," *IEEE Trans. Transp.*

Electrif., vol. 3, no. 1, pp. 76–85, 2017.

[8] S. M. Castano, B. Bilgin, E. Fairall, and A. Emadi, "Acoustic noise analysis of a high-speed high-power switched reluctance machine: Frame effects," *IEEE Trans. Energy Convers.*, vol. 31, no. 1, pp. 69–77, 2015.

[9] A. D. Callegaro, B. Bilgin, and A. Emadi, "Radial force shaping for acoustic noise reduction in switched reluctance machines," *IEEE Trans. Power Electron.*, vol. 34, no. 10, pp. 9866–9878, 2019.

[10] A. D. Callegaro, J. Liang, J. W. Jiang, B. Bilgin, and A. Emadi, "Radial force density analysis of switched reluctance machines: the source of acoustic noise," *IEEE Trans. Transp. Electrif.*, vol. 5, no. 1, pp. 93–106, 2018.

[11] J. Dong *et al.*, "Hybrid acoustic noise analysis approach of conventional and mutually coupled switched reluctance motors," *IEEE Trans. Energy Convers.*, vol. 32, no. 3, pp. 1042–1051, 2017.

[12] J. Liang *et al.*, "Prediction of acoustic noise and vibration of a 24/16 traction switched reluctance machine," *IET Electr. Syst. Transp.*, vol. 10, no. 1, pp. 35–43, 2019.

[13] A. Dorneles Callegaro, "Radial Force Shaping of Switched Reluctance Motor Drives for Acoustic Noise Reduction." 2018.

[14] J. Ye, "Advanced control methods for torque ripple reduction and

performance improvement in switched reluctance motor drives." 2014.

[15] Y. Sozer, I. Husain, and D. A. Torrey, "Guidance in Selecting Advanced Control Techniques for Switched Reluctance Machine Drives in Emerging Applications," *IEEE Trans. Ind. Appl.*, vol. 51, no. 6, pp. 4505–4514, Nov. 2015.

[16] N. Yan, X. Cao, and Z. Deng, "Direct Torque Control for Switched Reluctance Motor to Obtain High Torque–Ampere Ratio," *IEEE Trans. Ind. Electron.*, vol. 66, no. 7, pp. 5144–5152, 2019.

[17] C. R. Neuhaus, N. H. Fuengwarodsakul, and R. W. De Doncker, "Predictive PWM-based direct instantaneous torque control of switched reluctance drives," in *2006 37th IEEE Power Electronics Specialists Conference*, 2006, pp. 1–7.

[18] C. Li, G. Wang, Y. Li, and A. Xu, "An improved finite-state predictive torque control for switched reluctance motor drive," *IET Electr. Power Appl.*, vol. 12, no. 1, pp. 144–151, 2017.

[19] X. Li and P. Shamsi, "Model predictive current control of switched reluctance motors with inductance auto-calibration," *IEEE Trans. Ind. Electron.*, vol. 63, no. 6, pp. 3934–3941, 2016.

[20] X. Li and P. Shamsi, "Inductance surface learning for model predictive

current control of switched reluctance motors," *IEEE Trans. Transp. Electrif.*, vol. 1, no. 3, pp. 287–297, 2015.

[21] H. Peyrl, G. Papafotiou, and M. Morari, "Model predictive torque control of a switched reluctance motor," in *2009 IEEE International Conference on Industrial Technology*, 2009, pp. 1–6.

[22] R. Mikail, I. Husain, Y. Sozer, M. S. Islam, and T. Sebastian, "Torque-ripple minimization of switched reluctance machines through current profiling," *IEEE Trans. Ind. Appl.*, vol. 49, no. 3, pp. 1258–1267, 2013.

[23] J. Ye, B. Bilgin, and A. Emadi, "An Offline Torque Sharing Function for Torque Ripple Reduction in Switched Reluctance Motor Drives," *IEEE Trans. Energy Convers.*, vol. 30, no. 2, pp. 726–735, Jun. 2015.

[24] J. Ye, B. Bilgin, and A. Emadi, "An extended-speed low-ripple torque control of switched reluctance motor drives," *IEEE Trans. Power Electron.*, vol. 30, no. 3, pp. 1457–1470, 2015.

[25] X. D. Xue, K. W. E. Cheng, and S. L. Ho, "Optimization and evaluation of torque-sharing functions for torque ripple minimization in switched reluctance motor drives," *IEEE Trans. power Electron.*, vol. 24, no. 9, pp. 2076–2090, 2009.

[26] H. Li, B. Bilgin, and A. Emadi, "An Improved Torque Sharing Function for

Torque Ripple Reduction in Switched Reluctance Machines," *IEEE Trans. Power Electron.*, vol. 34, no. 2, pp. 1635–1644, 2019.

[27] S. Bolognani, S. Bolognani, L. Peretti, and M. Zigliotto, "Design and implementation of model predictive control for electrical motor drives," *IEEE Trans. Ind. Electron.*, vol. 56, no. 6, pp. 1925–1936, 2008.

[28] I. Osman, D. Xiao, K. S. Alam, M. P. Akter, S. M. S. I. Shakib, and M. F. Rahman, "Discrete Space Vector Modulation Based Model Predictive Torque Control with No Sub-Optimization," *IEEE Trans. Ind. Electron.*, 2019.

[29] S. S. Ahmad and G. Narayanan, "Predictive control based constant current injection scheme for characterization of switched reluctance machine," *IEEE Trans. Ind. Appl.*, vol. 54, no. 4, pp. 3383–3392, 2018.

[30] R. Mikail, I. Husain, Y. Sozer, M. S. Islam, and T. Sebastian, "A fixed switching frequency predictive current control method for switched reluctance machines," *IEEE Trans. Ind. Appl.*, vol. 50, no. 6, pp. 3717–3726, 2014.

[31] A. Anuchin, V. Podzorova, V. Popova, I. Gulyaev, F. Briz, and Y. Vagapov, "Model Predictive Torque Control of a Switched Reluctance Drive with Heat Dissipation Balancing in a Power Converter," in *2019 IEEE 60th*

International Scientific Conference on Power and Electrical Engineering of Riga Technical University (RTUCON), 2019, pp. 1–6.

[32] R. Tarvirdilu-Asl, S. Nalakath, B. Bilgin, and A. Emadi, "A Finite Control Set Model Predictive Torque Control for Switched Reluctance Motor Drives with Adaptive Turn-off Angle," in *IECON 2019-45th Annual Conference of the IEEE Industrial Electronics Society*, 2019, vol. 1, pp. 840–845.

[33] J. Villegas, S. Vazquez, J. M. Carrasco, and I. Gil, "Model predictive control of a switched reluctance machine using discrete space vector modulation," in *2010 IEEE International Symposium on Industrial Electronics*, 2010, pp. 3139–3144.

[34] S. Song, R. Hei, R. Ma, and W. Liu, "Model Predictive Control of Switched Reluctance Starter/Generator with Torque Sharing and Compensation," *IEEE Trans. Transp. Electrif.*, 2020.

[35] Y. Li, R. Wang, G. Wang, C. Li, Y. Fan, and J. Liu, "Predictive Direct Torque Control for Switched Reluctance Motor Drive System," in *2018 37th Chinese Control Conference (CCC)*, 2018, pp. 3871–3876.

[36] H. Hu, X. Cao, N. Yan, and Z. Deng, "A New Predictive Torque Control Based Torque Sharing Function for Switched Reluctance Motors," in *2019 22nd International Conference on Electrical Machines and Systems*

(ICEMS), 2019, pp. 1–5.

[37] C. Shang, A. Xu, L. Huang, and J. Chen, "Flux linkage optimization for direct torque control of switched reluctance motor based on model predictive control," *IEEJ Trans. Electr. Electron. Eng.*, vol. 14, no. 7, pp. 1105–1113, 2019.

[38] A. Xu, C. Shang, J. Chen, J. Zhu, and L. Han, "A new control method based on DTC and MPC to reduce torque ripple in SRM," *IEEE Access*, vol. 7, pp. 68584–68593, 2019.

[39] J. Ye, P. Malysz, and A. Emadi, "A fixed-switching-frequency integral sliding mode current controller for switched reluctance motor drives," *IEEE J. Emerg. Sel. Top. Power Electron.*, vol. 3, no. 2, pp. 381–394, 2014.

[40] F. Peng, J. Ye, and A. Emadi, "A digital PWM current controller for switched reluctance motor drives," *IEEE Trans. Power Electron.*, vol. 31, no. 10, pp. 7087–7098, 2015.

[41] Q. Yu, B. Bilgin, and A. Emadi, "Loss and efficiency analysis of switched reluctance machines using a new calculation method," *IEEE Trans. Ind. Electron.*, vol. 62, no. 5, pp. 3072–3080, 2015.

[42] M. Ehsani, Y. Gao, S. Longo, and K. Ebrahimi, *Modern electric, hybrid electric, and fuel cell vehicles*. CRC press, 2018.

[43] M. Krishnamurthy, C. S. Edrington, A. Emadi, P. Asadi, M. Ehsani, and B. Fahimi, "Making the case for applications of switched reluctance motor technology in automotive products," *IEEE Trans. power Electron.*, vol. 21, no. 3, pp. 659–675, 2006.

[44] B. Bilgin, J. W. Jiang, and A. Emadi, *Switched reluctance motor drives: fundamentals to applications*. CRC Press, 2019.

[45] W. Jiang, "Three-phase 24/16 switched reluctance machine for hybrid electric powertrains: Design and optimization." 2016.

[46] H. Li, "Torque Ripple Minimization in Switched Reluctance Machines." 2017.

[47] A. V Rajarathnam, K. M. Rahman, and M. Ehsani, "Improvement of hysteresis control in switched reluctance motor drives," in *IEEE International Electric Machines and Drives Conference. IEMDC'99. Proceedings (Cat. No. 99EX272)*, 1999, pp. 537–539.

[48] C. Labiod, K. Srairi, B. Mahdad, M. T. Benchouia, and M. E. H. Benbouzid, "Speed control of 8/6 switched reluctance motor with torque ripple reduction taking into account magnetic saturation effects," *Energy Procedia*, vol. 74, no. 1, pp. 112–121, 2015.

[49] X. Rain, M. Hilairet, and O. Bethoux, "Comparative study of various current

controllers for the switched reluctance machine," in *2010 IEEE Vehicle Power and Propulsion Conference*, 2010, pp. 1–6.

[50] B. C. Torrico, R. N. de C. Almeida, L. L. N. dos Reis, W. A. Silva, and R. S. T. Pontes, "Robust Control Based on Generalized Predictive Control Applied to Switched Reluctance Motor Current Loop," *J. Dyn. Syst. Meas. Control*, vol. 136, no. 3, 2014.

[51] S. Mehta, M. A. Kabir, and I. Husain, "Extended Speed Current Profiling Algorithm for Low Torque Ripple SRM Using Model Predictive Control," in *2018 IEEE Energy Conversion Congress and Exposition, ECCE 2018*, 2018, pp. 4558–4563.

[52] S. Mehta, P. Pramod, and I. Husain, "Analysis of Dynamic Current Control Techniques for Switched Reluctance Motor Drives for High Performance Applications," in *ITEC 2019 - 2019 IEEE Transportation Electrification Conference and Expo*, 2019.

[53] X. Zhang, Q. Yang, M. Ma, Z. Lin, and S. Yang, "A Switched Reluctance Motor Torque Ripple Reduction Strategy With Deadbeat Current Control and Active Thermal Management," *IEEE Trans. Veh. Technol.*, vol. 69, no. 1, pp. 317–327, Jan. 2020.

[54] S. Mehta, I. Husain, and P. Pramod, "Predictive Current Control of Mutually

Coupled Switched Reluctance Motors Using Net Flux Method," in *2019 IEEE Energy Conversion Congress and Exposition, ECCE 2019*, 2019, pp. 4918–4922.

[55] M. Kiani, "Model predictive control of stator currents in Switched Reluctance Generators," in *2014 IEEE 23rd International Symposium on Industrial Electronics (ISIE)*, 2014, pp. 842–846.

[56] R. Pupadubsin, P. Somsiri, N. Chayopitak, K. Tungpimolrut, P. Jitkreeyan, and S. Kachapornkul, "Simple predictive delta-modulation current regulator for switched reluctance motor drive," in *2008 International Conference on Electrical Machines and Systems*, 2008, pp. 3333–3337.

[57] B. Li, X. Ling, Y. Huang, L. Gong, and C. Liu, "Predictive current control of a switched reluctance machine in the direct-drive manipulator of cloud robotics," *Cluster Comput.*, vol. 20, no. 4, pp. 3037–3049, 2017.

[58] D. F. Valencia, S. Rotilli Filho, A. D. Callegaro, M. Preindl, and A. Emadi, "Virtual-flux finite control set model predictive control of switched reluctance motor drives," in *IECON 2019-45th Annual Conference of the IEEE Industrial Electronics Society*, 2019, vol. 1, pp. 1465–1470.

[59] R. Abdel-Fadil and L. Számel, "Enhancement of the switched reluctance motor performance for electric vehicles applications using predictive current

control," in *2018 International IEEE Conference and Workshop in Óbuda on Electrical and Power Engineering (CANDO-EPE)*, 2018, pp. 195–200.

[60] J. Saeed, M. Niakinezhad, N. Fernando, and L. Wang, "Model predictive control of an electric vehicle motor drive integrated battery charger," in *2019 IEEE 13th International Conference on Compatibility, Power Electronics and Power Engineering (CPE-POWERENG)*, 2019, pp. 1–6.

[61] A. Krasovsky, S. Vasyukov, and S. Kuznetsov, "Design of Speed Regulator at Direct Torque Control of Switched Reluctance Motors," in *2019 International Conference on Industrial Engineering, Applications and Manufacturing (ICIEAM)*, 2019, pp. 1–5.

[62] R. B. Inderka and R. W. A. A. De Doncker, "DITC - Direct Instantaneous Torque Control of Switched Reluctance Drives," *IEEE Trans. Ind. Appl.*, vol. 39, no. 4, pp. 1046–1051, Jul. 2003.

[63] I. Ralev, F. Qi, B. Burkhart, A. Klein-Hessling, and R. W. De Doncker, "Impact of Smooth Torque Control on the Efficiency of a High-Speed Automotive Switched Reluctance Drive," *IEEE Trans. Ind. Appl.*, vol. 53, no. 6, pp. 5509–5517, Nov. 2017.

[64] D.-H. Lee, J. Liang, Z.-G. Lee, and J.-W. Ahn, "A simple nonlinear logical torque sharing function for low-torque ripple SR drive," *IEEE Trans. Ind.*

Electron., vol. 56, no. 8, pp. 3021–3028, 2009.

[65] X. D. Xue *et al.*, "Optimal Control Method of Motoring Operation for SRM Drives in Electric Vehicles," *IEEE Trans. Veh. Technol.*, vol. 59, no. 3, pp. 1191–1204, Mar. 2010.

[66] X. D. Xue *et al.*, "Optimal control method of motoring operation for SRM drives in electric vehicles," *IEEE Trans. Veh. Technol.*, vol. 59, no. 3, pp. 1191–1204, Mar. 2010.

[67] X. D. Xue, K. W. E. Cheng, and S. L. Ho, "Optimization and evaluation of torque-sharing functions for torque ripple minimization in switched reluctance motor drives," *IEEE Trans. Power Electron.*, vol. 24, no. 9, pp. 2076–2090, 2009.

[68] R. Mikail, I. Husain, M. S. Islam, Y. Sozer, and T. Sebastian, "Four-quadrant torque ripple minimization of switched reluctance machine through current profiling with mitigation of rotor eccentricity problem and sensor errors," *IEEE Trans. Ind. Appl.*, vol. 51, no. 3, pp. 2097–2104, 2014.

[69] J. Rodriguez and P. Cortes, *Predictive control of power converters and electrical drives*, vol. 40. John Wiley & Sons, 2012.

[70] S. Vazquez *et al.*, "Model predictive control: A review of its applications in power electronics," *IEEE Ind. Electron. Mag.*, vol. 8, no. 1, pp. 16–31, 2014.

[71] M. Preindl and S. Bolognani, "Comparison of direct and PWM model predictive control for power electronic and drive systems," in *2013 Twenty-Eighth Annual IEEE Applied Power Electronics Conference and Exposition (APEC)*, 2013, pp. 2526–2533.

[72] P. F. C. Gonçalves, S. M. A. Cruz, and A. M. S. Mendes, "Predictive current control of six-phase permanent magnet synchronous machines based on virtual vectors with optimal amplitude and phase," in *2019 International Conference on Smart Energy Systems and Technologies (SEST)*, 2019, pp. 1–6.

[73] M. Preindl, "Robust control invariant sets and Lyapunov-based MPC for IPM synchronous motor drives," *IEEE Trans. Ind. Electron.*, vol. 63, no. 6, pp. 3925–3933, 2016.

[74] M. Shirahase, S. Morimoto, and M. Sanada, "Torque ripple reduction of SRM by optimization of current reference," in *The 2010 International Power Electronics Conference-ECCE ASIA-*, 2010, pp. 2501–2507.

[75] H. Wen and Z. Pan, "A novel dead-beat torque control of switched reluctance machines," in *2011 International Conference on Electrical Machines and Systems, ICEMS 2011*, 2011.

[76] H. J. Brauer, M. D. Hennen, and R. W. De Doncker, "Multiphase torque-

sharing concepts of predictive PWM-DITC for SRM," in *2007 7th International Conference on Power Electronics and Drive Systems*, 2007, pp. 511–516.

[77] H. J. Brauer, M. D. Hennen, and R. W. De Doncker, "Control for polyphase switched reluctance machines to minimize torque ripple and decrease ohmic machine losses," *IEEE Trans. Power Electron.*, vol. 27, no. 1, pp. 370–378, 2011.

[78] D. Winterborne and V. Pickert, "Improving direct instantaneous torque control of switched reluctance machines with predictive flux constraints," 2016.

[79] W. Zhang, A. Xu, L. Han, and S. Wang, "Minimising torque ripple of SRM by applying DB-DTFC," *IET Electr. Power Appl.*, Apr. 2019.

[80] A. D. Pierre, A. R. Gilles, H. K. Théophile, and V. Antoine, "Torque ripple minimization in Switch Reluctance Motor using Model Predictive Control for water pumping application," *Curr. J. Appl. Sci. Technol.*, pp. 1–9, 2019.

[81] H. Goto and O. Ichinokura, "Model prediction based instantaneous torque control of switched reluctance motor," in *2014 International Conference on Electrical Machines (ICEM)*, 2014, pp. 810–815.

[82] H. Le-Huy and P. Brunelle, "A versatile nonlinear switched reluctance motor

model in Simulink using realistic and analytical magnetization characteristics," in *31st Annual Conference of IEEE Industrial Electronics Society, 2005. IECON 2005.*, 2005, pp. 6-pp.

[83] C. P. Weiss, A. Klein-Hessling, and R. W. De Doncker, "Discussion on control structure modifications using an FPGA for predictive DITC in switched reluctance machines regarding LUT resolution," in *19th International Conference on Electrical Machines and Systems, ICEMS 2016*, 2017.

[84] A. Sadeghzadeh and B. N. Araabi, "Auto-tune predictive control of switched reluctance motor," in *IEEE International Symposium on Industrial Electronics*, 2006, vol. 1, pp. 335–340.

[85] D. S. Weile and E. Michielssen, "Genetic algorithm optimization applied to electromagnetics: A review," *IEEE Trans. Antennas Propag.*, vol. 45, no. 3, pp. 343–353, 1997.

[86] D. S. Al-Ani, "Energy optimization strategy for system-operational problems." 2012.

[87] L. Yan, F. Wang, M. Dou, Z. Zhang, R. Kennel, and J. Rodríguez, "Active Disturbance-Rejection-Based Speed Control in Model Predictive Control for Induction Machines," *IEEE Trans. Ind. Electron.*, vol. 67, no. 4, pp. 2574–

2584, 2019.

[88] X. Yuan, S. Zhang, C. Zhang, A. Galassini, G. Buticchi, and M. Degano, "Improved Model Predictive Current Control for SPMSM Drives Using Current Update Mechanism," *IEEE Trans. Ind. Electron.*, 2020.

[89] C. A. Rojas, J. Rodriguez, F. Villarroel, J. R. Espinoza, C. A. Silva, and M. Trincado, "Predictive torque and flux control without weighting factors," *IEEE Trans. Ind. Electron.*, vol. 60, no. 2, pp. 681–690, 2012.

[90] R. E. K. Meesala, V. P. K. Kunisetti, and V. K. Thippiripati, "Enhanced predictive torque control for open end winding induction motor drive without weighting factor assignment," *IEEE Trans. Power Electron.*, vol. 34, no. 1, pp. 503–513, 2018.

[91] S. Vazquez, J. Rodriguez, M. Rivera, L. G. Franquelo, and M. Norambuena, "Model predictive control for power converters and drives: Advances and trends," *IEEE Trans. Ind. Electron.*, vol. 64, no. 2, pp. 935–947, 2016.

[92] F. Wang, H. Xie, Q. Chen, S. A. Davari, J. Rodriguez, and R. Kennel, "Parallel predictive torque control for induction machines without weighting factors," *IEEE Trans. Power Electron.*, vol. 35, no. 2, pp. 1779–1788, 2019.

[93] Y. Zhang and H. Yang, "Model-predictive flux control of induction motor drives with switching instant optimization," *IEEE Trans. Energy Convers.*,

vol. 30, no. 3, pp. 1113–1122, 2015.

[94] Y. Zhang and H. Yang, “Two-vector-based model predictive torque control without weighting factors for induction motor drives,” *IEEE Trans. Power Electron.*, vol. 31, no. 2, pp. 1381–1390, 2015.